REVIEWS OF TOPICAL PROBLEMS

1000th issue of *Uspekhi Fizicheskikh Nauk* journal

Metasurfaces: a new look at Maxwell's equations and new ways to control light

M A Remnev, V V Klimov

Contents

Abstract. The basic principles of light controling by means of metasurfaces are reviewed. Metasurfaces are able to control the phase, amplitude, polarization, and frequency of radiation propagating through them. The formulation of the generalized Snell's law is presented. Ways to realize metasurfaces using resonances and the methods of phase shift within 2π are discussed. An overview of experiments and recent achievements in the field of the light controling by means of the metasurfaces is also presented. Possible applications of metasurfaces and further development of this paradigm are considered, too.

Keywords: metasurfaces, metamaterials, nanoplasmonics, all-dielectric metasurfaces, Huygens' surfaces, metalens, meta-holograms, nonlinearity, Maxwell's equations, light beam steering, nanotechnologies, generalized Snell's law

M A Remnev N L Dukhov All-Russia Research Institute of Automatics,
ul. Sushchevskaya 22, 127055 Moscow, Russian Federation
E-mail: m.remnev@yandex.ru
V V Klimov N L Dukhov All-Russia Research Institute of Automatics,
ul. Sushchevskaya 22, 127055 Moscow, Russian Federation;
Lebedev Physical Institute, Russian Academy of Sciences,
Leninskii prosp. 53, 119991 Moscow, Russian Federation;
National Research Nuclear University MEPhI,
Kashirskoe shosse 31, 115409 Moscow, Russian Federation
E-mail: klimov256@gmail.com

1. Introduction

Throughout human history, humanity has faced the necessity of creating and using new materials, in addition to the variety of widely available ones of natural origins possessing unique properties (e.g., gold and diamonds). A number of novel materials have recently been discovered and/or synthesized, as exemplified by graphenes and their artificial analogs composed of a single layer of 1–2 carbon atoms [1–6], topological insulators, semimetals, etc. All these materials consist of natural 'brick elements' (atoms). Another approach to the development of new materials is based on the use of meta-atoms, i.e., artificial nanoscale structures with a rather simple shape [7]. Meta-atoms can be used to produce either bulk or planar structures showing properties lacking in natural materials. This review is focused on metasurfaces and planar structures comprising meta-atoms.

As applied to optics, metamaterials are considered to be rationally engineered artificial materials allowing their physical properties to be designed to meet requirements that go far beyond those of their 'natural' analogs [8]. Metasurfaces make up a class of optical metamaterials of subwave thickness capable of controling light much more efficiently than their conventional counterparts [9]. In other words, they can be regarded as two-dimensional analogs of metamaterials possessing such advantages as being very small in size, having small losses and easy to fabricate without significant losses [10].

We shall treat metasurfaces as optical devices. Light in optical equipment is controlled by altering its phase, amplitude, polarization, frequency, and spatial structure.

Conventional instruments make use of such phenomena as refringence (refractive optics), reflection, and diffraction. For example, an appropriate wave front in optical lenses and prisms is formed as light propagates through matter having a specific refractive index [11]. Light passage through a lens results in a phase shift, while continuous variation of the lens thickness promotes the emergence of a phase gradient that, in turn, alters the wave front direction in accordance with Fermat's principle [12].

Image formation using a lens has some drawbacks. A cumulation of phase shifts implies the necessity of using lenses with certain thicknesses that are much thicker than the radiation wavelength, which leads to large thicknesses of the lenses. Moreover, light of different wavelengths undergoes different phase shifts as it covers the same distance, which accounts for dispersion and related aberrations. Modern optical systems are made of a set of lenses and mirrors to compensate for the phase shift and reduce to a minimum chromatic (dispersion-induced) aberration; this complicates the optical system and makes its objectives hard to handle.

A different type of optical system employs diffraction, including the application of diffraction gratings, Fresnel zone plates, and holograms, also based on the principle of phase variation along the optical path. Such devices have advantages over refractive optical equipment in that they are much thinner than refractive lenses. However, they are not free from dispersion either, and the images are distorted as well due to different radiation wavelengths [13, 14]. Moreover, the effectiveness of diffractive optics is lower than that of usual lenses owing to the presence of higher-order diffraction maxima. On the other hand, a combination of high-order maxima allows distortions caused by dispersion to be avoided. It is, however, difficult to put together such combinations using available technologies. Usual holograms are also based on the light ray phase variation [15]. The phase profile of reflected light is controlled by etching groves of different depths on the substrate. The holograms are relatively easy to produce. Their diffraction efficiency is limited by the theoretical maximum of 40.5%, with etching inaccuracies making an additional contribution to image distortion.

One more method of light control is to use bulk metamaterials, opening enormous opportunities for the purpose [16]. Their refractive index is known to vary within a wide range [17, 18] and may even take negative values, thereby allowing making up for chromatic distortions. Moreover, metamaterials may possess nonlinear properties that further increase opportunities for their application, e.g., for frequency transformation, material transparency controling, and second-harmonic generation spectroscopy [19, 20]. However, bulk metamaterials are difficult to manufacture and show strong absorption in the visible part of the spectrum [21].

Metasurfaces, like metamaterials, open up promising opportunities for the control of light; moreover, they have a much lower absorption capacity. The very first experiments on radiation control in the infrared spectrum using a metasurface were reported a few years ago [22, 23]. The metasurfaces used in these studies were characterized by low efficiency (below 15%) and operated in the framework of a cross-polarization scheme, where output radiation passed through an additional polarizer orthogonal to the incident light. Since that time, the number of relevant publications has increased steadily and continues to grow (Fig. 1). Simulta-
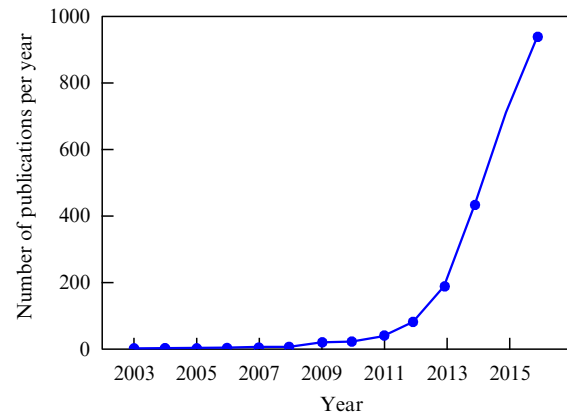

Figure 1. Number of publications per year from Scopus searches for 'metasurface' [24] as of 10 April 2017.

neously, both the quality and efficiency of metasurfaces have markedly improved. Metasurfaces operate in a visible frequency range and are utilized to fabricate submicrometer-scale lenses capable of focusing light with high accuracy and efficiency [25].

Despite the world scientific community's great interest in metasurfaces and the large number of review articles highlighting this topic [26–33], it is poorly covered in the Russian literature. The objective of the present article is to fill this gap by describing beam steering techniques using metasurfaces in infrared and visible spectra with special reference to the physical mechanisms underlying their operation. A formulation of the generalized Snell's law is offered, and basic principles of beam steering by means of metasurfaces are reviewed. An overview of experiments and recent achievements in the field of light control using metasurfaces is presented. Possible applications of metasurfaces, comprising flat lenses, holograms, etc., as well as further development of this paradigm, are considered. Special emphasis is laid on nonlinear properties of metasurfaces, opening up new prospects for beam steering.

2. Basic principles of metasurface physics: a new look at Maxwell's equations

Metasurfaces are described in terms of conventional Maxwell's equations, which brings nothing fundamentally new. However, the history of the development of metamaterials gives evidence that even conventional Maxwell's equations can describe unusual phenomena, such as the negative refractive index [34] and exceeding the diffraction limit of light [35, 36]. It is this circumstance that constitutes the basis of discussion in the present section focused on a description of individual meta-atoms and their resonances by Maxwell's equations for engineering metasurfaces capable of arbitrary phase changing over a nanometer distance.

2.1 Generalized Snell's law of refraction

The Snell law of refraction [11] relates angles of incidence θ_i and refraction θ_t of a light ray passing through the boundary between two transparent media, namely from a medium with refractive index n_1 to that having refractive index n_2:

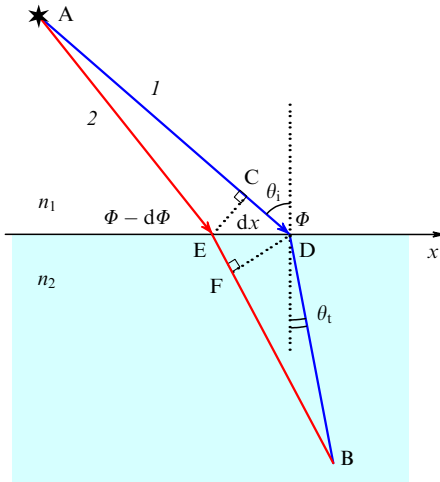$$\frac{\sin \theta_i}{\sin \theta_t} = \frac{n_2}{n_1} \, . \tag{1}$$

Figure 2. Derivation of the generalized Snell's law from the variational formulation of the Fermat principle. At the interface between two media possessing refracting indices n_1 and n_2, light ray undergoes a sharp change of phase Φ, which is a continuous function of coordinate x. Ray *1* is sent from source A to point B across the interface. In accordance with the variational principle, it takes the path at which a small change in the trajectory (path *2*) does not alter the accumulated phase.

In this case, the angle of reflection θ_r is equal to the angle of incidence. Snell's law (1) suggests phase continuity at the interface. Once there is an object capable of changing the light ray phase depending on the coordinate (e.g., a metasurface), the conventional Snell's law is not necessarily fulfilled, and the ray propagation obeys the generalized Snell's law [22].

Let us consider in detail the physical principles and formulation of the generalized Snell's law (Fig. 2). A light ray travels from source A placed in a medium with refractive index n_1 to point B located in a medium with refractive index n_2 (see Fig. 2). The ray phase undergoes a sharp change at the interface between the two media, $\Phi(x)$, where Φ is a continuous function. In accordance with the Fermat principle, the beam follows the trajectory making the shortest optical path. The passing light experiences the phase incursion

$$\Phi(x) + \int_A^B \mathbf{k}\, d\mathbf{r}\,,$$

where the first item stands for the phase jump at the interface, and the second one describes phase accumulation in the bulk. Variational formulation of the Fermat principle suggests that any small change in the trajectory does not lead to a change in the optical path in the first order of smallness [12]. If trajectory *1* is assumed to be the main one, and trajectory *2* is its variation, the latter is spaced a small distance dx apart from the former at the interface. The main ray undergoes a sudden phase shift $\Phi(x)$ at point D at the interface (Fig. 2), while ray *2* changes phase $\Phi(x - dx) = \Phi(x) - d\Phi$ at point E. Because the optical path length remains unaltered upon a small change in the ray trajectory, the phases accumulated along both trajectories must coincide, too.

Let us consider the difference between phases accumulated along ray trajectories *1* and *2*. The distance dx between them being rather small, the phases accumulated in segments AC and AE are identical in the first approximation. The same is true of segments FB and DB. Light passing along segment

CD of trajectory *1* accumulates phase $dx \sin \theta_i (k_0 n_1)$, and that along segment EF of trajectory *2* accumulates phase $dx \sin \theta_t (k_0 n_2)$. Since a phase of the rays following both trajectories should remain the same, its sharp change at points E and D leads to the relationship

$$k_0 n_1 \sin \theta_i\, dx + \Phi + d\Phi = k_0 n_2 \sin \theta_t\, dx + \Phi\,, \qquad (2)$$

where $k_0 = 2\pi/\lambda_0$; hence follows the generalized Snell's law

$$n_2 \sin \theta_t - n_1 \sin \theta_i = \frac{\lambda_0}{2\pi} \frac{d\Phi}{dx}\,. \qquad (3)$$

Expression (3) differs from the conventional Snell's law (1) in that it contains the right-hand side arising from the phase discontinuity gradient, which implies very important consequences. For example, a normally incident ray ($\theta_i = 0$) will be refracted at the angle

$$\theta_t = \arcsin\left(\frac{\lambda_0}{2\pi n_2} \frac{d\Phi}{dx}\right). \qquad (4)$$

At certain incident angles, negative refraction effect is observed, with the transmitted ray deflecting to the same side as the incident one. Moreover, two equal angles of incidence from different sides, $\pm\theta_i$, give different refracted angles, which results in two different angles of total reflection:

$$\theta_{c1,2} = \arcsin\left(\pm\frac{n_2}{n_1} - \frac{\lambda_0}{2\pi n_1} \frac{d\Phi}{dx}\right). \qquad (5)$$

Similar reasoning leads to the generalized reflection law

$$\sin \theta_r - \sin \theta_i = \frac{\lambda_0}{2\pi n_1} \frac{d\Phi}{dx}\,. \qquad (6)$$

By virtue of the phase gradient at the interface, the angle of reflection may have a critical value at which the reflected wave decays (becomes evanescent):

$$\theta_c' = \arcsin\left(1 - \frac{\lambda_0}{2\pi n_1} \frac{d\Phi}{dx}\right). \qquad (7)$$

A sudden phase change in metasurfaces is due to scattering from so-called meta-atoms. Phase modification techniques are discussed in Section 2.2.

A nanoparticle can serve, for instance, as a meta-atom [14]. It accounts for the discrete character of the dependence of phase shift Φ on coordinate x. As a rule, meta-atoms occupy periodic unit cells on metasurfaces (Fig. 3). If such cells display periodicity Δx and each meta-atom in a cell shifts the light phase by an amount greater by $\Delta\Phi$ than its predecessor does, then the phase shift gradient will be $\alpha = \Delta\Phi/\Delta x$. The phase shift by each meta-atom linearly depends on the unit cell number: $\Phi = \Phi_0 + \Delta\Phi i$, where $i = 1, 2, 3, \ldots, n$. Variable n determines the number of unit cells in a supercell, so that $n\Delta\Phi = 2\pi$. In the next supercell, the phase shift Φ begins anew.

Let us consider, by way of example, a metasurface having a supercell made up of six unit cells with meta-atoms. Such a supercell is schematically depicted in Fig. 3 between two media having refractive indices n_1 and n_2. Here, meta-atoms are nanoparticles onto which an electromagnetic wave is incident from above. Each nanoparticle within a single supercell shifts the light phase. Let us assume, for certainty, the following phase shifts: 30°, 90°, 150°, 210°, 270°, 330°. This means that the phase in the first element of any supercell
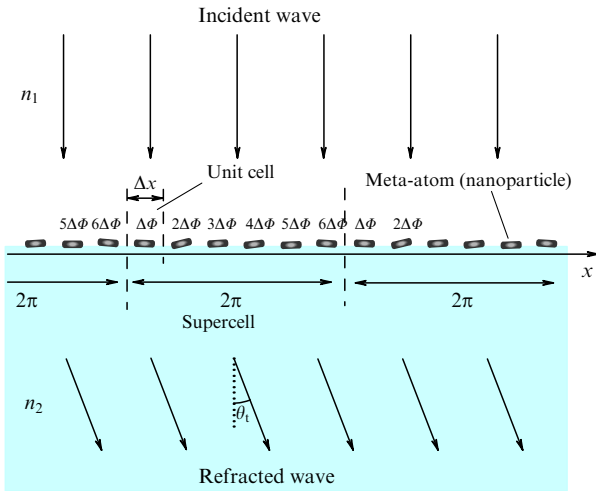
Figure 3. Light refraction by meta-atoms arranged periodically in unit cells, each shifting the phase of incident radiation by an amount that is greater by $\Delta\Phi$ than its predecessor. Supercells are formed from unit cells encompassing phase variations within 2π. The electromagnetic wave incident from the medium n_1 is directed normally to the surface. Due to the phase shift increment $\Delta\Phi/\Delta x$, the transmitted wave turns through angle θ_t.

is shifted 30°. For example, if $\Delta x = \lambda_0/4$, the right-hand side of Eqn (3) equals 2/3. When the refractive index $n_2 = 1.5$, the light incident along the normal, $\theta_i = 0$, will be refracted by an angle $\theta_t = 26.4°$.

According to geometric optics laws, a light ray is refracted at the interface between two media and follows further in a strictly determined direction. However, since the size of meta-atoms on a metasurface is smaller than or commensurate with the wavelength, wave optics needs to be employed. A metasurface resembles a diffraction grating giving several radiation intensity maxima at the output, depending on the angle. Because unit cells are smaller than the wavelength, in an ideal it is possible to achieve that only a single diffraction maximum remains.

To better understand the process of suppression of submaxima, let us represent a metasurface in the form of a phased antenna array formed by N point sources of equal power, as shown in Fig. 4. The sources are equally spaced apart, Δx, and the radiation phase difference between them is $\Delta\Phi$. Let us calculate the Poynting vector depending on angle θ between the ray direction and normal **p** to the surface over which the radiation sources are arranged. Fraunhofer interference patterns will be observed in parallel rays, i.e.,
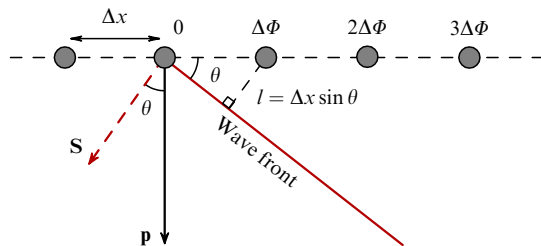

Figure 4. Phased antenna array consisting of N point sources shown as gray dots. The phase of each antenna is shifted $\Delta\Phi$ relative to the preceding one. The resulting Poynting vector **S** of total radiation is directed at angle θ to the normal **p**.

practically in the focal plane of the observer objective. The strength of the resultant field is the sum of field strengths of individual sources, while the radiation phase of each source is the sum of the phase acquired by light as it passes from the source to the observation point and the phase of each source $\delta_m = (\delta + \Delta\Phi)(m-1)$, where $\delta = (2\pi\Delta x/\lambda_0)\sin\theta$. Taking account of all sources yields the sum of a geometric progression

$$E = \sum_{m=1}^{N} \exp\left(i\delta_m\right). \tag{8}$$

The magnitude S of the Poynting vector is proportional to E^2:

$$S \sim \frac{\sin^2\left[(\delta + \Delta\Phi)N/2\right]}{\sin^2\left[(\delta + \Delta\Phi)/2\right]}. \tag{9}$$

It follows from formula (9) that the maximum on the interference pattern is observed when the denominator vanishes, i.e., $(2\pi\Delta x/\lambda_0)\sin\theta + \Delta\Phi = 2\pi n$. Therefore, the wave front angle is

$$\theta_n = \arcsin\left[\frac{\lambda_0}{\Delta x}\left(n - \frac{\Delta\Phi}{2\pi}\right)\right], \tag{10}$$

where n is the order number of the maximum. The principal maximum corresponding to $n = 0$ is always present, while additional maxima appear if the argument of arcsine is less than unity. Disregarding item $\Delta\Phi/(2\pi)$ in expression (10) yields additional maxima ($n = \pm 1$) in the interference pattern for $\Delta x \geqslant \lambda_0$. When the distance between neighboring antennas is smaller than the wavelength, a single maximum remains. Figure 5 illustrates the dependence of radiation intensity on the angle to the normal for a phased antenna array consisting of 20 sources equally spaced $\Delta x = 0.5\lambda_0$ apart from each other. The figure shows that the angle at which the principal maximum is observed increases with increasing phase difference between adjacent antennas.

Let us present the antennas depicted in Fig. 4 as sources of secondary waves generated by a plane wave incident from above at angle θ_i. Then, the sources add their phase to the phase of a re-emitted wave that varies linearly as the source number increases, i.e., $\Phi_i = \Delta\Phi i$, in analogy with meta-atom phases in Fig. 3. The phase difference $\Delta\Phi$ responsible for the phase gradient in formula (10) transforms under the influence
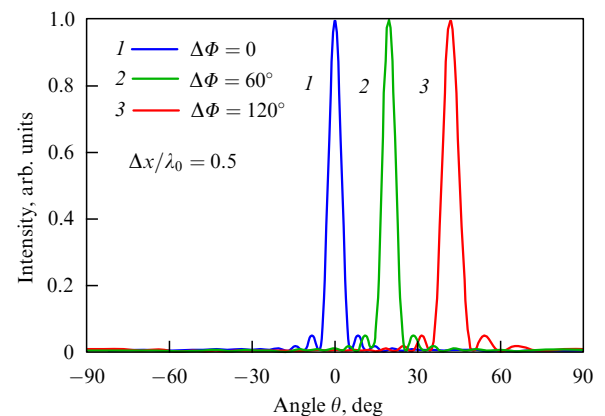

Figure 5. Angle dependence of radiation intensity of 20 equally spaced antennas for different $\Delta\Phi$ between their phases.

of the incident wave: $\Delta\Phi/(2\pi) \rightarrow \Delta\Phi/(2\pi) - \Delta x/\lambda_0 \sin\theta_i$. Taking into account different optical media (n_1 and n_2), in which the incident and transmitted waves are located, yields the generalized Snell's law for the maxima of transmitted light in the wave optics formulation:

$$\sin\theta_{t,n} n_2 - \sin\theta_i n_1 = -\frac{n\lambda_0}{\Delta x} + \frac{\lambda_0}{2\pi}\frac{\Delta\Phi}{\Delta x} . \qquad (11)$$

Here, the integer n is responsible for the maximum order. Because the interantenna distance Δx is smaller than the wavelength, one has $n = 0$, i.e., only the principal order of the transmitted light is retained.

Therefore, the presence of meta-atoms capable of sharply altering the light phase in a controllable manner at the interface between two media makes it possible to keep in check the direction of radiation across the interface. To avoid additional diffraction maxima, the distance between meta-atoms should be shorter than the radiation wavelength, and the totality of meta-atoms in a supercell of the metasurface must change the light phase from 0 to 2π. This is a very difficult task that awaited the development of new technologies and calculation methods to be addressed. The physical principles underlying phase variation by meta-atoms are considered in Section 2.2.

2.2 Phase control with the aid of resonances in meta-atoms

As was mentioned in Section 2.1, meta-atoms comprise particles of different shapes and subwave sizes. Resonances occurring in meta-atoms despite their small size [7] provide a basis for the creation of metasurfaces with an arbitrary phase shift.

2.2.1 Electric resonance in meta-atoms. Resonance may serve as one of the mechanisms for continuous adjustment of the light wave phase shift. The passage of the driving force frequency through the oscillator resonance frequency is known to change the oscillator phase by π. Let us consider a metallic nanoparticle in the form of a cylinder of length l and radius R onto which light of the wavelength λ is incident (Fig. 6). Kalousek et al. [37] report an analytical light–cylinder interaction model in the free electron approximation for $R \ll \lambda, l$ and $\lambda \sim l$.

It was shown in Ref. [7] that an alternating electric field makes electrons of the rod move in a periodic manner and gives rise to a standing wave. The boundary conditions forbid electron movements at the ends of the rod. Resonance occurs when some whole number of half wavelengths fits along the rod. Light wave frequencies at which resonance sets in are
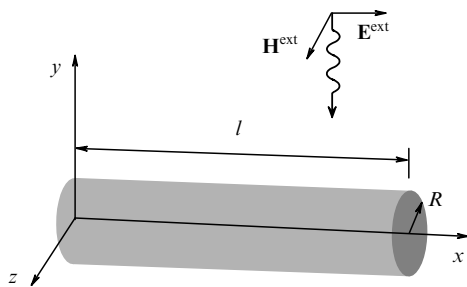

Figure 6. Schematic representation of the incidence of a flat electromagnetic wave onto a thin rod, as observed in Ref. [37]. The wavelength λ is commensurate with the rod length l.
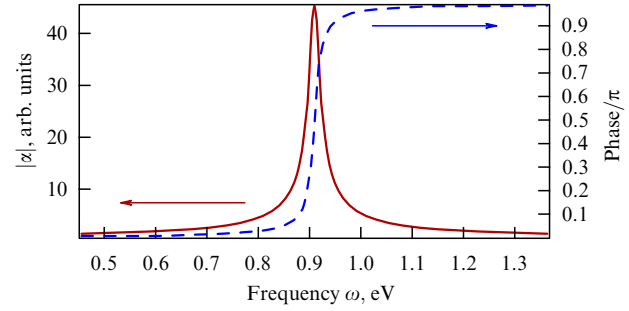

Figure 7. Amplitude and phase of the polarizability of a thin rod vs near-resonant frequency. The phase changes within the limits of π as the frequency passes through resonance.

given by the formula

$$\Omega_j = \frac{j\pi}{2}\,\omega_p\,\frac{R}{l}\,\sqrt{\ln\left(\vartheta\,\frac{l}{R}\right)}, \qquad (12)$$

where j is the oscillating mode number, ω_p is the plasma frequency, and $\vartheta = 2\exp(-1/2)$. Electron displacement inside the rod creates dipole moment $\mathbf{p}(\omega) = \alpha(\omega)\,\mathbf{E}^{ext}(\omega)$, where ω is the incident radiation frequency. In addition, the expression was derived for rod polarizability depending on driving field frequency ω:

$$\alpha_j(\omega) = \frac{8V}{j^2\pi^2}\,\frac{\omega_p^2}{\Omega_j^2 - \omega^2 - i\omega/\tau}, \qquad (13)$$

where $V = \pi R^2 l$ is the rod volume, and τ is the electron mean free time. Such resonance associated with electron oscillating modes can develop in any metallic particles.

A change in the phase of polarizability α calculated from formula (13) is illustrated in Fig. 7 for a silver rod of length $l = 400$ nm and radius $R = 13$ nm. The plasma frequency of silver is $\omega_p = 9.1$ eV and $1/\tau = 0.02$ eV [38]. The rod resonance frequency (1st harmonic) obtained from formula (12) is $\Omega = 0.91$ eV. At this frequency, the polarizability amplitude shows a very apparent peak. At frequencies lower than the resonant frequency, the polarizability phase tends to zero, i.e., rod polarizability is in phase with the external electric field. As the driving field frequency ω passes through resonance, the polarizability phase increases to π, meaning that phase shifts of rod polarizability and rod-reemitted wave can be matched by varying the incident radiation frequency. As it is, the phase shift is achieved by changing the resonant frequency rather than the external field frequency, e.g., by varying the rod length. Indeed, variation of the rod length allows obtaining the desired phase shift of the reemitted wave within π.

However, full control of radiation requires 2π phase coverage. Its extension from 0 to 2π is possible by adding a second resonance. A relatively simple method for the purpose was employed in early studies demonstrating the generalized Snell's law [22] with the use of a cross-polarization scheme or the so-called geometric resonance, involving an additional π phase shift by polarizers. For certainty, let radiation incident along the z-axis be polarized, so that the electric field $\mathbf{E}_{inc}$ is directed along the x-axis (Fig. 8). It polarizes the rod along its axis. In turn, rod polarization creates rod-scattered radiation $\mathbf{E}_{scat}$ that passes through the polarizer, so that only the y-component E_{scat}^y remains. Angle θ varies between $-\pi/2$ and

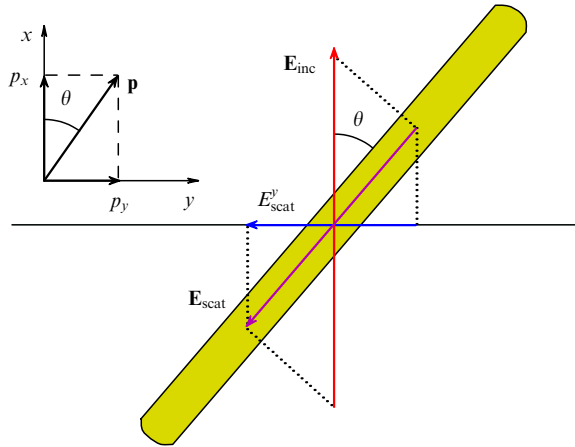**Figure 8.** π phase shift in a cross-polarization scheme. External field $\mathbf{E}_{inc}$ is polarized along the x-axis. If the rod is turned through a positive angle θ to the x-axis, as shown in the figure, the external electric field polarizes the rod in direction $\mathbf{p} = (|p_x|, |p_y|, 0)$. The scattered field $\mathbf{E}_{scat}$ is directed oppositely. Therefore, the y-component E_{scat}^y of the scattered field is directed against the axis. When $\theta < 0$, $\mathbf{E}_{inc}$ polarizes the rod in direction $\mathbf{p} = (|p_x|, -|p_y|, 0)$. Because the scattered field $\mathbf{E}_{scat}$ is directed oppositely to rod polarization $\mathbf{p}$, component E_{scat}^y is directed along the y-axis; hence, the possibility of an additional phase shift by π.

$\pi/2$. When it passes through zero, the scattered field E_{scat}^y changes sign due to the phase shift by π. Thus, a phase shift of scattered radiation is regulated within a range from 0 to π by changing the rod length l, while the additional π shift is effected by a turn through angle θ. In other words, a combination of these two parameters makes possible complete coverage of the $0–2\pi$ range.

A considerable increase in the polarization amplitude at the resonance frequency (see Fig. 7) adversely affects metasurface efficiency. Correct implementation of the generalized Snell's law (3) implies not only correct phase matching but also the similarity of amplitudes of light scattered by each meta-atom. Fortunately, the above scheme of phase matching envisages two degrees of freedom: the rod length l, and the rod

turn angle θ. The authors of Ref. [22] calculated the amplitude and the phase of the rod-scattered field, depending on the rod length l and the angle of rotation θ. The wave incident onto the rod was polarized along the y-axis, while the scattered wave passed through a polarizer oriented along the x-axis. The results are presented in Fig. 9 showing that the parameter dependence of the phase exhibits two quite apparent maxima: one between 0 and 90°, and the other in the range of θ from 90° to 180°. In all other respects, the maxima are virtually identical. The phase diagram is also split into two regions. The phase of each region changes smoothly depending on the rod length, but not the rod turn angle θ. A sharp 180° phase shift occurs only during the passage from one region to the other. The presence of two degrees of freedom permits choosing such values of parameters l and θ at which the amplitude remains constant. One such isoline is shown by the dashed curve in Fig. 9a. The placement of the isoline onto the phase diagram allows phases to be adjusted, regardless of the constancy of amplitude. Matching parameters in the isoline permits the phase of scattered radiation to be changed within a range from $-30°$ to $-140°$ that can be doubled upon transition to the second region, $\theta > 90°$, which expands phase coverage up to $\sim 325°$.

Calculations demonstrated the low efficiency of a metal rod-based metasurface. Therefore, the authors of work [22] utilized V-shaped meta-atoms in their experiments, details of which are described in Section 3 dealing with experimental realizations of metasurfaces. It is worthwhile to note that the effectiveness of metasurfaces based on electric resonance alone remains extremely low even after above-mentioned modernization. Moreover, the cross-polarization scheme does not ensure complete 2π phase coverage. A more efficient method for obtaining the desired range of phase shifts consists in superposition of electric and magnetic resonances. This is employed in the majority of ongoing studies [39–45] and is described in Section 2.2.2.

2.2.2 Magnetic resonance in meta-atoms. An efficient method for shifting the phase of scattered radiation in a range from 0 to 2π is the superposition of electric and magnetic
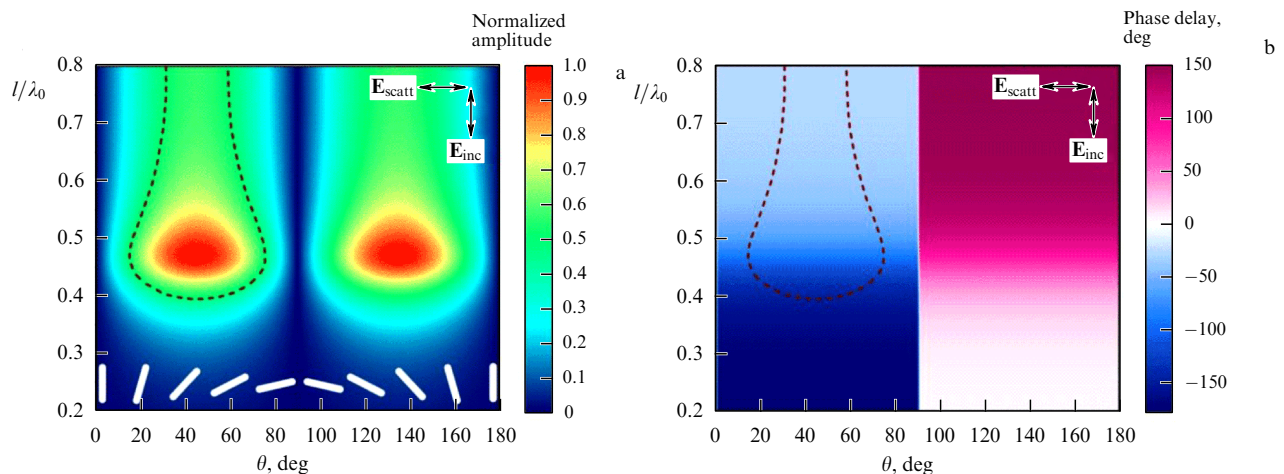

Figure 9. (Color online.) Results of calculating the amplitude (a) and phase (b) of the nanorod-scattered field depending on the rod length and the rod turn angle in Ref [22]. The polarizer of the scattered wave is normal to incident wave ($\mathbf{E}_{inc}$) polarization. A change in the rod length l causes a resonant frequency shift and a change in the scattered field phase from 0 to π. An additional π phase shift can be achieved by a change in rod turn angle θ. The scattered wave amplitude in figure (a) has quite apparent maxima. The dashed curve around one of the maxima in figure (a) shows the isoline corresponding to constant scattering amplitude. The superposition of this curve on the phase plot in figure (b) allows identifying such l and θ values at which the scattering amplitude remains constant and the phase can be chosen arbitrarily.
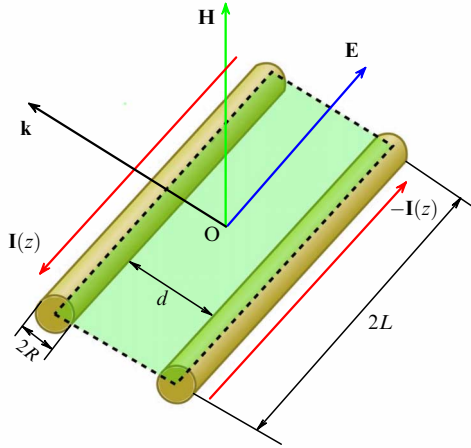
Figure 10. (Color online.) Two metallic nanorods placed in an alternating electromagnetic field, matching the model computed in Ref. [46]. It is assumed that $R \ll d \ll 2L$. Magnetic field H is directed normally to the rods' plane, and electric field E along the rods. A change in the magnetic field excites antisymmetric oscillations of current in the rods, $\mathbf{I}(z)$ and $-\mathbf{I}(z)$. Magnetic resonances occur when the whole number of electron oscillation half-waves fit inside the rod.

resonances. The latters arise from the interaction of meta-atoms with an external magnetic field. Figure 10 presents a model consisting of two thin rods placed in an alternating magnetic field $H(t) = H_0 \exp(-i\omega t)$. The electric field E is assumed to be absent for the time being. Reference [46] describes an analytical theory of magnetic plasmon resonance in this system on the assumption that $2L \gg d \gg R$. The rods form a contour in which a change in the magnetic flux results in electromagnetic induction in the rods and current oscillations $I(z)$. By virtue of problem symmetry, the current in the rods is antisymmetric with respect to the O center. Due to the absence of current I at the rod ends, resonance develops when a whole number of half-wavelengths fit inside the rod. In Ref. [46], the formula for the resonant frequency at the first oscillating mode,

$$\Omega^{M} = \frac{\pi R \omega_{p}}{4L} \sqrt{2 \ln \frac{d}{R}}, \tag{14}$$

was obtained together with the expression for frequency ω-dependent magnetic polarizability of the system:

$$\alpha_{M} = \frac{4\pi m}{H_0 V} = \frac{16 L d \omega_{p}}{\lambda^2 \Omega^{M} \sqrt{2 \ln(d/R)}} \frac{1}{1 - \omega/\Omega^{M} - i/(2\tau\Omega^{M})}, \tag{15}$$

where m is the system's magnetic moment, $V = 4LRd$, and $\lambda = 2\pi c/\omega$.

The electric and magnetic resonance frequencies are determined by the material properties and nanoparticle geometry [see formulas (12) and (14)] rather than by the wavelength-to-particle size ratio. This property of plasmonic resonance allows creating the meta-atoms much smaller than the radiation wavelength at which the metasurface operates. In both cases [see formulas (13) and (15)], the resonance peak width depends on the electron mean free time τ or extinction $1/\tau$. Similar to the case of electric resonance, the phase of the scattered radiation changes in the range from 0 to π as the frequency passes through the resonant frequency Ω^{M} of magnetic resonance.

When an electromagnetic wave is incident on a nanoparticle composed of two metallic nanorods, it is influenced by alternating electric and magnetic fields. If the wave falls in the rod plane, as shown in Fig. 10, both electric and magnetic resonances occur simultaneously in the system. As a rule, however, the resonant frequencies are significantly different, which prevents the mutual influence of the resonances. Certain authors have achieved overlapping of the electric and magnetic resonances by modifying meta-atoms [40, 45, 47–49]. Such metasurfaces steer the reflection light in the infrared and visible wavelength ranges with a rather high efficiency, as described in detail in Section 3. Here, it is more convenient to consider resonances in dielectric nanoparticles to obtain a deeper insight into the resonance overlapping mechanism and phase coverage from 0 to 2π.

Let us consider an infinite array of dielectric spherical nanoparticles following Ref. [50]. These nanoparticles lie in a plane and are affected by an incident electromagnetic wave as shown in Fig. 11. In the work referred, the nanoparticles are described as a totality of interacting electric and magnetic dipoles. In this case, the expressions for the plane wave transmission (t) and reflection (r) coefficients have the form [50]

$$t = 1 + \frac{ik_d}{4S_L^2}\left(\frac{1}{\varepsilon_0\varepsilon_d/\alpha^E - k_d^2 G_{xx}^0} + \frac{1}{1/\alpha^M - k_d^2 G_{yy}^0}\right),$$
$$r = \frac{ik_d}{4S_L^2}\left(\frac{1}{\varepsilon_0\varepsilon_d/\alpha^E - k_d^2 G_{xx}^0} - \frac{1}{1/\alpha^M - k_d^2 G_{yy}^0}\right). \tag{16}$$

Here, S_L is the unit cell area, k_d is the incident wave vector, ε_d is the dielectric constant of the array-containing medium, α^E and α^M are the electric and magnetic polarizabilities of individual particles obtained in the Mie theory, and Green's functions G_{xx}^0 and G_{yy}^0 are solutions of Maxwell's equations with point sources, which are responsible for particle interactions.

The first item of the transmission coefficient t in formula (16) is equal to unity and related to the wave transmitted without interaction with the particle array. This wave excites electric and dipole moments in the particles of the array, which lead to the appearance of the second and third items, respectively, in formula (16). The reflection coefficient r consists only of the components related to re-emitted electric and magnetic dipoles undergoing destructive interference. Figure 12 presents theoretical scattering spectra of spherical silicon nanoparticles depending on their radii R. The spectra exhibit two maxima related to the electric and magnetic resonances, the wavelengths of which are much longer than
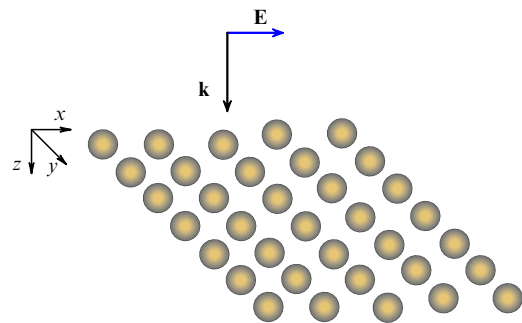

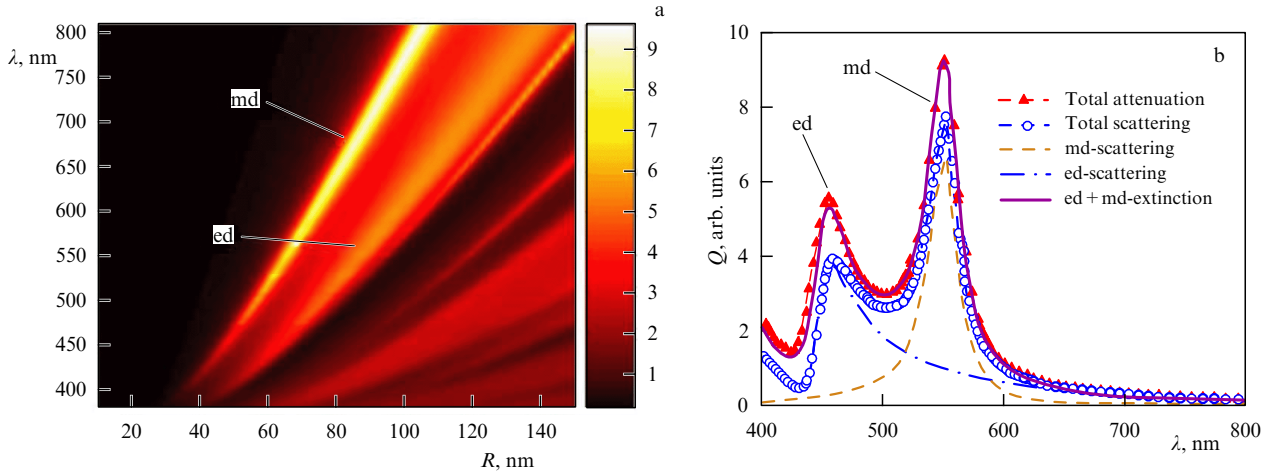**Figure 11.** Array of dielectric nanoparticles considered in Ref. [50].

Figure 12. (Color online.) (a) Scattering spectrum of Si spherical particles depending on their radius R calculated in Ref. [50]. (b) Wave extinction and scattering spectra Q of Si nanoparticles with radius $R = 65$ nm. The peaks correspond to the electric (ed) and magnetic (md) resonances.

the particle radii. An enlargement of the particle's radius leads to a rise in the resonance wavelength.

Polarizabilities $\alpha^{\rm E}$ and $\alpha^{\rm M}$, like Green's functions G_{xx}^0 and G_{yy}^0, have a complicated form. To explain the resonance overlapping mechanism, the authors of Ref. [51] approximated effective electric $\alpha_{\rm eff}^{\rm e} = 1/(\varepsilon_0 \varepsilon_{\rm d}/\alpha^{\rm E} - k_{\rm d}^2 G_{xx}^0)$ and magnetic $\alpha_{\rm eff}^{\rm m} = 1/(1/\alpha^{\rm M} - k_{\rm d}^2 G_{yy}^0)$ polarizabilities from formula (16) by the Lorentz curves:

$$\alpha_{\rm eff}^{\rm e} = \frac{\alpha_0^{\rm e}}{\omega_{\rm e}^2 - \omega^2 - 2i\gamma_{\rm e}\omega} \,,$$

$$\alpha_{\rm eff}^{\rm m} = \frac{\alpha_0^{\rm m}}{\omega_{\rm m}^2 - \omega^2 - 2i\gamma_{\rm m}\omega} \,. \qquad (17)$$

Here, the frequencies $\omega_{\rm e,m}$ correspond to electric and magnetic resonances, and $\gamma_{\rm e,m}$ to their widths. Resonance amplitudes $\alpha_0^{\rm e,m}$ are chosen such that incident radiation is totally reflected at resonant frequencies ($\omega = \omega_{\rm e}$ and $\omega = \omega_{\rm m}$) in the absence of transmission, i.e.,

$$T = |t(\omega_{\rm e,m})|^2 = \left| 1 + \frac{ik_{\rm d}}{4S_L} \alpha_{\rm eff}^{\rm e,m}(\omega_{\rm e,m}) \right|^2 = 0 \,. \qquad (18)$$

This condition yields expressions for the transmission and reflection coefficients in the ideal case when the scattering cross section coincides with the area of a unit cell in the array:

$$t = 1 + \frac{2i\gamma_{\rm e}\omega}{\omega_{\rm e}^2 - \omega^2 - 2i\gamma_{\rm e}\omega} + \frac{2i\gamma_{\rm m}\omega}{\omega_{\rm m}^2 - \omega^2 - 2i\gamma_{\rm m}\omega} \,,$$

$$r = \frac{2i\gamma_{\rm e}\omega}{\omega_{\rm e}^2 - \omega^2 - 2i\gamma_{\rm e}\omega} - \frac{2i\gamma_{\rm m}\omega}{\omega_{\rm m}^2 - \omega^2 - 2i\gamma_{\rm m}\omega} \,. \qquad (19)$$

The expressions for the amplitudes of transmitted and reflected waves in the ideal case (19) allow us to understand how resonance overlapping occurs. Figure 13 plots dependences of the phase and amplitude of the wave transmitted through an infinite array of nanoparticles and calculated from formula (19). Resonance widths $\gamma_{\rm e}$ and $\gamma_{\rm m}$ were assumed to be equal. In Fig. 13a, $\omega_{\rm e} \neq \omega_{\rm m}$. As frequency ω passes separately through either resonance, its amplitude decreases and vanishes at the resonant frequency. The wave incident on an array of nanoparticles is totally reflected at resonant frequencies. Moreover, the phase varies in a range from $-\pi/2$ to $\pi/2$ (or from 0 to π) as the frequency passes through each resonance, similarly to the phase of an individual resonance (see Fig. 7).

The situation changes dramatically when resonance frequencies coincide: $\omega_{\rm e} = \omega_{\rm m}$. Figure 13b shows the depend-
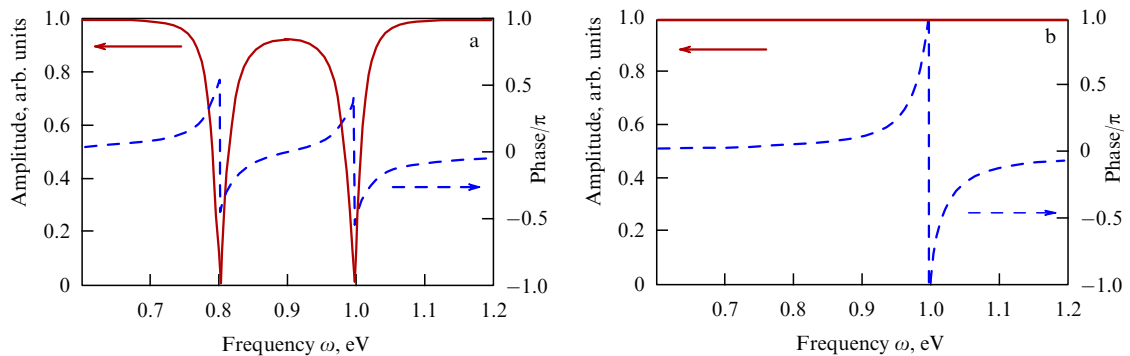

Figure 13. (Color online.) Amplitude and phase of a wave transmitted through an infinite array of nanoparticles in an ideal case when the scattering cross section coincides with the unit cell area [see formula (19)]. (a) The electric and magnetic resonances do not coincide ($\omega_{\rm m} = 0.8$ eV and $\omega_{\rm e} = 1.0$ eV). As the frequency passes through each resonance, the amplitude of the transmitted wave vanishes, and the phase varies within π. (b) The frequencies of both resonances coincide: $\omega_{\rm m} = \omega_{\rm e} = 1.0$ eV. As the frequency passes through each resonance, the amplitude remains unaltered, while the phase varies within 2π. Parameters $\gamma_{\rm m} = \gamma_{\rm e} = 0.02$ eV were used in calculations.
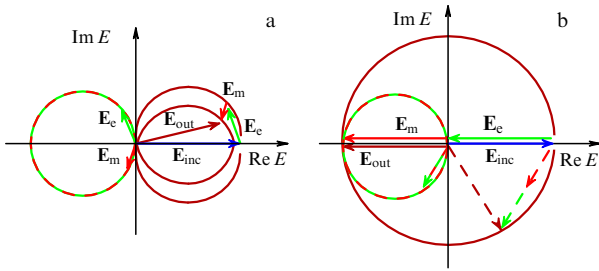
Figure 14. (Color online.) Vector field diagrams describing decomposition of the electric field vector $\mathbf{E}_{out}$ of the transmitted wave. Re E and Im E are the real and imaginary components of the electric field, respectively. The transmitted field comprises the incident field and the field scattered by electric and magnetic dipoles: $\mathbf{E}_{out} = \mathbf{E}_{inc} + \mathbf{E}_e + \mathbf{E}_m$. (a) Magnetic and electric resonances do not coincide (see Fig. 13a). (b) Magnetic and electric resonances coincide (see Fig. 13b).

ence of the amplitude and phase of a transmitted wave on frequency in the case of coincident electric and magnetic resonances. Here, the amplitude of the transmitted wave remains unaltered during passage through resonance, while the phase varies in the range from $-\pi$ to π. The amplitude of the reflected wave at $\omega_e = \omega_m$ is identically equal to zero.

It should be noted that the condition of coincidence of electric and magnetic resonances is analogous to the Kerker condition [52–54]: the reflection disappears when $\varepsilon = \mu$. However, magnetic permeability μ of a medium is usually a function of electron spin and orbital magnetic moments, whereas magnetic and electric polarizabilities in meta-atoms are normally unrelated to spins.

To elucidate the physical aspects of resonance overlap leading to 2π phase coverage, a vector field diagram can be employed, as shown in Fig. 14 [51]. The total output field is composed of the incident wave field and the field scattered by electric and magnetic dipoles: $\mathbf{E}_{out} = \mathbf{E}_{inc} + \mathbf{E}_e + \mathbf{E}_m$. The incident field shown by the blue arrow remains unaltered as the frequency changes. The vectors of scattered electric and magnetic fields shown by green and red arrows, respectively, circumscribe a circle lying in the left-handed half-plane as the incident light frequency passes through resonance. When the frequencies of the electric and magnetic resonances fail to coincide (Fig. 13a), these vectors run around the perimeter of the circle alternately. Their amplitudes being smaller than those of the incident field, the total field $\mathbf{E}_{out}$ circumscribes the figure colored deep-red and lying almost entirely in the right-handed half-plane of Fig. 14a. The phase of the output field $\mathbf{E}_{out}$ changes from $-\pi/2$ to $\pi/2$ and thereby ensures π phase coverage. When resonance frequencies coincide (Fig. 13b), vectors $\mathbf{E}_e$ and $\mathbf{E}_m$ simultaneously circumscribe a circle in the left-handed half-plane. As a result, their total amplitude is doubled when the frequency passes through resonance, and the total vector $\mathbf{E}_{out}$ circumscribes a circle that occupies all the four quadrants, as shown by the deep-red line in Fig. 14b. For example, when the incident field frequency coincides with the resonance frequency ($\omega = 1$ eV in Fig. 13b), both vectors $\mathbf{E}_e$ and $\mathbf{E}_m$ of scattered fields are directed opposite to $\mathbf{E}_{inc}$ and have the same length. Then, the $\mathbf{E}_{out}$ phase spans π, as indicated by the deep-red arrow in Fig. 14. At a frequency somewhat higher than the resonance frequency $\omega = 1.03$ eV, both vectors $\mathbf{E}_e$ and $\mathbf{E}_m$ lie in the left lower quarter of the plane (green and red dashed lines). The total vector has a unity amplitude and is turned through the angle $\approx -\pi/3$. This accounts for a change in the phase of the incident field $\mathbf{E}_{out}$ within 2π.

As a matter of fact, the resonances are far from ideal, unlike those described by formula (19). Both their widths and their frequencies coincide only in part, while the scattered field amplitude is smaller than that of the incident wave. Nevertheless, this model explains the physics of phase variation in meta-atoms in the range from 0 to 2π.

Similarly to the single-resonance case, the phase is selected in practice by varying resonant frequencies at a fixed incident wave frequency. As a rule, geometric parameters of nanoparticles are varied (see, for instance, Refs [47, 51, 55]). Moreover, the adjustment of geometric parameters is needed for coincidence of resonances. For example, it was shown in Ref. [53] that regulation of the ratio between the axes of a spheroidal dielectric nanoparticle allows the Kerker condition to be fulfilled. However, varying the parameters and resonance frequencies entails changing not only the phase but also the amplitude of the transmitted wave, which negatively affects the performance of metasurfaces. Phase matching, while simultaneously retaining constant amplitude, is possible due to the presence of several degrees of freedom, as in the case with a single resonance (see Fig. 9).

2.2.3 Use of the Pancharatnam–Berry phase. The above phase control methods making use of resonances in meta-atoms are applicable only within a relatively narrow wavelength range. A fundamentally different method of the radiation phase control by means of meta-atoms is based on Pancharatnam–Berry phase variation [56–59]. Its advantage consists in independence of the phase shift of the radiation wavelength. However, it is applicable to circularly polarized light alone.

Let us consider the main characteristics of such metasurfaces based on the data from Ref. [57] demonstrating the possibility of arbitrarily changing the phase within 2π in the framework of a simple model permitting us to understand the principle of phase control. Meta-atoms of a metasurface comprise nanorods turned through an angle to the axis, as shown in Fig. 15a. A circularly polarized electromagnetic wave is incident on the metasurface. Scattering by a meta-atom gives rise to a scattered oppositely polarized wave. The
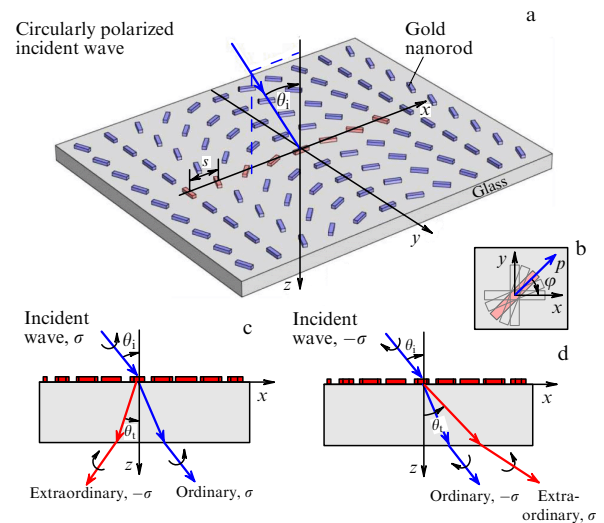

Figure 15. (Color online.) Control of circularly polarized light [57]. (a) General view of a metasurface from gold nanorods placed on a glass substrate; (b) an individual rod turned through angle φ to control the phase within 2π; (c, d) layout of experiments. Left and right circularly polarized light is deflected to different directions.

angle of rod rotation determines the phase of the scattered wave, $\Delta\Phi = 2\varphi$, and a nanorod turn within π angle allows following up the phase shift in the range from 0 to 2π.

Let us consider the following model [57] to better understand the mechanism of phase control by the rotation of a nanorod. Let a single nanorod lie in plane xy and be turned through angle φ with respect to the x-axis, as shown in Fig. 15b. A circularly polarized electromagnetic wave propagating in the xz plane is incident on the rod at angle θ_i. Then, the electric field strength of this wave has the form

$$\mathbf{E}^\sigma = E_x\mathbf{e}_x + E_y\mathbf{e}_y + E_z\mathbf{e}_z$$
$$= \frac{1}{\sqrt{2}}\left(\cos\theta_i\,\mathbf{e}_x + \sigma i\,\mathbf{e}_y - \sin\theta_i\,\mathbf{e}_z\right), \qquad (20)$$

where $\sigma = \pm 1$ denotes right- and left-hand polarization, respectively, E_x, E_y, E_z are components of electric field strength, and $\mathbf{e}_x$, $\mathbf{e}_y$, $\mathbf{e}_z$ are unit vectors along the x-, y-, and z-axes, respectively. The nanorod in this model constitutes a dipole antenna. Its electric dipole moment $\mathbf{p}$ can be expressed through the rod polarizability α_e and turn angle φ:

$$\begin{pmatrix} p_x \\ p_y \end{pmatrix} = \alpha_e \begin{pmatrix} \cos^2\varphi & \sin\varphi\cos\varphi \\ \sin\varphi\cos\varphi & \sin^2\varphi \end{pmatrix} \begin{pmatrix} E_x \\ E_y \end{pmatrix}. \qquad (21)$$

The far field of the electric dipole is written out as

$$\mathbf{H}_{\mathrm{rad}} = \frac{ck^2}{4\pi}\left(\mathbf{u}\times\mathbf{p}\right)\frac{\exp(ikr)}{r}\,;$$
$$\mathbf{E}_{\mathrm{rad}} = \sqrt{\frac{\mu_0}{\varepsilon_0 n_1^2}}\left(\mathbf{H}_{\mathrm{rad}}\times\mathbf{u}\right), \qquad (22)$$

where r is the distance from the dipole, $\mathbf{u}$ is the unit vector of the field observation direction, and $k = 2\pi n_t/\lambda_0$ is the wave vector amplitude. Let us consider the direction of re-emitted wave propagation in the xz plane. Then, the unit vector can be expressed through the observation angle θ_t: $\mathbf{u} = \sin\theta_t\,\mathbf{e}_x + \cos\theta_t\,\mathbf{e}_z$. Substituting formulas (20) and (21) into expression (22) yields a formula for the strength of the field scattered by meta-atoms [57]:

$$\mathbf{E}_{\mathrm{rad}} \approx \frac{c\alpha_e k^2 \exp(ikr)}{4\sqrt{2}\pi r}\left[\frac{\cos\theta_i\cos\theta_t + 1}{4}\,\mathbf{E}_\mathbf{u}^\sigma\right.$$
$$\left. + \frac{(\cos\theta_i + 1)(\cos\theta_t + 1)}{8}\,\mathbf{E}_\mathbf{u}^{-\sigma}\exp(2i\sigma\varphi)\right], \qquad (23)$$

where $\mathbf{E}_\mathbf{u}^{\pm\sigma} = \cos\theta_t\,\mathbf{e}_x \pm \sigma i\mathbf{e}_y - \sin\theta_t\,\mathbf{e}_z$.

The first item in formula (23) corresponds to a wave with the same circular polarization as that of a wave incident upon a nanoparticle. The second item defines a wave with opposite circular polarization. It includes factor $\exp(2i\sigma\varphi)$ depending on polarization σ and rod turn angle φ. It is this factor that describes the phase shift unrelated to the radiation wavelength but depending on the nanorod turn angle.

Light polarization σ influences the sign of the metasurface phase gradient. Therefore, in accordance with formula (3), a wave with different polarization will deflect toward different sides with respect to the direction of usual refraction. Figures 15c, d show that nanosurface-incident radiation is divided into a wave with the same polarization transmitted in agreement with the conventional Snell's law and an oppositely polarized wave obeying the generalized Snell's law. The left-hand circularly polarized wave incident on the metasurface in Fig. 15c is colored blue. The extraordinarily transmitted right-hand circularly polarized wave shown in red

color deflects to the left from the ordinarily transmitted wave with left-hand polarization. In contrast, Fig. 15d plots a right-hand circularly polarized wave (painted red) incident on the metasurface. The anomalously transmitted wave is left-hand polarized and deflects to the right of the ordinarily transmitted one.

The phase shift by turning the nanorod can be interpreted in terms of the Pancharatnam–Berry phase [60, 61]; therefore, metasurfaces of this type are frequently referred to as Pancharatnam–Berry metasurfaces.

Meta-atoms altering the Pancharatnam–Berry phase may consists not only of nanorods. For example, Ref. [59] describes Π-shaped meta-atoms. The rotation angle of such nanoparticles also determines the phase shift. The Pancharatnam–Berry phase can be controlled by making use of elliptic holes in a thin metal film [58].

2.3 Other principles behind metasurface operation. Nonlinear effects

The principles of phase control for light propagating through a metasurface were described in Sections 2.1 and 2.2 in terms of the optical properties of meta-atoms, with special reference to the far field. However, the near field of meta-atoms opens up equally promising prospects for control of light owing to the fact that the near field of nanoparticles (especially metallic ones) multiply increases in the resonance region in comparison with incident fields. This field enhancement of nanoparticles gives rise to strong nonlinear effects, such as the generation of second and third harmonics. Due to this, metasurfaces possess nonlinear optical properties [19, 20, 33, 62]. Parameters of the nonlinear response of a metasurface, e.g., intensity, phase, and polarization, can be controlled by changing the geometry of meta-atoms. Moreover, inasmuch as the size of meta-atoms is much smaller than the wavelength, the electromagnetic field can be focused onto a region of an equally small size. Such properties can be used to create controllable optical devices, modify radiation wavelength, and develop ultrahigh-sensitive sensors and optical microscope systems capable of overcoming the diffraction limit.

Nonlinear optics has a history of several decades. Second-harmonic generation on a quartz crystal irradiated by a pulsed ruby-laser beam (694.3 nm) was observed for the first time in 1961 [63]. The spectrum of radiation transmitted through the crystal had a weak maximum at a half-wavelength of 347.2 nm, besides the main peak. Since then, many theoretical and experimental studies on nonlinear optical effects have been published. Such effects find wide application in a variety of optical devices, from waveguides to photonic crystals.

Nonlinear properties of matter account for the appearance of the highest degrees in the dependence of polarization $\mathbf{P}^{\mathrm{NL}}$ on electromagnetic field strength [33, 64]:

$$P_i^{\mathrm{NL}} = \chi_{ijk}^{(2)}E_j^\omega E_k^\omega + \chi_{ijkl}^{(3)}E_j^\omega E_k^\omega E_l^\omega + \dots, \qquad (24)$$

where $\mathbf{E}^\omega$ is the electric field strength of the fundamental harmonic, and $\chi^{(2)}$ and $\chi^{(3)}$ are the second- and third-order nonlinear susceptibilities, respectively. The second-order susceptibility vanishes in the case of central symmetry. Second-harmonic generation proves highly sensitive to symmetry breaking, e.g., the presence of surfaces and interfaces. Moreover, quadrupole and magnetic dipole moments greatly contribute to second-harmonic generation [64–66].

Most studies on the nonlinear properties of metasurfaces deal with the generation of second-harmonic radiation (see, for instance, Refs [62, 67–70]). In these studies, second-harmonic generation is carried out utilizing plasmonic metasurfaces with meta-atoms represented by either metallic nanoparticles or holes in metal films. The contribution to the nanoparticle's second harmonic comes from both surface ($\mathbf{P}^{\mathrm{surf}}$) and bulk ($\mathbf{P}^{\mathrm{bulk}}$) polarizations [71, 72]. In the former case, for isotropic and centrosymmetric materials, the second-order susceptibility tensor $\chi^{(2)}$ from Eqn (24) can be reduced to three independent components: $\chi_{\perp\perp\perp}$, $\chi_{\perp\|\|}$, and $\chi_{\|\|\perp}$, where symbols $\perp$ and $\|$ denote perpendicular and parallel directions with respect to the surface, respectively. Moreover, component $\chi_{\perp\|\|}$ makes, from the theoretical and experimental standpoints, only a minor contribution to second-harmonic generation in noble metals, which is important for plasmonic metasurfaces [72]. Therefore, the main contribution comes from two kinds of polarization:

$$P_{\perp}^{\mathrm{surf}}(\mathbf{r}, 2\omega) = \chi_{\perp\perp\perp} E_{\perp}(\mathbf{r}, \omega)\, E_{\perp}(\mathbf{r}, \omega)\,,$$
$$P_{\|}^{\mathrm{surf}}(\mathbf{r}, 2\omega) = \chi_{\|\|\perp} E_{\|}(\mathbf{r}, \omega)\, E_{\perp}(\mathbf{r}, \omega)\,, \tag{25}$$

where the electric field inside the metal is taken into account. Polarization of the surface generates currents flowing already over the outer metal surface and calculated from the formula $\mathbf{j}^{\mathrm{surf}} = \partial \mathbf{P}^{\mathrm{surf}}/\partial t$.

It follows from general considerations that different components may contribute to bulk polarization $\mathbf{P}^{\mathrm{bulk}}$. For noble metal particles, bulk polarization can be expressed as [72]

$$\mathbf{P}^{\mathrm{bulk}}(\mathbf{r}, 2\omega) = \gamma \nabla \big(\mathbf{E}(\mathbf{r}, \omega)\, \mathbf{E}(\mathbf{r}, \omega) \big)\,, \tag{26}$$

where γ is the bulk susceptibility. Associated with bulk polarization are bulk currents $\mathbf{j}^{\mathrm{bulk}} = \partial \mathbf{P}^{\mathrm{bulk}}/\partial t$ as well. Given that components $\chi_{\perp\perp\perp}$, $\chi_{\|\|\perp}$, and γ of the surface susceptibility tensor, as well as bulk susceptibility, are known, it is possible to comprehensively describe the generation of second-harmonic radiation by a meta-atom. Characteristic susceptibility values are small enough, e.g., for gold $|\chi_{\perp\perp\perp}| = 4.4 \times 10^{-13}$ cm^2 stat V^{-1}, $|\chi_{\|\|\perp}| = 1.3 \times 10^{-14}$ cm^2 stat V^{-1}, and $\gamma = 2.1 \times 10^{-15}$ cm^2 stat V^{-1} [73].[1]

The values of the susceptibility tensor suggest that $\chi_{\perp\perp\perp}$ is of primary importance, and it alone can be used to describe the nonlinear properties of metasurfaces in the first approximation. However, it should be kept in mind that the total dipole moment for highly symmetric meta-atoms can be zero, since it follows from Eqn (25) that the opposite side of a symmetric particle may have charges with the identical sign. For this reason, asymmetric meta-atoms undergoing resonances both at the incident wave frequency and at the second-harmonic frequency are employed in designing nonlinear metasurfaces. Examples of such metasurfaces are presented in Section 3.3.

The efficiency of second-harmonic generation can be calculated as the ratio of the scattered wave power at a doubled frequency to the incident radiation (fundamental harmonic) power: $\eta = P_{\mathrm{SHG}}/P_{\mathrm{FW}}$. It follows from formula (25) that P_{SHG} increases as the square of P_{FW}. Due to this, η

increases too with the incident radiation power. However, the unlimited power augmentation results in metasurface destruction [74, 75] at $P_{\mathrm{FW}}^{\mathrm{max}} \sim 1$ GW cm^{-2} (in an impulse). Therefore, a maximum attainable efficiency η_{max} is usually reported in most publications, i.e., the efficiency at which second-harmonic generation still occurs without metasurface decomposition.

To avoid the dependence of second-harmonic generation efficiency on the incident radiation power, an effective nonlinear coefficient $\gamma_{\mathrm{eff}} = P_{\mathrm{SHG}}/P_{\mathrm{FW}}^2 = \eta/P_{\mathrm{FW}}$ is introduced [75]. Experiments in Ref. [75] showed that this quantity is virtually unrelated to the pumping power and can be used to compare metasurfaces without augmenting the fundamental harmonic power to a critical level.

3. Experimental realizations of beam steering by means of metasurfaces

The principles underlying the physics of metasurfaces and radiation control with their application were presented in Section 2. These principles are based on Maxwell's equations and could actually have been used 100 years ago. However, only the advent of nanotechnologies made it possible to create and arrange in order nanoparticles of arbitrary shapes and sizes on a substrate to compose metasurfaces.

As a rule, metasurfaces are formed by planar technologies [25, 48, 55] based on complementary metal–oxide–semiconductor (CMOS) structures [76] that are much easier to produce than bulk metamaterials. Efficiency is one of the most important characteristics involved to compare metasurfaces among themselves and to other optical devices. An electromagnetic wave incident on a metasurface is partly absorbed and scattered in different directions, but only one of them is deemed correct. The ratio of intensity of an electromagnetic wave propagating in the correct direction after it passes through the metasurface to incident wave intensity is called metasurface efficiency. For example, in Ref. [22], designed to verify the generalized Snell's law, the correct direction corresponded to the angle described by formula (3), which means that metasurface efficiency was calculated in paper [22] as the ratio of intensity of an electromagnetic wave transmitted according to the generalized Snell's law to that of the incident wave. Another important feature of a metasurface is the working wavelength. It has gone down with technical progress and has recently approached the wavelength of visible light (see Ref. [77]). Resonances being narrow enough, metasurfaces operate within a short frequency range. Its width is one more important characteristic of metasurfaces, and researchers are doing their best to further broaden it [78].

3.1 Experimental verification of generalized Snell's law and beam steering using resonances in meta-atoms
Demonstration of realizability of the generalized Snell's law on a metasurface in the infrared range was reported a few years ago [22]. The metasurface worked in radiation transmission. Meta-atoms were gold nanoparticles in the form of paired rods connected at certain angles, i.e., V-shaped rods (Fig. 16a). The cross-polarization scheme shown in Fig. 8 was employed. Polarized light was incident on the metasurface. Transmitted and reflected radiation consisted of two components each: ordinary (polarized in the same plane as the incident one) and anomalous (polarized in the perpendicular plane) (Fig. 16b). The choice of V-shaped nanoparticles was

---

[1] A statvolt per centimeter (stat V cm^{-1}) is the CGS unit of an electric field strength. Application of a voltage of 1 stat V cm$^{-1} = 299.79$ V between two infinite parallel planes spaced 1 cm apart generates an electric field of 1 stat V cm$^{-1} = 29979.2$ V m$^{-1} = 1$ G.
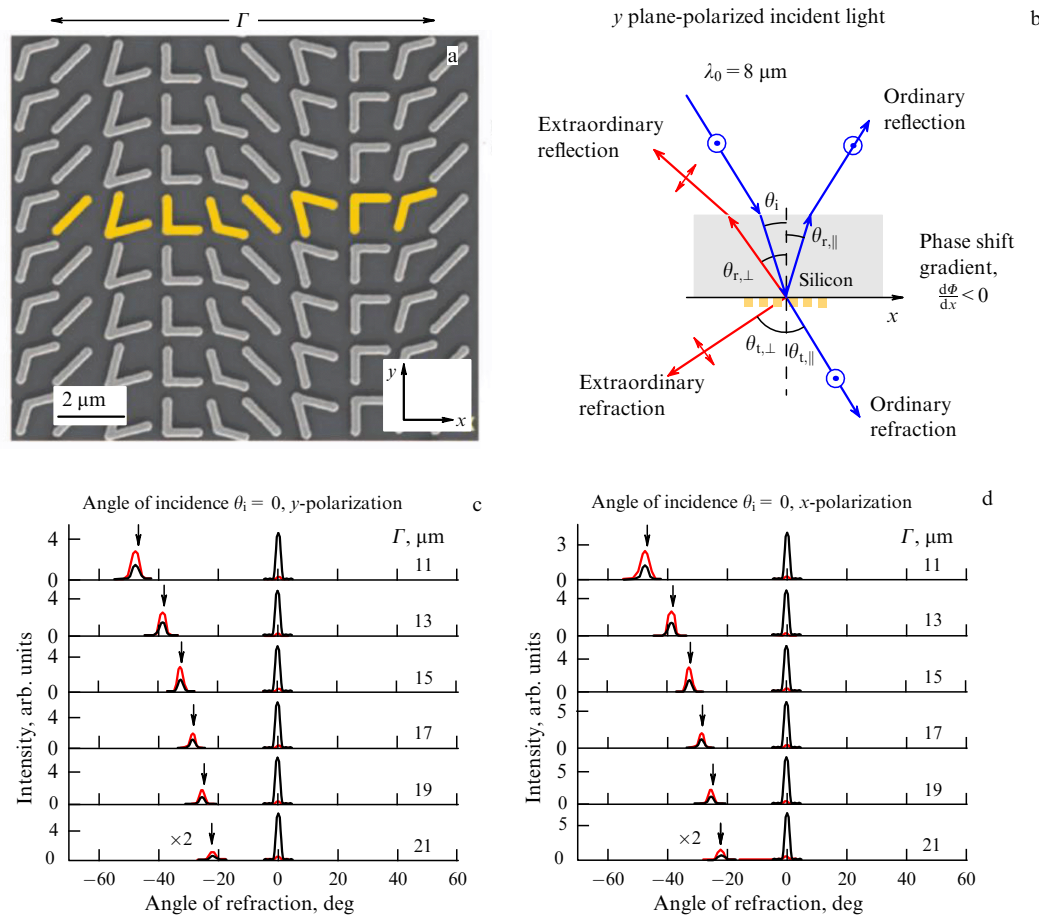
Figure 16. (Color online.) Schematic realization of the generalized Snell's law [22]. (a) Electron microscope image of a metasurface. Yellow color in the center shows a supercell composed of eight meta-atoms. (b) Layout of experiment: y-polarized light is incident on the metasurface; the light passes through the metasurface, it is divided into ordinary and extraordinary transmitted and reflected radiation. (c, d). Dependences of transmitted radiation intensity on the measurement angle for the y- and x-polarized ordinary incident wave, respectively. The red and black lines denote the intensity in the presence and absence of an output polarizer, respectively.

dictated by the fact that their efficiency was much higher than in usual nanorods. Moreover, such nanoparticles possessed two resonance modes, symmetric and antisymmetric, which allowed the incident wave to be polarized in the x- and y-directions. Two degrees of freedom in the nanoparticles, the rod length and the angle between rods, permitted adjusting phase shifts and retaining the scattering amplitude unaltered.

The size of an unit cell in the above experiment was 1.5 μm, the rod length varied from 0.8 to 1.6 μm, the rod width was ≈ 220 μm, and the thickness was ≈ 50 nm. Measurements were made in the infrared wavelength range from 8 to 21 μm.

The dependences of the intensity of radiation after its passage through the metasurface on the measuring angle are plotted in Fig. 16c, d. The electromagnetic wave falls at a right angle to the metasurface. The intensity in the absence of a polarizer shown by the black line exhibits two peaks corresponding to ordinary and extraordinary transmission, respectively. The red line denotes the intensity of radiation transmitted through a polarizer, i.e., it corresponds only to extraordinary radiation. Evidently, for different sizes Γ of the supercell, radiation undergoes refraction at different angles: the smaller the wavelength, the larger the deflection angle. It follows from Fig. 16c, d that metasurface efficiency does not exceed 40%.

Reference [22] also confirmed the generalized Snell's law (3) and (6) by direct measurement of radiation intensity. Figure 17a displays intensity maxima of ordinary (black) and extraordinary (red) radiation transmitted through the metasurface. Measurements were made at the wavelength $\lambda_0 = 8$ μm. The extraordinary radiation corresponds to the generalized Snell's law. Importantly, the figure shows the negative transmission region in which the light bends toward the same side whence the incident wave comes. The dependence of the position of reflected light maxima is presented in Fig. 17b. The reflected radiation also has ordinary and extraordinary peaks depicted in black and red, respectively. The figure shows the negative reflection region. In both graphs, experimental and theoretical data are in excellent agreement.

The authors of Ref. [22] not only verified the generalized Snell's law but also demonstrated the ability of metasurfaces to arbitrarily prepare radiation, e.g., to create optical vortices (Fig. 18c). To this effect, they divided a metasurface into eight sectors, each of them shifting the phase of transmitted radiation by its own amount. Meta-atoms were V-shaped nanoparticles, as demonstrated in Fig. 18a, b. An electromagnetic wave passed through the metasurface and interfered with a Gaussian beam, thus giving rise to a vortex (presented in Fig. 18c). This image roughly agrees with the theoretical one (Fig. 18d).
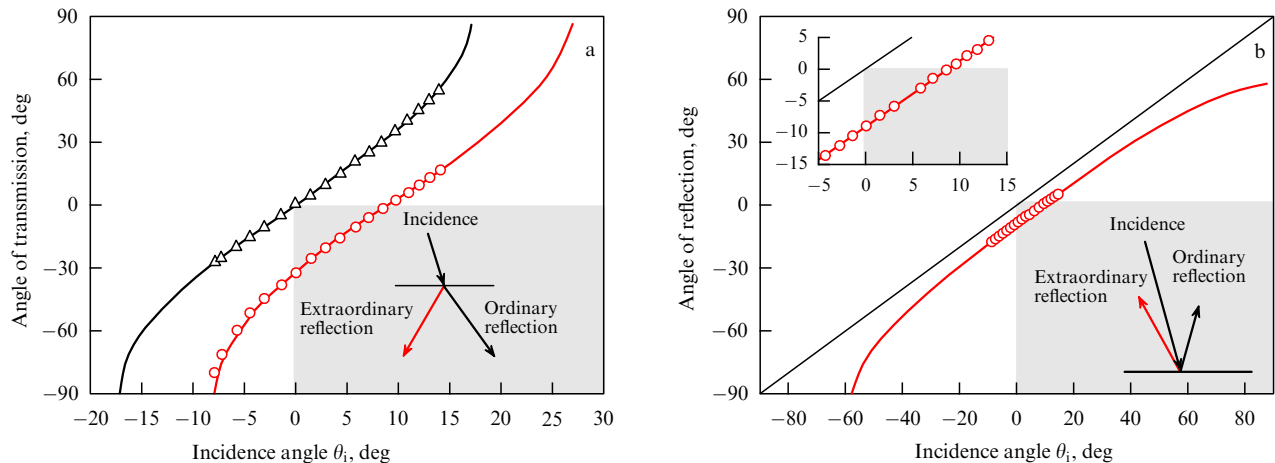
Figure 17. (Color online.) Experimental verification of the generalized Snell's law [22]. (a) The dependence of the angle of transmitted radiation peak on the incident light angle. (b) The dependence of the angle of reflected radiation on the incident light angle. Symbols and curves denote experimental and theoretical data, respectively. Black lines and symbols correspond to ordinary transmission and reflection laws, while red ones to the generalized Snell's law.
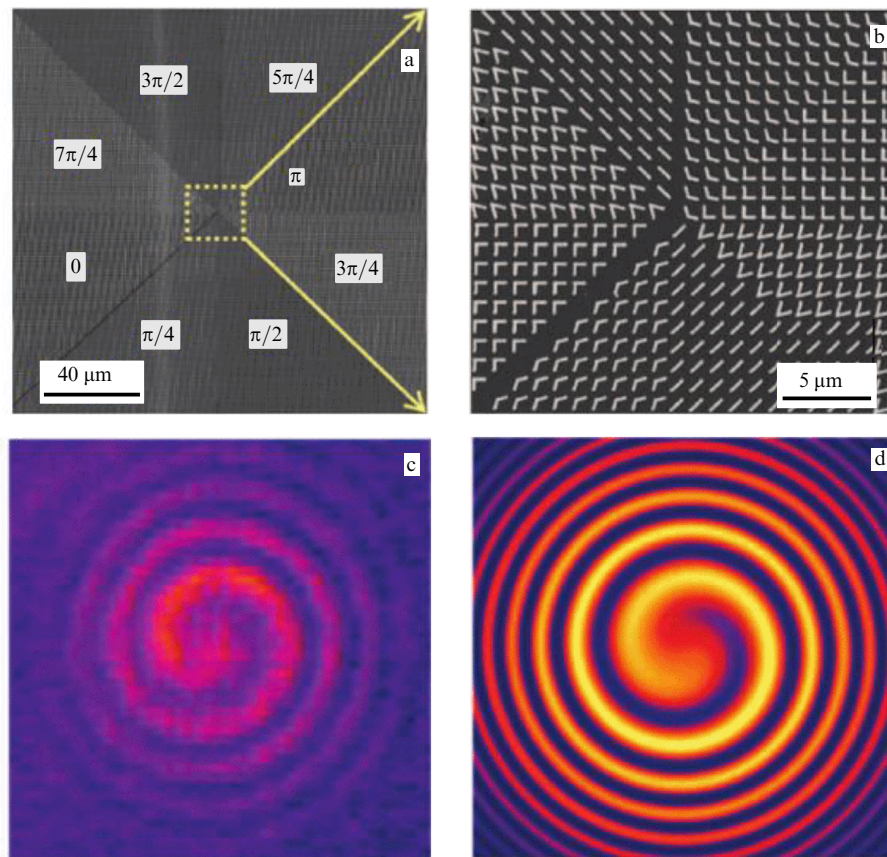

Figure 18. (Color online.) Formation of an optical vortex as a result of interference between radiation transmitted through a metasurface and a Gaussian beam in Ref. [22]. (a) Electron microscope image of a metasurface. The metasurface is divided into eight sectors, each shifting the phase of transmitted radiation by a certain amount. Each following sector shifts the phase by more than $\pi/4$ relative to the preceding one. (b) Magnified image of the central part of the metasurface. Meta-atoms are V-shaped nanoparticles. (c) Image of experimental vortex. (d) Image of simulated vortex.

A similar later experiment based on the cross-polarization scheme [23] was also carried out using gold nanoparticles as meta-atoms. The rod length varied from 93 to 158 nm, the width was 40 nm, and the thickness was 30 nm. The radiation wavelength ranged from 1 to 1.9 μm. Figure 19 presents results of an experiment in which excellent agreement between the observed data and theoretical formula (3) was achieved, while metasurface efficiency was much lower due to ohmic losses in gold, amounting to $\approx 1\%$

A marked improvement in the efficiency was reached by combining electric and magnetic resonances (see Figs 10, 13, and 14) [45, 47–49]. These studies were designed to investigate
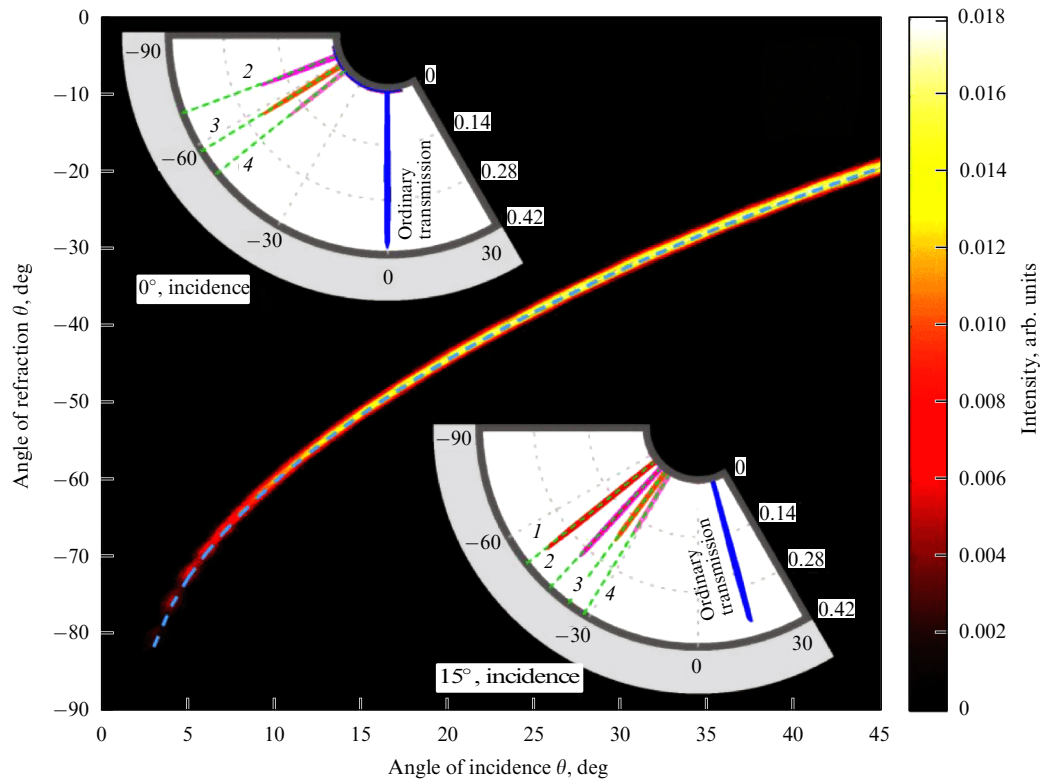
Figure 19. (Color online.) Demonstration of the generalized Snell's law in a cross-polarization scheme described in Ref. [23]. Color gradation marks the variation of radiation intensity. Wavelength is 1.5 μm. Italicized digits number the samples with differently sized supercells: *1* — 1440 nm, *2* — 1600 nm, *3* — 1760 nm, and *4* — 1920 nm.

metasurfaces operating by reflection. They consisted of metallic (gold) nanoparticles located at some distance from a continuous reflecting metal film. For example, the authors of Ref. [47] used rectangular nanoparticles, shown in Fig. 20a. The thickness of the dielectric layer that separated them from the reflecting film was $t_s = 50$ nm, and the size of unit cells $l = 240$ nm. The thickness of the nanoparticles was $t = 50$ nm, and their length and width (L_x and L_y) varied from 30 to 220 nm. The operation wavelength was $\lambda = 800$ nm.

The phase of a reflected wave was given by matching nanoparticle sizes L_x and L_y. Figure 20b presents calculated indices of reflection from a meta-atom, depending on particle's size under periodic boundary conditions. Another peculiar feature of the chosen reflection scheme was a rather weak dependence of reflected wave on intensity L_x and L_y. The curves in Fig. 20b depict phases of the reflected wave. The blue and green curves correspond to TM and TE polarizations, respectively. At the intersections of these curves the points of symmetry are marked at which TM- and TE-polarized waves experience reflection either symmetrically (squares) or antisymmetrically (circles). Figure 20c presents an antisymmetric metasurface reflecting the waves of TM and TE polarizations at the same angle but in different directions. A unit cell of this metasurface is composed by two identical meta-atoms. The difference in wave phase changes between neighboring unit cells equals $\pi/3$.

Results of experiment and computation suggest that a normally incident wave is reflected at an angle of 16.1°. The calculated field strength of a reflected wave resulting from TM-polarized wave with $\lambda = 800$ nm falling normally on the metasurface is shown in Fig. 20d. At this wavelength, a given diffraction lobe has a maximum intensity. The reflected wave

is slightly distorted due to the presence of other diffraction lobes. Figure 20e shows diffraction lobe intensity plotted versus the wavelength. It follows that the diffraction lobe with $m = 1$ has maximum intensity at $\lambda = 800$ nm, whereas other lobes are suppressed; in other words, the metasurface efficiency at this wavelength reaches the highest value. Results of calculations give evidence that this scheme of metasurface realization permits reaching an efficiency up to 80%. In experiment, a 50% efficiency was achieved. Moreover, the metasurface realized in this way operates in a quite wide wavelength range.

References [45, 49] reported reflecting metasurfaces with meta-atoms of various shapes. However, their efficiency was not higher than that of metasurfaces with rectangular meta-atoms. In the end, the rectangular shape (see Fig. 20) proved most favorable in terms of simplicity and efficiency. Moreover, rectangular nanoparticles can be used to create metasurfaces suitable for independent control of TM- and TE-polarized light, as was demonstrated in Ref. [47].

An even higher efficiency of metasurfaces was reached in Ref. [43]. The maximum efficiency at the wavelength $\lambda = 800$ nm amounted almost to 80%. The experimental layout, similar to that in earlier studies with unit cells composed of two rectangular nanoparticles each, is shown in Fig. 21a. The metasurface is depicted in Fig. 21b. The dependences of reflected light intensity on the measuring angle were obtained for different angles of incidence and the generalized Snell's law [see formula (3)] was realized. Experimental data are presented at the top of Fig. 21c, and theoretical results at the bottom.

Further development of metasurfaces was based on the utilization of dielectric nanoparticles [10, 51, 55, 79]. A phase
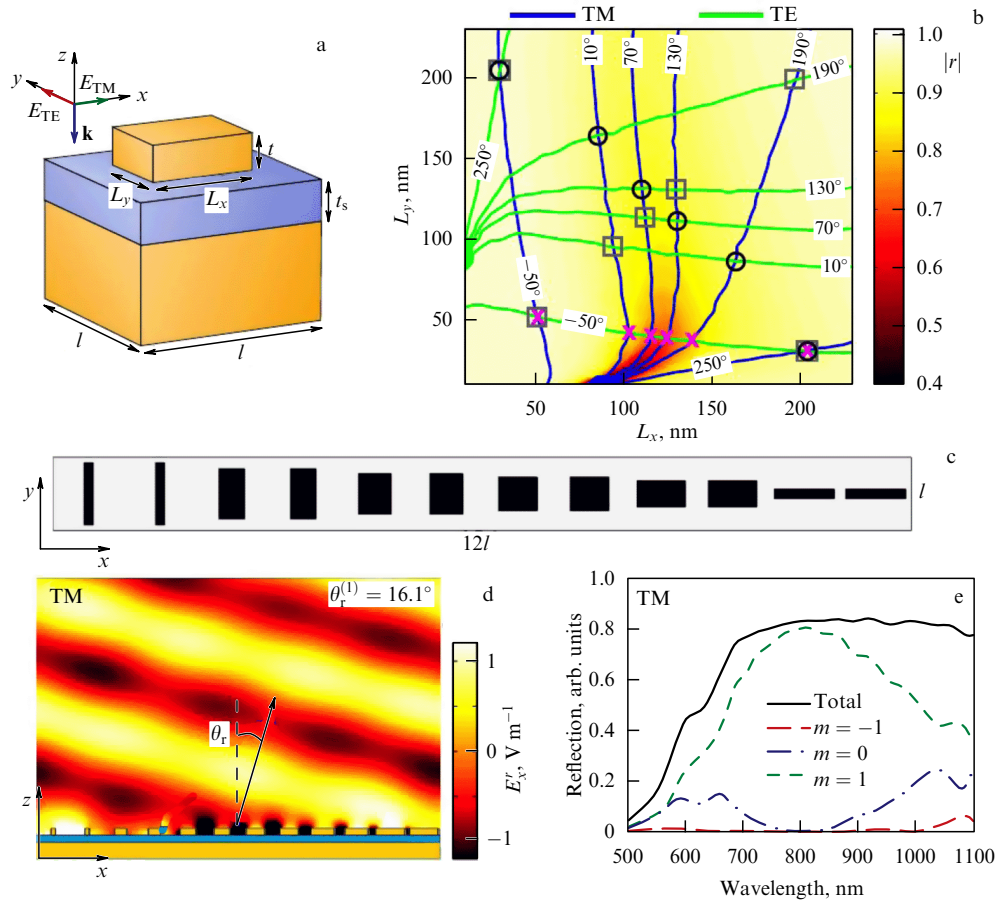
Figure 20. (Color online.) Extraordinary reflection in the reflection scheme (taken from Ref. [47]). (a) A meta-atom formed by a rectangular gold nanoparticle located over a continuous gold film. The nanoparticle and the substrate are separated by a thin dielectric layer. (b) The dependence of reflected wave intensity on the sizes L_x and L_y of the rectangular gold nanoparticle. Green and blue isolines denote reflected light phases for TE (Transverse Electric) and TM (Transverse Magnetic) polarizations, respectively. (c) Supercell composed of six unit cells containing two identical meta-atoms each. (d) Field strength of a wave reflected from the metasurface. The wave fell normally on the surface and reflected at angle $\theta_r = 16.1°$. (e) Wavelength dependence of the reflection coefficient. Black line is the total coefficient of reflection; red, blue, and green lines are for diffraction lobes $m = -1, 0, 1$, respectively.
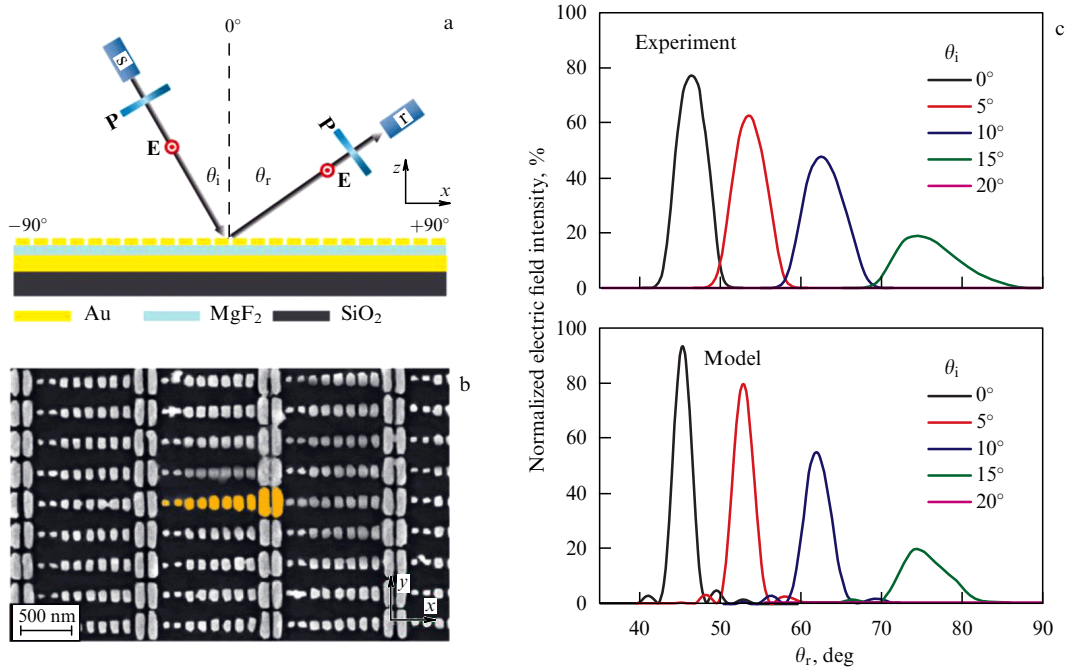

Figure 21. (Color online.) Metasurface realized in Ref. [43]. (a) Layout of experiment on realization of generalized Snell's law. (b) Electron microscope image of the metasurface. (c) Reflected radiation intensity versus θ_r angle at different incidence angles θ_i. Top — experimental data, and bottom — theoretical results.
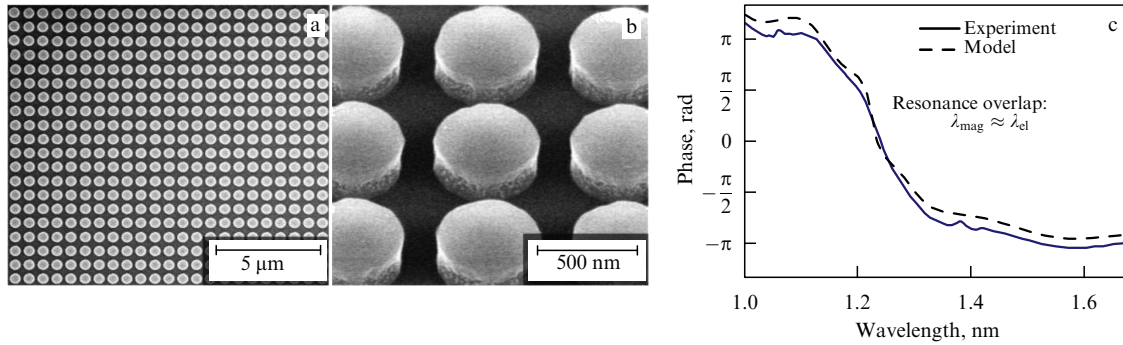
Figure 22. Phase change using a metasurface consisting of an array of identical Si cylinders realized in Ref. [51]. (a, b) Electron microscope images of the metasurface. (c) The phase of transmitted radiation plotted vs wavelength. Cylinder radius $r_d = 242$ nm, and height $h = 220$ nm. Grating constant $a = 666$ nm.

shift on dielectric nanoparticles occurs due to electric and magnetic resonances and their overlap (see Figs 13 and 14). The possibility, in principle, of achieving resonance overlapping and 2π phase coverage using dielectric cylinders was demonstrated in Ref. [51]. Images of the metasurface composed of such cylinders are presented in Figs 22a, b. The size of the Si cylinders was chosen such that electric and magnetic resonance wavelengths coincided. As a result, a change in the wavelength caused a shift in the phase of transmitted radiation, shown in Fig. 22c. Coincidence of resonance frequencies made possible phase changes within a range from 0 to 2π.

A metasurface based on Si cylinders deflecting transmitted radiation was realized in Ref. [10]. Its supercell consisted of eight cylinders with linearly changing radii (Fig. 23a). Laser light was incident normally on the surface, passed through it, and arrived at the camera lens. The intensity of the diffraction lobe with $m = -1$ at the resonant wavelength reached a maximum value (Fig. 23b), whereas the remaining lobes, including the zero one, were suppressed, suggesting $\approx 10°$ angle of refraction. At wavelengths somewhat different from the resonance wavelength, the beam passed unbent. Dependences of transmission coefficients of diffraction lobes on the wavelength of light incident on the metasurface are shown in Fig. 23c. The intensity of the zero diffraction maximum gradually decreased closer to the resonance wavelength and became almost totally suppressed. In contrast, the diffraction maximum with $m = -1$ grew further to the highest value at a wavelength close to the resonance wavelength. The efficiency of such a metasurface was $\approx 45\%$.

A dielectric metasurface from rectangular Si nanoparticles arranged on an SiO_2 substrate was realized in Ref. [55] (see Fig. 24a). Scattering of radiation by rectangular nanoparticles depends on their linear dimensions to a greater extent than scattering by cylindrical ones. On the other hand, the length and the width are two degrees of freedom that make it possible to choose such parameters at which the scattering amplitude is constant and the phase is given arbitrarily. The authors of Ref. [55] calculated parameters of eight nanoparticles at which the scattered light phase of each following particle would be larger by $\pi/4$ than that of the preceding one. The laser beam passed through a polarizer to a beam splitter, as shown in Fig. 24c. Then, two separated beams followed different trajectories, one going through the sample, the other bypassing it. Thereafter, the beams came together again to enter the

camera lens. The images produced by the camera are presented in Fig. 24b. The top image shows the beam that bypassed the metasurface and reached the center. The bottom image depicts refraction of transmitted radiation. The angle of refraction was $13.1°$ at wavelength $\lambda = 1.6$ μm. The efficiency of this metasurface was estimated at 36%.

In addition, Ref. [55] demonstrated the possibility of creating optical vortices with the use of dielectric metasurfaces formed by Si rectangles. Each metasurface consisted of eight sectors changing the phase of the incident light with a $\pi/4$ increment. Images similar to those in Fig. 18 were obtained. The radiation intensity transmitted through the metasurface was 45% of the incident one.

Further development of dielectric metasurfaces was based on the use of Si nanoparticles with a square section placed over a quartz substrate [79]. The height of the silicon particles exceeded their length and width. The equal length and width of the nanoparticles enabled the metasurface to operate regardless of incident light polarization. Laser radiation reached the quartz substrate from below and escaped from the opposite side harboring nanoparticles (Fig. 25a). Scattering from the nanoparticles resulted in beam refraction visible on the screen, as shown in Fig. 25b. The experiment was carried out with the radiation at different wavelengths and demonstrated that the metasurface caused light dispersion. A change in the wavelength from 550 to 710 nm made the light beam of the first diffraction lobe deflect by 17.8 to $26.4°$. Diffraction efficiency, i.e., the ratio of intensity of the first diffraction lobe to that of all lobes taken together, reached a maximum value of 93% at $\lambda = 670$ nm. However, the transmission coefficient at this wavelength did not exceed 30%. As a result, the metasurface efficiency at $\lambda = 670$ nm was below 28%.

3.2 Experimental realization of metasurfaces based on the Pancharatnam–Berry phase

Apart from the theory of Pancharatnam–Berry phase control, Ref. [57] has demonstrated the possibility of controling the wavefront. The dependences of light transmission and reflection on the angle of incidence were obtained and the generalized Snell's law (11) was realized.

The circularly polarized light was incident on a metasurface comprising nanorods (Fig. 26a) The supercell of this metasurface was formed by eight nanorods, each turned through its own angle φ to ensure a phase shift of the reemitted wave possessing reverse polarization: $\Delta\Phi = 2\varphi$ [see formula (23)].
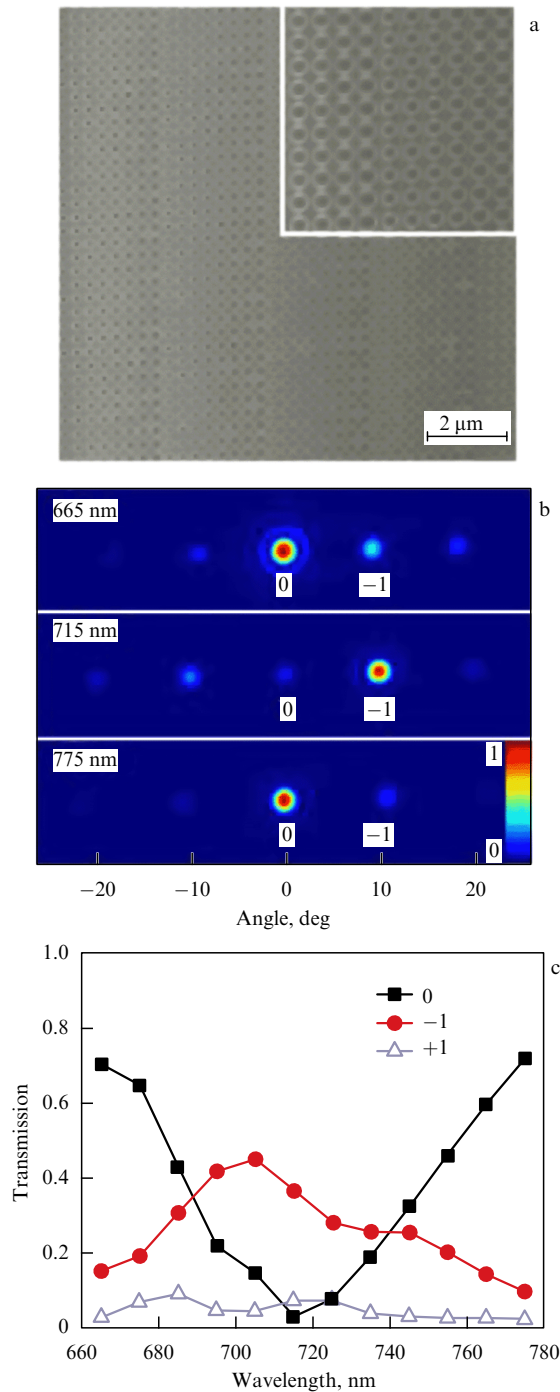
Figure 23. (Color online.) Radiation control using a metasurface consisting of Si cylinders (from Ref. [10]). (a) Electron microscope image of the metasurface. The supercell is composed of eight 130-nm high cylinders with a radius from 120 to 155 nm. (b) The beam was transmitted through the metasurface. Radiation of 665 and 775 nm incident normally to the surface passes almost without distortion. At the resonant wavelength (715 nm), the intensity of the diffraction lobe with $m = -1$ is maximum, while the remaining lobes are suppressed. (c) The dependence of transmission coefficients for three diffraction lobes.

The intensity of radiation transmitted through the metasurfaces was recorded at different angles. The metasurface-scattered light consisted of two waves, one with the same polarization as the incident wave, the other with opposite polarization. Results of computer simulation for the left-polarized wave are presented in Fig. 26b showing the

dependence of radiation intensity on the incidence and transmission angles. Intensity maxima produce lines characterizing the relationship between the incidence and transmission angles. One of the lines passing through the center corresponds to the left-polarized wave refracted in accordance with conventional Snell's law. The more intense line above it corresponds to the right-polarized wave refracted following the generalized Snell's law.

Triangles in Fig. 26b fit experimental data on the incidence angle dependence of the transmission angle for radiation with left-hand polarization. There is excellent agreement between theory and experiment for both conventional and generalized Snell's laws. Moreover, the lines in the upper-left and lower-right corners of Fig. 26b correspond to additional diffraction lobes, i.e., $n = \pm 1$ in formula (11). Calculations and measurements of dependences of the transmission angle on the incidence angle for right-polarized light yielded similar results, but the line corresponding to extraordinary refracted radiation lay below that corresponding to ordinary refraction

Reference [57] demonstrated the existence of a metasurface based on the properties of the Pancharatnam–Berry phase in a broad spectrum. Figure 26c presents the calculated dependence of the intensity of radiation transmitted through a metasurface on the observation angle and the wavelength. Radiation fell onto the metasurface at a right angle. Triangles in the figure denote experimental values of transmission angles. Clearly, the metasurface operates in a broad spectrum, and the angle of refraction shows the dispersive dependence on the radiation wavelength.

3.3 Experimental realizations of nonlinear metasurfaces

The second-harmonic generation on a metasurface can be of value for many applications (see Section 4.4), but its efficiency thus far leaves much to be desired. This accounts for a large number of experimental and theoretical studies on second-harmonic generation and enhancement of its efficiency. Such generation occurs in a variety of nanoparticles with broken symmetry.

References [80–83] describe the generation of second-harmonic radiation using nanoparticles of various shapes, viz. L-shaped, T-shaped, V-shaped, and U-shaped. Images of meta-atoms used in these studies are presented in Figs 27a–c. Nonlinear generation strongly depends not only on the size and shape of the meta-atoms, but also on their mutual arrangement and distances between them. References [66, 67, 84, 85] were designed to evaluate the influence of interparticle distances on generation efficiency (Figs 27d–f). Moreover, the generation of second-harmonic radiation can also be achieved by using holes in a metal film, as shown in Refs [86, 87].

The efficiency of generation of second-harmonic radiation, i.e., the ratio of radiation power at a doubled frequency to the starting radiation power, is rather low. To increase it, some authors made use of paired meta-atoms consisting of vertically aligned metal particles [68, 88], as shown in Fig. 27g. In this case, a contribution to generation comes not only from the dipole but also from the quadrupole and magnetic dipole moments of the particles. In Ref. [68], generation efficiency amounted to $\eta_{max} = 1.32 \times 10^{-10}$ at the incident radiation power $P_{FW} = 5$ mW, which corresponds to nonlinear coefficient $\gamma_{eff} = 2.6 \times 10^{-8}$ W^{-1}. Another way to enhance second-harmonic generation efficiency reduces to placing an active element, like a diode, between the nanoparticles, as proposed
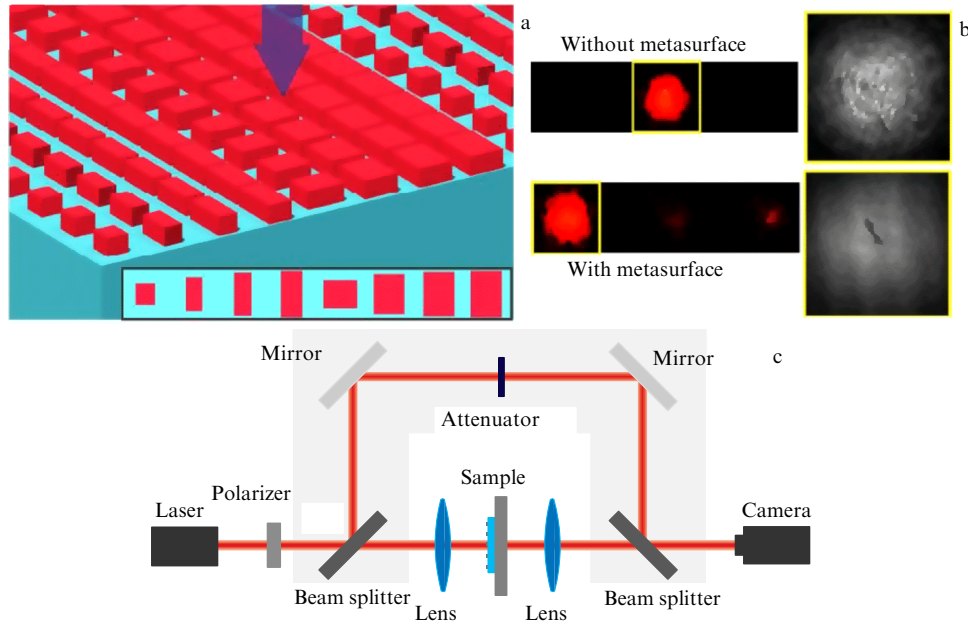
Figure 24. (Color online.) Realization of the dielectric metasurface with the aid of rectangular Si nanoparticles on an SiO$_2$ substrate [55]. (a) The supercell is formed by parallelepiped-shaped nanoparticles. The total size of the metasurface is 96×96 μm. The length and width of 270-nm high particles varied from 250 to 750 nm. Grating constant $a = 800$ nm. Working wavelength $\lambda = 1.6$ μm. (b) An image from a CCD (charge-coupled device). Top: an image obtained without the metasurface; bottom: an image of radiation transmitted through the metasurface. (c) Layout of experiment with the use of a Max–Zehnder interferometer. The laser beam passes the polarizer and enters the beam splitter. Then, it either passes through the metasurface or bypasses it. Thereafter, the two beams come together again to enter the camera lens.
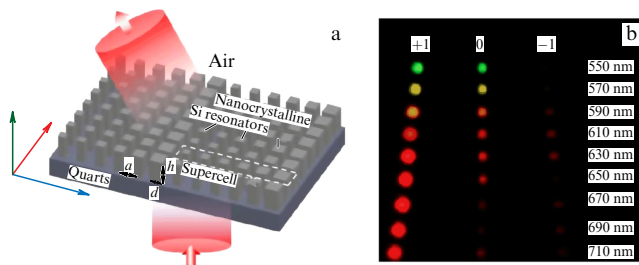

Figure 25. (Color online.) Realization of the metasurface from Si nanoparticles on a quartz substrate [79]. (a) The supercell of the metasurface is formed by parallelepiped-shaped nanoparticles. Grating constant $a = 300$ nm; nanoparticle height $h = 370$ nm; the side of the square section d varied from 110 to 210 nm. (b) An image obtained with the camera. The beam deflected by $17.8°$ to $26.4°$ upon a change in the wavelength from 550 nm to 710 nm.

in Ref. [70]. The maximum radiation conversion efficiency reached $\eta = 4.36 \times 10^{-6}$ at incident radiation intensity $I_0 = 1$ GW cm^{-2} (in a pulse). The nonlinear coefficient could not be calculated due to the absence of data on the focused beam area.

Metasurfaces operating with circularly polarized radiation also exhibit nonlinear properties. For example, the authors of Refs [89, 90] investigated the properties of nonlinear chiral (twisted) metasurfaces (Fig. 27h).

Nonlinear dielectric metasurfaces capable of improving the efficiency of second-harmonic radiation have recently become available [74, 91, 92]. Reference [91] reports the efficiency $\eta = 8 \times 10^{-5}$ at the fundamental harmonic power $P_{FW} = 1$ mW (radiation intensity $I_0 = 7$ GW cm^{-2}), corresponding to the nonlinear coefficient $\gamma_{eff} = 8 \times 10^{-2}$ W^{-1}. The maximum efficiency $\eta = 2 \times 10^{-5}$ ($P_{FW} = 5$ mW and $\gamma_{eff} = 4 \times 10^{-4}$ W^{-1}) was reached in work [74].

Of special interest is work on electromagnetic radiation frequency conversion with the use of active metasurfaces [93–95], where second-harmonic radiation was generated by virtue of photon absorption by heterostructures located beneath plasmonic nanoparticles and subsequent re-emission of photons at a doubled frequency (Fig. 28a). Quantum wells in the heterostructures were adjusted so that the energies of electron resonance levels corresponded to these photons. The band diagram of a heterostructure is presented in Fig. 28b.

The bands were matched so that two photons at a fundamental frequency were absorbed by electrons, first occurring at the intermediate level and then moving to the upper one. Thereafter, the electrons were transferred to the lower level, while emitting photons with a doubled energy. In this case, the mean level of the quantum heterostructure underwent a 25-meV shift to reduce optical losses in the resonator and avoid saturation of the nonlinear optical response. A plasmonic nanoparticle functioning as a resonator shows up in two modes. The fundamental mode was tuned to horizontally polarized radiation incident on the metasurface, while the second-harmonic mode was tuned to vertically polarized radiation. The calculated electric field strengths of these modes are presented in Fig. 28c. The horizontally polarized wave falls on the resonator and is absorbed by the heterostructure. Thereafter, excited electrons emit photons at a doubled frequency, which interact with the vertical resonator. This results in second-harmonic emission of the vertically polarized wave. The metasurface absorption spectrum is displayed in Fig. 28d.

The metasurface thickness in Ref. [94] was 25 times smaller than the radiation wavelength, and the maximum frequency conversion efficiency amounted to $\eta = 7.5 \times 10^{-4}$ at incident radiation intensity $I_0 = 15$ kW cm^{-2}. Here,
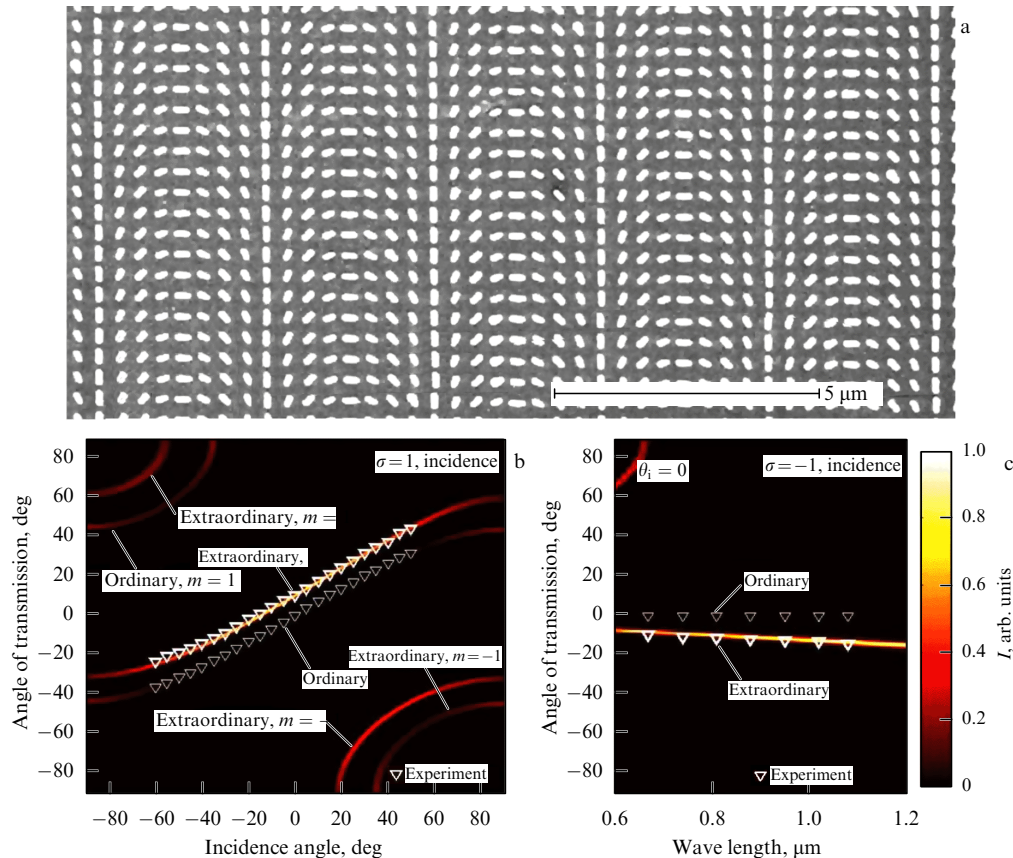
Figure 26. (Color online.) Demonstration of the generalized Snell's law based on the Pancharatnam–Berry phase [57]. (a) Electron microscope image of a metasurface with a supercell of eight meta-atoms, each in the form of a nanorod turned through a certain angle. (b) Theoretical dependence of transmitted radiation intensity on the incidence and transmission angles. Triangles denote experimental data. (c) Calculated dependence of transmitted radiation intensity I on the wavelength and angle of transmission. Radiation fell normally on the surface. Triangles denote experimental data.

incident wave intensity is much lower than in earlier papers using the passive metasurfaces: the power of the second harmonic in active metasurfaces does not obey the law (25), and its intensity does not increase as the square of intensity of the incident wave. Second-harmonic generation efficiency reaches a maximum at a pumping power much smaller than that the structure can sustain. A further increase in the pumping power markedly reduces generation efficiency.

Second-harmonic generation by active metasurfaces is equally feasible for circularly polarized radiation. In such a case, a turn of a meta-atom can control the Pancharatnam–Berry phase described in Section 2.2.3. This property allowed the authors of Refs [96, 97] to control the direction of the second harmonic in the far field in accordance with the generalized Snell's law [see formula (4) in Section 2.1]. Moreover, the second-harmonic generation power of an active metasurface can be controlled by varying voltage applied to the heterostructure. In Ref. [98], voltage thus applied to the heterostructure controlled the concentration of electrons in quantum wells. It made possible the modulation of second-harmonic generation pulses by varying the voltage. The response time of an optical pulse was less than 10 ns.

4. Applications of metasurfaces

Metasurfaces are compact devices intended for control of light in a practically arbitrary fashion, opening up highly promising prospects for their application in a variety of

optical instruments. Several such applications are considered in the present section. The development of certain tools, e.g., metalenses, have already been finalized, whereas others remain to be designed.

4.1 Metasurface-based flat lenses (metalenses)

The ability of metasurfaces to control both phase and amplitude offers vast opportunities for radiation control. Specifically, it makes possible the creation of lenses of subwave thickness. Reference [99] was one of the first studies dealing with metasurface-based flat lenses. Such lenses are frequently called metalenses. Metasurfaces described in work [99] consisted of V-shaped nanoparticles and were used in the framework of the cross-polarization scheme. At the beginning, computer simulation was employed to calculate the relationship between the phase of the field scattered by a nanoparticle and its parameters (Fig. 29a). Eight nanoparticles were selected with the scattered radiation phase encompassing the 2π range. These nanoparticles made up a metalens (Fig. 29). Meta-atoms were adjusted so as to ensure the hyperbolic phase profile of scattered radiation along the lens plane. The scattering phase was defined as

$$\varphi_{\mathrm{L}}(x,y) = \frac{2\pi}{\lambda}\left(\sqrt{(x^2+y^2)+f^2}-f\right), \qquad (27)$$

where x and y — nanoparticle coordinates at the lens, λ — radiation wavelength, and f is the lens focal distance. This phase profile enabled waves emitted from all points of the lens
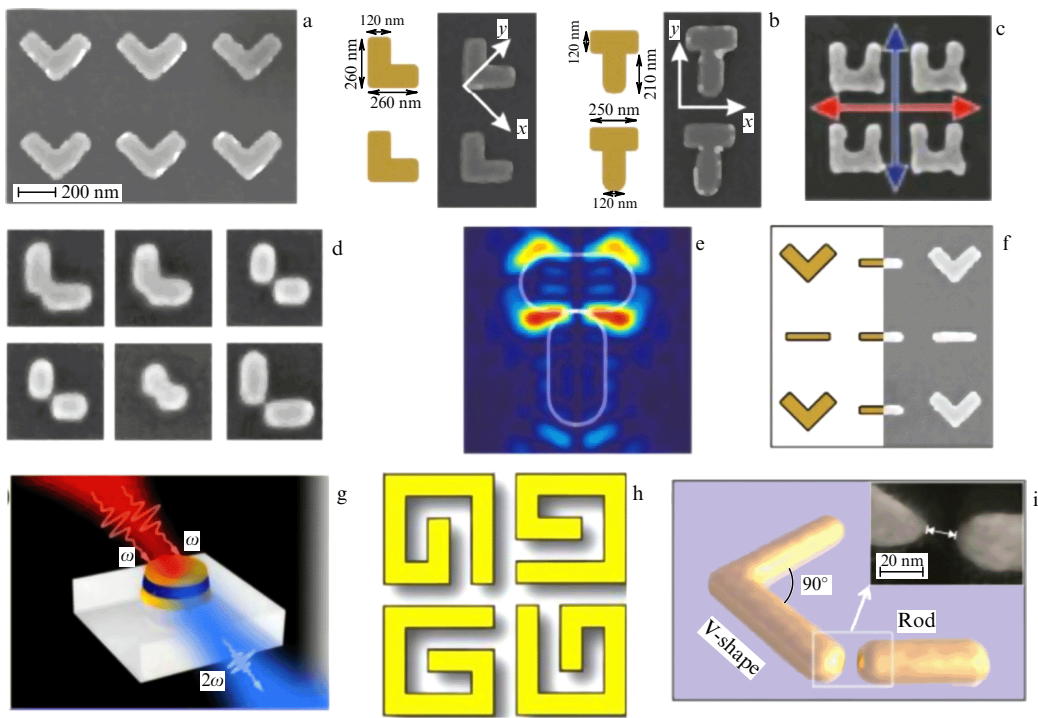
Figure 27. (Color online.) Various meta-atoms in nonlinear metasurfaces with broken central symmetry tapped to generate the second harmonic: (a) V-shaped nanoparticles [81]. (b) L- and T-shaped nanoparticles [69]. (c) U-shaped nanoparticles [83]. (d) Meta-atoms consisting of two perpendicular nanorods [67]. (e) Results of numerical simulation of field distribution in study [66] where perpendicular nanorods served as meta-atoms. (f) Composite meta-atom from Ref. [85] in which the influence of a passive element (horizontal nanorod) between two nonlinear V-shaped nanoparticles on second-harmonic generation was evaluated. (g) A meta-atom from Ref. [88] concerning second-harmonic generation from paired nanoparticles. (h) Chiral (twisted) meta-atoms [89]. (i) A composite meta-atom tapped for symmetry breaking and second-harmonic generation [75].

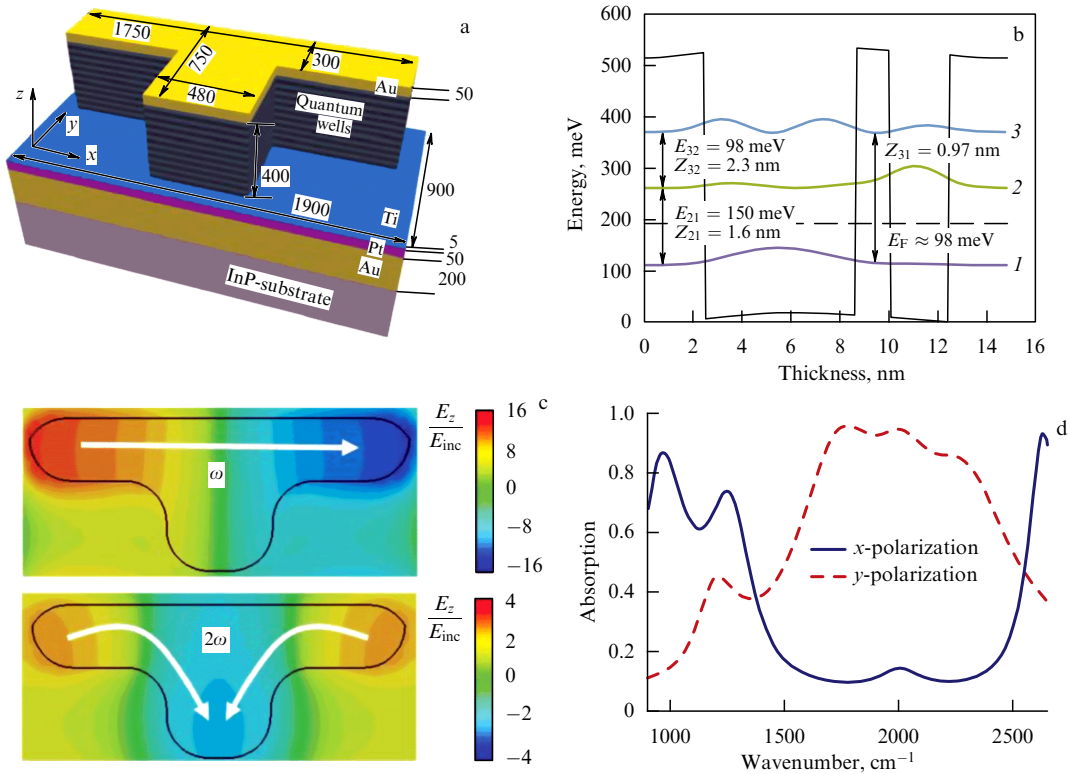**Figure 28.** (Color online.) Active nonlinear metasurface [94]. (a) An active meta-atom of such a surface formed by a two-mode plasmonic nanoparticle located on the heterostructure. Dimensions are given in nanometers. (b) Band diagram of a heterostructure with three bands in the discrete spectrum. (c) The fundamental mode of the nanoparticle and the second-harmonic mode. (d) Metasurface absorption spectrum for two polarizations.
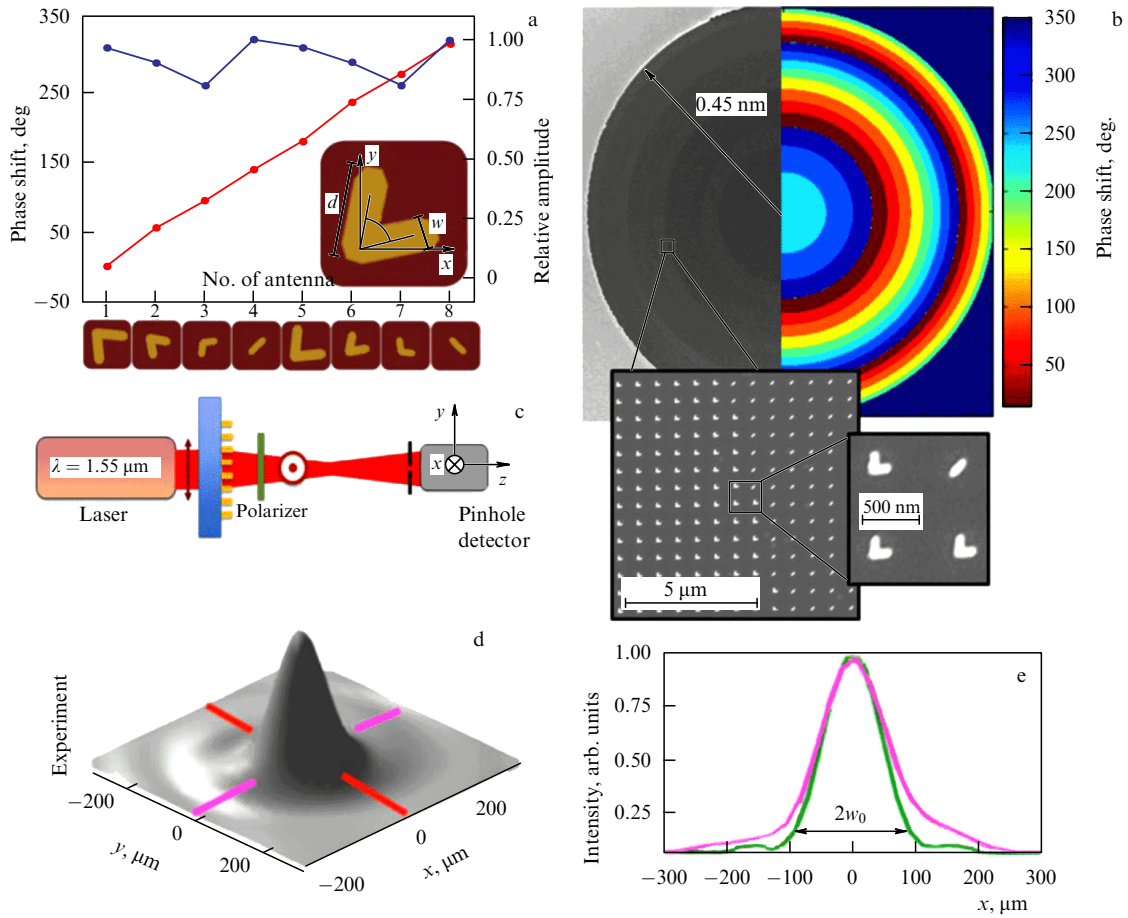
Figure 29. (Color online.) Radiation focusing by a metasurface-based flat lens in the cross-polarization setup [99]. (a) The dependence of scattering phase and amplitude on particle geometry. Several degrees of freedom allow covering phases within 2π and retain the roughly constant scattering amplitude. The dimensions d of 50-nm thick particles varied from 85 to 180 nm. (b) Electron microscope image of a flat lens. Each nanoparticle scatters radiation with a predetermined phase. Lens radius 0.45 mm, grating constant 500 nm, and focal distance 6 cm. (c) Experimental layout. Polarized light falls onto the flat lens; it is then transmitted through the polarizer and focused. The detector measures field intensity at an arbitrary point in space. (d, e) Coordinate dependence of radiation intensity within the lens focal distance. The 0.9-mm beam is focused onto a spot $2w_0 = 200$ μm in diameter. The radiation wavelength $\lambda = 1.55$ μm.
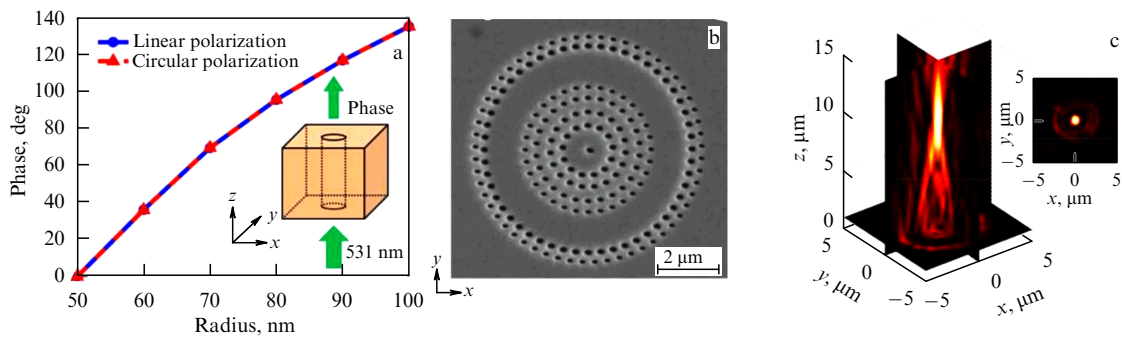

Figure 30. (Color online.) Focusing a plane wave by a lens made from a thin gold film with holes of various diameters in Ref. [107]. (a) The dependence of the phase of radiation transmitted through nanoholes on the hole radius. Changes in the radius make possible π phase coverage. The operation wavelength $\lambda = 531$ nm. (b) Electron microscope image of the lens. The gold film is 380 nm thick. (c) Focused radiation intensity distribution. Lens focal distance $z = 10$ μm.

to reach its focus in identical phases. Each point at the lens harbored a nanoparticle, in accordance with the calculated phase. The lens radius in Ref. [99] was 0.45 mm (Fig. 29b). A laser beam passed through the flat lens and the polarizer behind it, to be focused on a given point in space. A mobile radiation detector was used to scan the field strength, as shown in Fig. 29c. Two lenses with focal lengths of 6 cm and 3 cm, respectively, were made. The dependence of radiation intensity on coordinates at the lens focal length is illustrated in Figs 29d, e. The lens with the focal length of 6 cm focused the laser beam onto a spot $2w_0 = 200$ μm in diameter (Fig. 29e), while the lens with the focal length of 3 cm focused
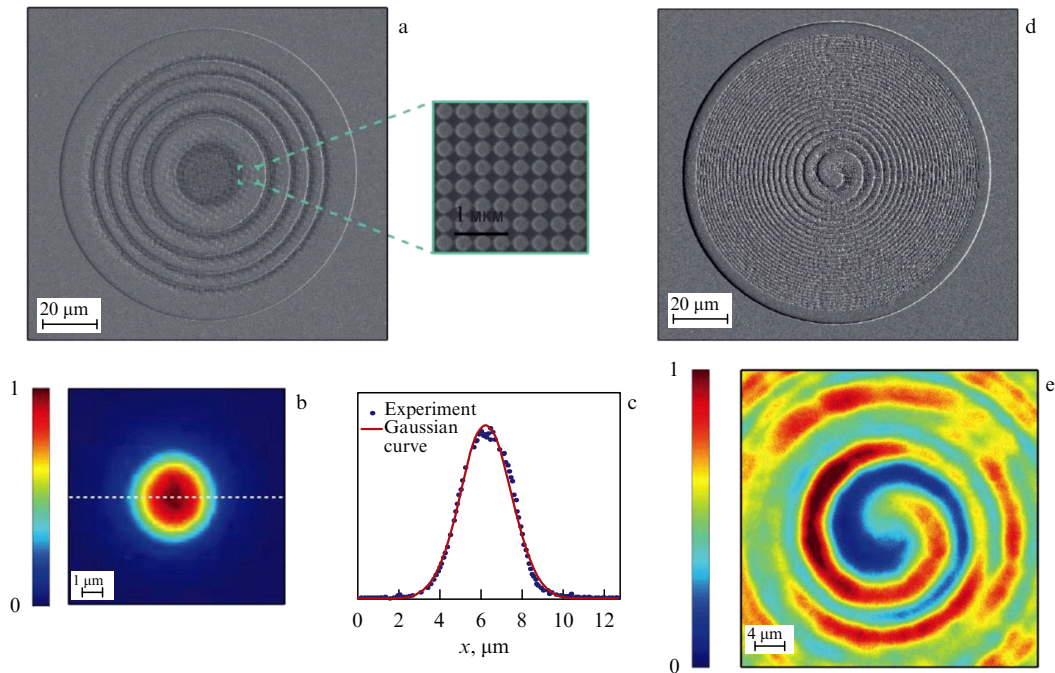
Figure 31. (Color online.) Flat lenses created in Ref. [25]. (a) Electron microscope image of a focusing lens. Meta-atoms are 633-nm high cylinders with 96- and 221-nm radii. Distance between cylinder centers 443 nm. (b, c) Field intensity distribution over the focal length. Blue points — experimental data. Red line — Gaussian curve. Measurements were made at $\lambda = 633$ nm. Lens focal distance $f = 250$ μm. (d) Lens forming an optical vortex. (e) Intensity distribution of optical vortex field.

the beam onto a spot 100 μm in diameter. Lens efficiency was estimated at 1%.

Such a setup with V-shaped nanoparticles and cross-polarization was implemented in Ref. [100], where radiation at $\lambda = 676$ nm was focused onto a spot 630 nm in diameter comparable to the wavelength. The focusing efficiency was roughly 10%, i.e., somewhat higher than in the previous study.

Diffraction optics had made considerable advances much before the advent of metasurfaces. Fresnel zone plates have found wide application for focusing X-rays [101] and other kinds of radiation [102, 103]. Equally successful were designers of photon sieve lenses [104–106]. Phase control in diffraction optics is exercised by the proper positioning of holes or zone plates in space. The advent of metasurfaces gave rise to investigations using a combination of zone plates and resonances. For example, the authors of Ref. [107] controlled the phase of radiation transmitted through the lens by varying the hole diameter. Figure 30a presents the dependence of the phase of radiation transmitted through a hole in a 380-nm thick gold film on the hole radius. Changes in the radius made possible almost π phase coverage. Due to incomplete 2π coverage, the holes had to be placed only in odd Fresnel zones, as shown in Fig. 30b. Radiation at the wavelength $\lambda = 531$ nm was focused within 10 μm of the lens (Fig. 30a), and that with a wavelength of 488 nm or 647 nm within 8 and 12 μm, respectively.

The idea of applying the nanoholes was further developed in Ref. [108], where complete phase coverage was slightly expanded by using rectangular holes and nonlinear properties of metasurfaces. Radiation at the wavelength $\lambda = 633$ nm was focused within a distance of 30 μm, with the gold film thickness being 250 nm.

Recently, a number of studies have been published concerning lenses based on metasurfaces composed of meta-atoms in the form of dielectric nanoparticles [25, 109–113]. The principles of the operation were identical in all these cases. For example, the flat lens used in Ref. [25] consisted of Si cylinders placed on a quartz substrate (Fig. 31a). The cylinders exhibited both electric and magnetic resonances. Changes to cylinder diameter made possible a phase control of radiation by taking advantage of the mutual position of the resonances within a range from 0 to 2π. The phase of the meta-atoms was calculated in relation to coordinates using a formula analogous to expression (27). A few flat lenses with the following optimal parameters were engineered: a cylinder height of 633 nm for the wavelength $\lambda = 633$ nm, the distance between cylinder centers of 443 nm, and cylinder radii of 96–221 nm for 2π phase coverage. They allowed radiation to be focused onto a small spot within $f = 250$ μm from the lens with an efficiency of 40% (Fig. 31b); in other words, spot intensity amounted to 40% of intensity for radiation incident on the lens. Lens transparency was estimated at 90%. The radiation intensity distribution depending on one of the coordinates in the focal plane is shown in Fig. 31c. The measured intensity curve and the Gaussian curve were 95 percent identical.

Reference [25] demonstrated optical vortex-forming lenses, besides collecting lenses. An electron microscope image of one of these lenses is presented in Fig. 31d. The light vortex image (Fig. 31e) was obtained within a distance of 100 μm. It is worthy of note that the use of cylindrical nanoparticles in Ref. [25] made it possible to manufacture light polarization-independent lenses.

Lenses based on dielectric nanoparticles show a higher efficiency than those based on metallic V-shaped particles. Moreover, the former are insensitive to light polarization and do not need an application of additional tools, whereas the latter operate only with linearly polarized waves and require
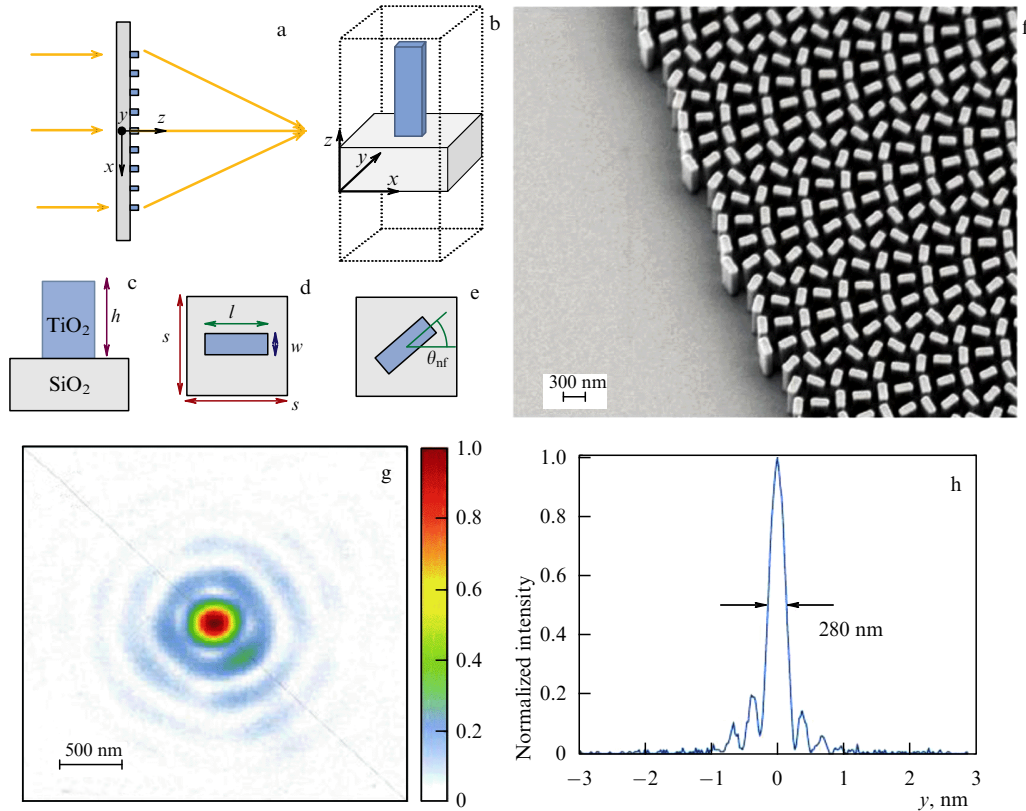
Figure 32. (Color online.) Focusing radiation with the aid of a metalens [77]. (a) A plane wave is incident onto a lens 2 mm in diameter made of rectangular dielectric materials. Transmitted radiation is collected over the lens focal distance $f = 0.725$ nm. (b–e) Lens meta-atoms in the form of TiO_2 parallelepipeds were placed on a glass substrate. The lens is optimized for operation at the wavelength $\lambda = 405$ nm, nanoparticle height $h = 600$ nm, length $l = 150$ nm, and width $w = 40$ nm. Elementary cell size $s = 200$ nm. A turn of a particle through the angle θ_{nf} in a range from 0 to π ensures 2π phase shift coverage. (f). Electron microscope image of part of the metalens. (g, h). Radiation intensity distribution over the lens focal distance.

additional polarizers to be used. It is worthwhile to note that neither type of lens is free of chromatic aberration. The dependence of the lens focal distance on the incident radiation wavelength was measured in Refs [25, 100].

Dielectric nanoparticle-based metalenses can also operate in a wider range. For instance, Ref. [114] reports a metalens made of TiO_2 nanocolumns working within a broad visible spectrum of 60 nm. Such metalenses are discussed in more detail in Section 4.2.

One more type of lens makes use of the Pancharatnam–Berry phase jump and circularly polarized incident radiation. Phase changes in such lenses are unrelated to the wavelength; their meta-atoms can be either metallic [115, 116] or dielectric [77, 117] nanoparticles. The highest performance of lenses was achieved in Ref. [77] where TiO_2 meta-atoms on a glass substrate were utilized. Three such lenses were prepared for 405-, 532-, and 660-nm radiation. The lenses were 2 mm in diameter, and had a focal distance of 0.725 mm. Figure 32a presents a schematic of focusing a plane wave onto a point. Meta-atoms of the lens were parallelepipeds, shown in Figs 32b–e. The nanoparticles had length l, width w, height h, and intercenter distance s chosen to match each particular wavelength. A turn of a nanoparticle through an angle θ_{nf} (Fig. 32e) ensured a phase shift within a 0 to 2π range. A metalens represented actually a set of parallelepipeds (Fig. 32f), each capable of shifting phase. The shift was calculated using formula (27). Radiation was focused onto a spot whose radius was shorter than the wavelength

(Figs 32g, h). Lens efficiency was 86% for the wavelength $\lambda = 405$ nm, 73% for $\lambda = 532$ nm, and 66% for $\lambda = 600$ nm. Moreover, the lenses were used to obtain optical images of gaps and holes in a thin film, which were smaller in size than the incident radiation wavelength.

Considerable progress has recently been achieved in the development of metalenses. For convenience, here are their main characteristics borrowed from different publications and summarized in Table 1. Clearly, the efficiency of lenses has significantly increased since the time of the first metalens. It is especially high in TiO_2-based lenses, although they operate with a circularly polarized light. Equally successful is work designed to improve the performance of silicon-based lenses.

4.2 Multiresonant metasurfaces and lenses based on them

Metalenses and other optical devices are characterized by strong dispersive aberration, because the angle of radiation refraction depends on the wavelength [see formulas (3) and (11)]. Moreover, control of light by resonances may be realized in a rather narrow spectrum due to a small resonance width. Almost all the aforementioned publications report experiments carried out at a single wavelength. These drawbacks can be made up for.

Reference [119] describes metalenses based on changes to the Pancharatnam–Berry phase. A circularly polarized plane wave was incident on a metalens comprising meta-atoms in the form of rectangular holes in a gold film. Rotation of the

Table. Characteristics of metalenses according to various studies.

Half-width/λ [1]	Efficiency [2]	Polarization	Material of meta-atoms	λ, nm	Thickness/λ	Year	References
~ 33	1 %	Linear	Au	1550	0.038	2012	[99]
0.93	10 %	Linear	Au	676	0.044	2013	[100]
~ 2	Unreported	Polarization-independent	Au (holes)	531	0.72	2013	[107]
9.7	5 %	Circular	Au	740	0.05	2013	[116]
1.2	Unreported [3]	Circular	Si	550	0.18	2014	[117]
~ 10	70 %	Polarization-independent	Si	850	0.56	2014	[113]
~ 65	~ 35	Polarization-independent	Si	1550	0.33	2014	[118]
2.15	~ 0.8 %	Circular	Au (holes)	632.8 [4]	0.19	2015	[119]
2.8	Unreported	Linear	Au (holes)	633	0.39	2015	[108]
100	70.8 %	Polarization-independent	Si	4800	0.61	2015	[109]
2.4	82 %	Polarization-independent	Si	1550	0.65	2015	[110]
0.69	86 %	Circular	TiO$_2$	405	0.67	2016	[77]
~ 10	5 %	Circular	Au	880	0.045	2016	[115]
1.93	65 %	Polarization-independent	Si	1550 [5]	0.46	2016	[111]
~ 6.3	40 %	Polarization-independent	Si	633	1	2016	[25]

[1] The half-width is that of the peak (in units of wavelength) on the coordinate dependence of radiation intensity in the focal plane (Fig. 32h).

[2] Because certain publications have demonstrated several lenses operating at different wavelengths, the highest experimental efficiencies are listed.

[3] 45 % diffraction efficiency at a wavelength of 550 nm. Diffraction efficiency is the ratio of intensity of the main diffraction maximum to overall intensity of all maxima.

[4] Experiment at four different wavelengths: 405, 532, 632.8, and 785 nm.

[5] Dual-range lens for the wavelengths 1550 and 915 nm with 65 % and 22 % efficiency, respectively.

holes about their axes caused a change in the phase encompassing a 2π range. Phase fitting of all meta-atoms allows collecting radiation onto a point within a certain focal distance from the lens. Phase changes by meta-atoms of such lenses were shown to weakly depend on the radiation wavelength, but the dispersion characteristic of light direction remained unaltered and resulted in a wavelength dependence of the focal distance, as shown in Fig. 33a depicting the distribution of the intensity of radiation transmitted through the metasurface in the plane of the main optical axis at different wavelengths λ. The dashed straight line indicates the focal plane. The distance between the lens and the focal plane f decreases with increasing wavelength. The light distribution in the focal plane remains practically the same for different λ (Fig. 33b). The dependences in Fig. 33b are normalized to unity. Their absolute values are significantly different, because the coefficient of light transmission through the holes in the film depends on the wavelength. Similar results were obtained in Ref. [120].

Metasurfaces based on the Pancharatnam–Berry phase operate in a wide wavelength range of circularly polarized radiation. They possess chromatic aberration, i.e., their focal distance depends on the wavelength. The authors of Ref. [13] proposed and implemented a method to get rid of chromatic

aberration. Specifically, radiation of different wavelengths was deflected through the same angle. It follows from formula (4) that dispersion is compensated for if the metasurface phase is inversely proportional to the wavelength:

$$\varphi(x, \lambda_i) = -\frac{2\pi}{\lambda_i}\, x \sin\theta_0\,, \qquad (28)$$

where λ_i is the set of wavelengths at which the metasurface operates, θ_0 is the required angle of deflection of the radiation direction from the normal, and x is the coordinate along the metasurface.

A unit cell of the metasurface was formed by two rectangular dielectric nanoparticles, as shown in Fig. 34a. Notice that the supercell is absent here, i.e., there is no periodically recurring set of unit cells. The structure is aperiodic. The one-dimensional metasurface consists of 240 1-μm long Si meta-atoms aligned in a row on a glass substrate (see the inset to Fig. 34d). Each meta-atom exhibits three resonances at different wavelengths.

Figure 34b illustrates the wavelength dependence of the scattering cross section showing resonances corresponding to the frequencies at which the metasurface operates. A change in the wavelength near any resonance alters the phase shift, as well as the variation of meta-atom parameters w_1, w_2, and d
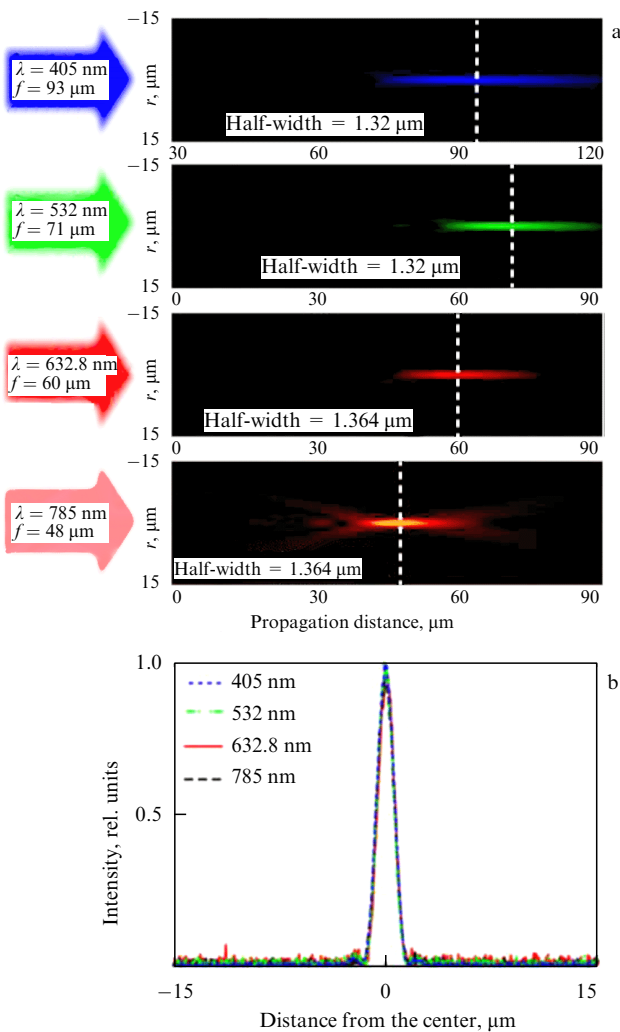
Figure 33. (Color online.) Radiation intensity distribution in optical axis plane (a) and in the focal plane (b) at different wavelengths. An increase in the wavelength λ causes a reduction in the focal distance f. (Taken from Ref. [119].)

does at a fixed wavelength. Rectangular nanoparticles are quite close to one another, which enhances the role of interaction between them. It is therefore difficult to construct a model describing the influence of meta-atom parameters on the radiation phase shift at all three wavelengths.

Different values of w_1, w_2, and d were considered to choose the necessary phase in Ref. [13], so as to ensure that their sum is smaller than the size of a unit cell. In the end, a metasurface was selected that satisfied condition (28) for three wavelengths: $\lambda_1 = 1300$ nm, $\lambda_2 = 1550$ nm, and $\lambda_3 = 1800$ nm. Each resonance exhibited dispersion (the angle of deflection depended on the wavelength, as shown in Fig. 34c) and deflected light at these wavelengths to the same angle, $\theta = -17°$. Neighboring resonances also deflected radiation to a specific angle, but their contribution was much smaller than that of the nearest resonance. The dependences of radiation intensity on the observation angle for the three wavelengths are plotted in Fig. 34d. All these dependences show the main peaks corresponding to the same angle and additional maxima of lower intensity attributable to the contribution from neighboring resonances. The metasurface efficiency was 9.8, 10.3, and 12.6% for the λ_1, λ_2, and λ_3 wavelengths, respectively.

Reference [13] presents, in addition to refraction of normally incident light, the concept of a flat lens with the focal distance equal for the three wavelengths. The structural principle of such a lens remains the same, viz. the phase shift at different wavelengths must compensate for dispersion, and meta-atoms must be paired rectangles. This idea was implemented in Ref. [121]. A one-dimensional (or cylindrical) lens was optimized for the three wavelengths. Radiation at 1300, 1550, and 1800 nm was focused at the same distance $f = 7.5$ mm with an efficiency of 15, 10, and 21%, respectively. Lens diameter was 600 μm, and the focused spot size around 30 μm.

Two-dimensional lenses capable of focusing radiation at two different wavelengths based on the same structural principle were described in Refs [111, 122]. Meta-atoms (or metamolecules already) of the lens were formed by several dielectric nanoparticles. In Ref. [111], a metamolecule consisted of two types of silicon cylinders having markedly different diameters. Large-diameter cylinders exhibited resonance at $\lambda_1 = 1550$ nm, and small-diameter ones at $\lambda_2 = 915$ nm. Because bigger cylinders had a greater scattering cross section, each of the metamolecules comprised three small cylinders per single large one. The metamolecules were packed into the hexagonal grating shown in Fig. 35 with constant $a = 720$ nm and cylinder height 718 nm. The lens, 300 μm in diameter, focused 1550-nm laser light onto the focal plane with a 65% efficiency, and 915-nm radiation with an efficiency of 22%. The half-width of the focused spot was equal to 2.9 and 1.9 μm, respectively. The same authors [122] used a metalens with meta-atoms of two types: large and small cylinders exhibiting resonance at different wavelengths. The meta-atoms were grouped into sectors as follows: meta-atoms of one type for $\lambda_1 = 1550$ nm in the interval from 0 to 45°, those of the other type for $\lambda_2 = 915$ nm in the interval from 45° to 90°, then again meta-atoms of the first type in the interval from 90° to 135°, etc. The efficiency of such a metalens was approximately equal to that of a previous one.

Meta-atoms allow differential control of differently polarized light. This property can be employed to create metalenses focusing radiation of different wavelengths onto one point. For example, Ref. [13] describes a metasurface-based lens with meta-atoms in the form of elongated aluminum rods. Some of them, directed horizontally, control only the phase of horizontally polarized light, while others, directed vertically, control only the phase of vertically polarized light. This concept provided a basis for designing a lens capable of focusing radiation at different wavelengths, $\lambda_1 = 650$ nm and $\lambda_2 = 460$ nm, and different polarizations within the same focal distance.

4.3 Metasurface-based holograms

Holography came into being in the mid-twentieth century. A usual photograph retains the trace of a light wave amplitude focused by the lens onto the film in the form of a two-dimensional image. A hologram contains information about light phase and amplitude, and thereby allows a three-dimensional (3D) image to be obtained. Holograms of real objects are most frequently prepared as described by Denisiuk or Leith and Upatnieks. Both methods make use of interference between object wave and reference wave. The former irradiates the object of interest and is reflected from it to interfere with the reference wave on a photographic plate, thus giving rise to an intricate three-dimensional relief corresponding to the distribution of electromagnetic energy
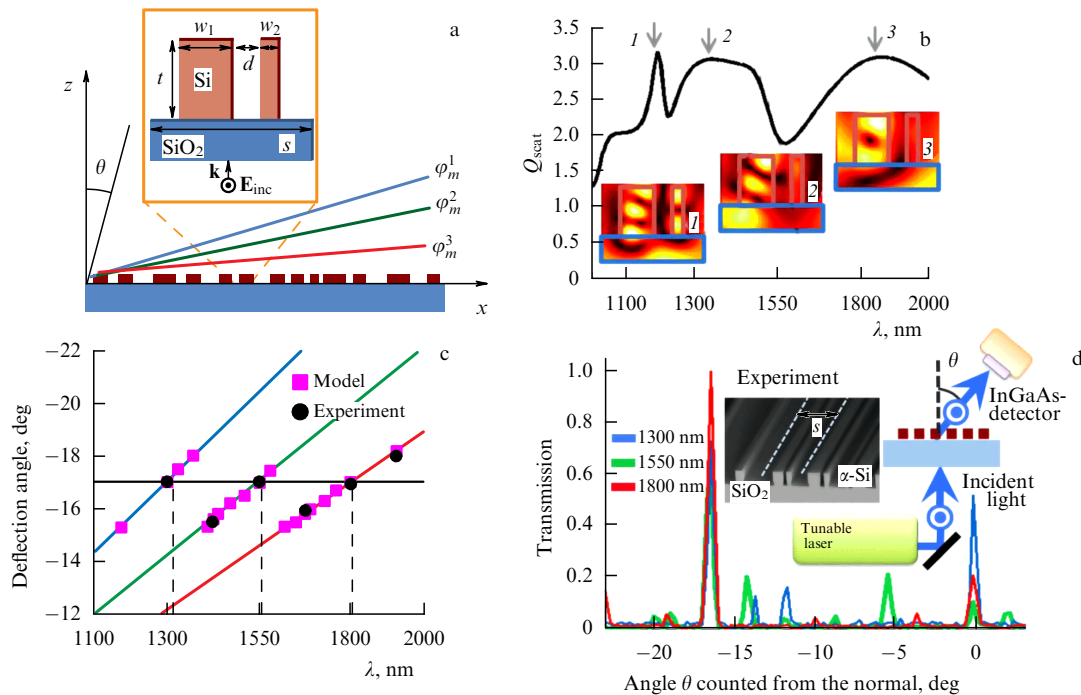
Figure 34. (Color online.) Metasurface realized in Ref. [13], which refracts radiation at various wavelengths by the same angle. (a) Unit cell consisting of two rectangular dielectric particles. Three degrees of freedom (w_1, d, and w_2) allow selecting the necessary phase for three wavelengths. (b) The wavelength dependence of scattering efficiency Q_{scat}. Dimensionless quantity Q_{scat} is defined by the ratio of the scattering cross section (having the dimension of length in the two-dimensional case) to the total block length $w_1 + w_2$. The meta-atom exhibits three resonances at different wavelengths, for which distributions of electric field intensities $|\mathbf{E}|^2$ are shown in the insets. (c) Wavelength dependences of the angle of refraction for various resonances. (d) Dependences of the intensity of radiation transmitted through the metasurface on the observation angle. The metasurface deflects 1300-, 1550-, and 1800-nm radiation by the angle $\theta = -17°$. Insets: Electron microscope images of the metasurface and experiment layout.
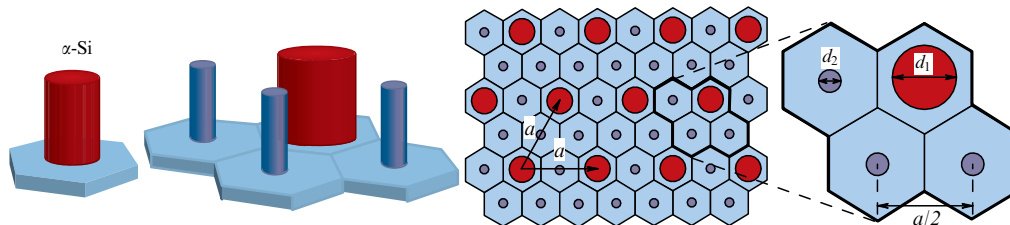

Figure 35. Lens metasurface designed in Ref. [111]. Its meta-atom (or metamolecule) consists of four nanocylinders. There are three small cylinders per single large one in a metamolecule.

in a given region in space. If this region is irradiated by a wave close to the reference one, the reflected wave acquires a relevant phase, by virtue of a varied plate relief depth, and becomes more like the object wave. As a result, the observer will see with a certain degree of accuracy such light as that reflected from the object.

Modern computer technologies make it possible to obtain phase and amplitude distributions from virtual models. A 3D printer then prints the three-dimensional relief of the calculated hologram. The light reflected from the hologram depicts the virtual three-dimensional object.

The cell size in a hologram exceeds the radiation wavelength, which accounts for the appearance of diffraction submaxima and reduction of hologram diffraction efficiency. Metasurfaces are promising candidates for the development of future holographic technologies, because their meta-atoms are smaller in size than radiation wavelengths. Moreover, meta-atoms are capable of efficient light phase and amplitude control.

One of the earliest studies [124] demonstrating the possibility, in principle, of creating metasurface-based holograms made use of the Pancharatnam–Berry phase. The authors first designed a few micron-scale 3D virtual jet model. Phase distribution in a given flat region of space was calculated in Ref. [125]. For simplicity, phase was the only variable on the hologram surface, while amplitude remained constant. Meta-atoms of the hologram surface were nanorods, each turned through its own angle, as shown in Fig. 36. Circularly polarized light passing through such meta-atoms acquired a phase shift $\Delta\Phi = 2\theta$. Rotation of the rod ensured phase coverage within 2π. Consequently, setting the angle θ for each meta-atom allowed the entire calculated phase portrait to be reproduced. As a result, the observer behind the metasurface could see the three-dimensional image of the previously created virtual aircraft model. The metasurface area comprised 800×800 meta-atoms, with a grating constant of 500 nm. The relatively small number of meta-atoms in the hologram prevented the observer from seeing the image at
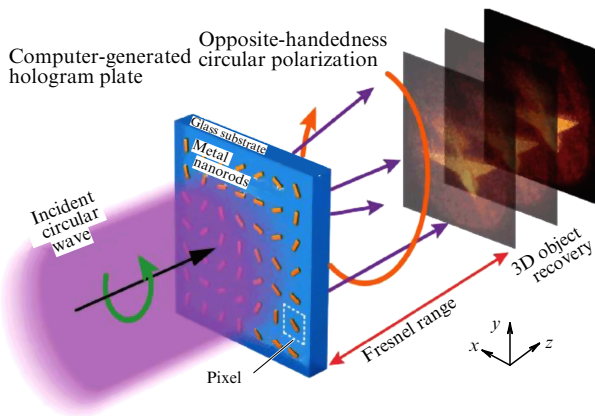
Figure 36. (Color online.) Demonstration of 3D holography in Ref. [124]. Circularly polarized light is incident on a metasurface. Each meta-atom imparts its own pre-calculated phase to the wave. As a result, a three-dimensional image appears at a certain distance from the metasurface.

different angles. Therefore, the authors of paper [124] invoked a different method (described below) to prove that they actually obtained a hologram producing a three-dimensional image.

The three-dimensional image of a jet was formed at a certain distance from the hologram. The objective of the microscope was focused on this region and could displace the focal point to and from, as shown in Fig. 36. In this way, the lens could be focused on different, close or distant, parts of the object. For example, short-range focusing produced a sharp image of the jet's nose, whereas the tail was slightly blurred. The reverse picture was observed for long-range focusing. The authors of paper [124] interpreted this situation as evidence that metasurfaces are suitable for displaying three-dimensional objects.

Even more convincing evidence of three-dimensionality in the images of objects is the capability to obtain their images at different angles. The same authors of Ref. [124] report virtual helical images (Fig. 37a) formed by point-like objects. The metasurface-based hologram displayed a three-dimensional image. In this case, the objective of the microscope was turned through different angles. The images obtained at five inclination angles of the microscope objective are presented in Fig. 37b. These far-from-ideal images nevertheless suggest three-dimensional viewing.

Many studies on metasurface-based holograms have recently been published. In all of them, meta-atoms control the radiation phase so as to form the necessary wave front. Meta-atoms of holograms utilize a variety of phase control mechanisms. High efficiencies of holograms amounting to 59 and 80% were obtained on reflecting metasurfaces irradiated by circularly polarized light in Refs [15, 126], respectively. These holograms were generated by manipulating the Pancharatnam–Berry phase. Other reflecting holograms based on resonance transform linearly polarized radiation into a holographic image [127, 128]. Numerous publications deal with holograms making use of transmitted light to form an image. Good efficiency (over 78%) was reached using TiO_2 dielectric metasurfaces altering the Pancharatnam–Berry phase [129]. A lower efficiency was reported for Si metasurfaces [130]. A large number of dielectric holograms working in a transmission mode form the wave front using resonances [131–133]. Metallic nanoparticles can also serve as a basis for holographic metasurfaces working in transmission. They can control phases taking advantage of both resonances for linearly polarized radiation [128, 134] and the Pancharatnam–Berry phase [124, 135, 136] for circularly polarized light. Moreover, there are holograms having a metasurface in the form of holes in a metal film. They can also control phases of light by means of resonances [137, 138] or the Pancharatnam–Berry phase [139].

For simplicity, in most studies on holographic metasurfaces, meta-atoms controlled only the phase of light without affecting its amplitude. However, meta-atoms have a greater degree of freedom than that and afford vast opportunities for light control. Suffice it to say that meta-atoms are capable of controling not only the phase but also the amplitude. In certain studies [136, 137, 139], meta-atoms controlled both the phase and the amplitude to improve an image quality. Moreover, the high degree of freedom of meta-atoms allows obtaining various images at various polarizations of light incident on hologram [126, 128, 140]. The size of nanoparticles influences resonant frequencies. As a result, meta-atoms with differently sized nanoparticles form different images at different wavelengths, which makes it possible to have color holographic pictures [127, 132, 139]. An additional degree of freedom is possible to obtain as well making use of the nonlinear effect on meta-atoms. Specifically, Ref. [135] reports various holographic images from a single metasurface at the second-harmonic frequency, while Ref. [141] describes holographic images at
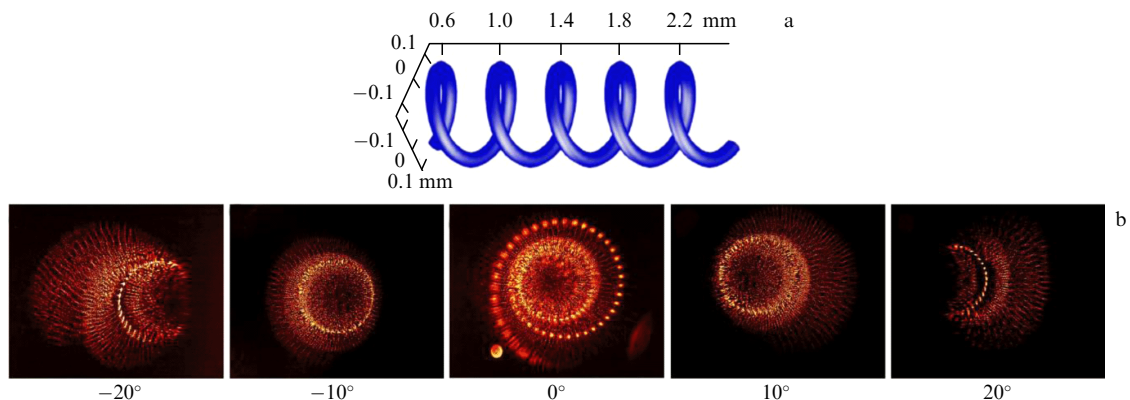

Figure 37. (Color online.) (a) 3D helical model from Ref. [124]. (b) Holographic images of helices obtained at different angles.
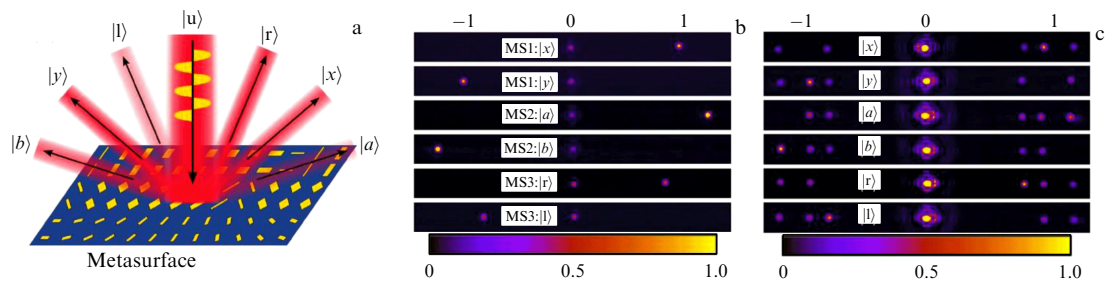
Figure 38. (Color online.) Determining light polarization [143]. (a) Polarization detector concept. The metasurface consists of three types of supercells, each reflecting light of a given polarization at a certain angle. (b) An image from a reflected-light camera. Results for three metasurfaces (MSI, MS2, and MS3), each consisting of identical supercells. (c) An image of radiation reflected from the composite metasurface comprising supercells of three types. Light polarizations are as follows: $|x\rangle$ and $|y\rangle$ — horizontal and vertical polarizations, $|a\rangle$ and $|b\rangle$ — diagonal polarizations, $|r\rangle$ and $|1\rangle$ — right- and left-hand polarizations. The wave incident on the metasurface has arbitrary (unknown) polarization $|u\rangle$.

the third harmonic. Nonlinear properties are considered in more detail in Section 4.4.

Thus far, the highest hologram efficiency has been achieved in Ref. [142] at a radiation wavelength of 1600 nm. The metasurface comprised 865-nm high silicon columns from 79 to 212 nm in radius. The grating constant was 750 nm, hologram size 0.75 mm, hologram diffraction efficiency 99%, and metasurface transparency 90%. A high-quality monochrome image 5 mm in size formed 10 mm from the metasurface.

4.4 Other applications of metasurfaces

Metasurfaces offer unique opportunities for control of light on a subwave scale, which accounts for a variety of their applications in optical instruments described in Sections 4.4.1–4.4.6, although there remains much to be done to reach a degree of their perfection comparable to that of lenses and holograms.

4.4.1 Polarizers. Radiation of various polarizations scatters differently from meta-atoms, which creates a basis for designing instruments having the ability to determine light polarization [143–145]. Reference [143] describes the employment for this purpose of a metasurface consisting of supercells of three types operating in a reflection mode. Supercells of each type reflected light of a given polarization at a specific angle, as shown in Fig. 38a. At the beginning, three metasurfaces were manufactured, each comprising supercells of a single type, either MSI, MS2, or MS3, that reflected light of a certain type at their own angles (Fig. 38b). MS1 reflected horizontally and vertically polarized light ($|x\rangle$ and $|y\rangle$) at one angle, MS2 reflected diagonally polarized light ($|a\rangle$ and $|b\rangle$) at a different angle, and MS3 changed the Pancharatnam–Berry phase and reflected circularly polarized light ($|r\rangle$ and $|1\rangle$) at a third angle. The detector-metasurface consisted of alternating supercells of the three types that reflected radiation of one type or another at a certain angle. Such a metasurface reflected polarized light at different angles and the possibility appeared to determine the polarization of incident radiation from reflection maxima (Fig. 38c). This metasurface exhibited the highest efficiency for 800-nm radiation and could aid in retrieving polarization characteristics in a wavelength range from 700 to 1000 nm. To recall, 50% of radiation is reflected into the zero diffraction maximum and carries no information about polarization.

Metasurface-based lenses can just as well serve as polarizers. For example, Ref. [146] presents an image of a beetle obtained with the aid of a filter-metalens of circular polarization (Fig. 39). The insect's body surface reflected left-hand-polarized light and absorbed right-hand-polarized radiation. It was illuminated with monochrome light. The camera image was focused by a Pancharatnam–Berry phase-based metalens (Fig. 32). Such lenses operate with circularly polarized light and simultaneously serve as polarization filters focusing only either left-hand-polarized or right-hand-polarized light. The left and right panels of the figure present the image in left- and right-hand-polarized light, respectively.

Metasurfaces can also find applications as light polarization converters [39, 147–150]. By way of example, Ref. [39] demonstrated the possibility of creating a metasurface from V-shaped nanoparticles that forms a circularly polarized wave from a linearly polarized wave. The light acquired circular polarization during extraordinary transmission through the metasurface (Fig. 40a). It was composed from two supercells displaced relative to each other and translated in a periodic manner (see Fig. 40b). Degree of transmitted light polarization was close to unity (Fig. 40c). The intensity of the extraordinary transmitted beam at a wavelength of 7.7 µm reached 30–40% of that of ordinary reflected radiation. Because light incident on the metasurface is partly transmitted and partly absorbed, the overall intensity of the circularly polarized wave is only 10% of the incident wave intensity. Reference [148] describes a reflecting metasurface capable of rotating the polarization plane through 90° with an efficiency of 97%.
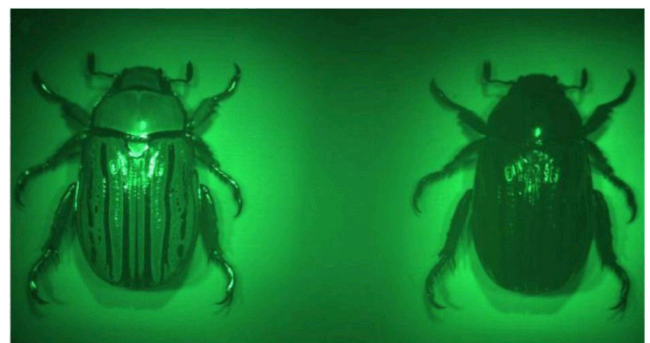

Figure 39. (Color online.) Image of a beetle produced with a metalens [146]. The metalens also served as a filter of circularly polarized light. Left and right parts of the figure present the image in left- and right-hand-polarized light, respectively.
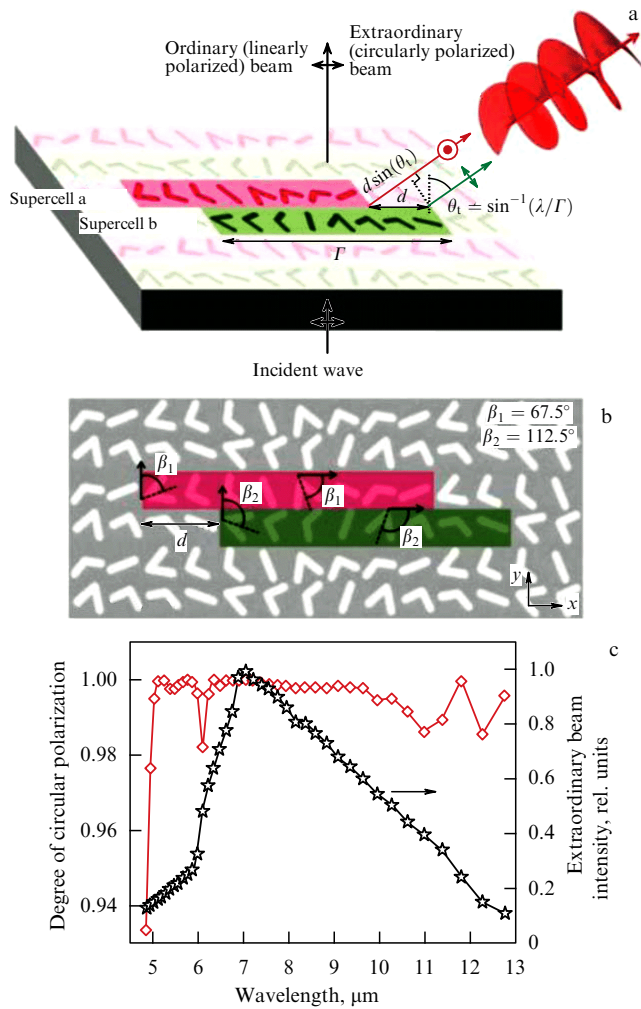
Figure 40. (Color online.) Conversion of linearly polarized light into circularly polarized light [39]. (a) Diagram illustrating conversion. The linearly polarized light is incident on the metasurface and passes through it in an extraordinary direction. The transmitted wave becomes circularly polarized. (b) Metasurface consisting of two supercells displaced relative to each other and translated in a periodic manner. (c) Wavelength dependence of a degree of polarization (red curve) and intensity (black curve) of extraordinary transmitted radiation.

An efficient polarizer based on a reflecting metasurface was developed in Ref. [151]. Its meta-atoms were formed of

aluminum nanorods arranged over a metal film onto which linearly polarized radiation fell. Reflected light rays, each with its own polarization (four linearly and two circularly polarized), propagated in six directions.

Metasurfaces with intricately shaped nanoholes have even more degrees of freedom for polarization control. Reference [152] describes a metasurface based on a metal film with chiral nanoholes that allowed polarization in each of the diffraction rays not only to be controlled but also to be converted (from circular into linear and back).

4.4.2 Optical diodes. Optical diodes make up important elements of many optical systems due to their ability to transmit light incident on one side of the structure, but not on the other side. Such devices are usually made of magnetic elements violating the reciprocity principle (Faraday effect), which makes them robust by convention. Metasurfaces can be applied to design very compact optical diodes. A combination of perforated gold nanofilms and planar photonic crystals was employed in Refs [153, 154] to demonstrate the enormous asymmetry of transmission of light incident on a metasurface from different sides.

4.4.3 Color printing and dyes. Metasurfaces based on electric and magnetic resonances operate in a narrow radiation spectrum. Extension of the operating frequency range is a serious challenge facing developers of metasurfaces. The narrow range has advantages and disadvantages. Certain authors have used meta-atoms as color filters for so-called plasmonic dyes [155]. For example, in Ref. [156], white light fell onto a metasurface composed of alumina crosses that served as filters. Transmitted light was found to change color, depending on the light polarization angle.

The parameters of nanoparticles determine the color of a scattered light, which opens up a new sphere of metasurface applications — color printing. In Refs [157–160], the color of scattered light was controlled by plasmon resonances on nanoparticles. Reference [157] describes a 50×50-μm image (Fig. 41b) with 'pixels' represented by nanocolumns, each formed by three disks: gold, silver, and dielectric (Fig. 41a). The disks are, in turn, placed on a gold film that reflects light, like the metasurface reported in Ref. [47]. Light color depends on the diameter of the disks and the distance between them. Figure 41c displays an electron micrograph of the metasurface showing the relationship between nanoparticle diameter and light color. Images generated

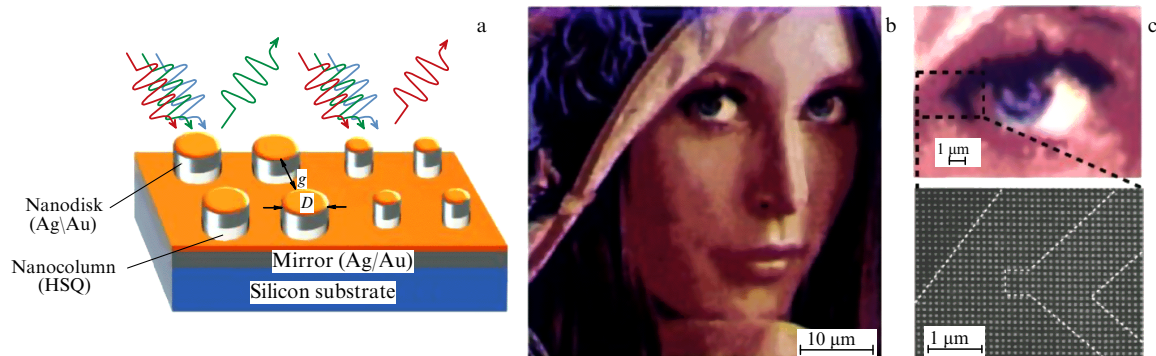**Figure 41.** (Color online.) Color printing of an image with the aid of plasmonic nanoparticles (taken from Ref. [157]). (a) Each 'pixel' of the image represents a composite nanodisk; its diameter and the distance between neighboring meta-atoms determine scattered light color. (b) Far-field image. (c) Part of the image magnified under an electron microscope; image color depends on nanoparticle diameter.
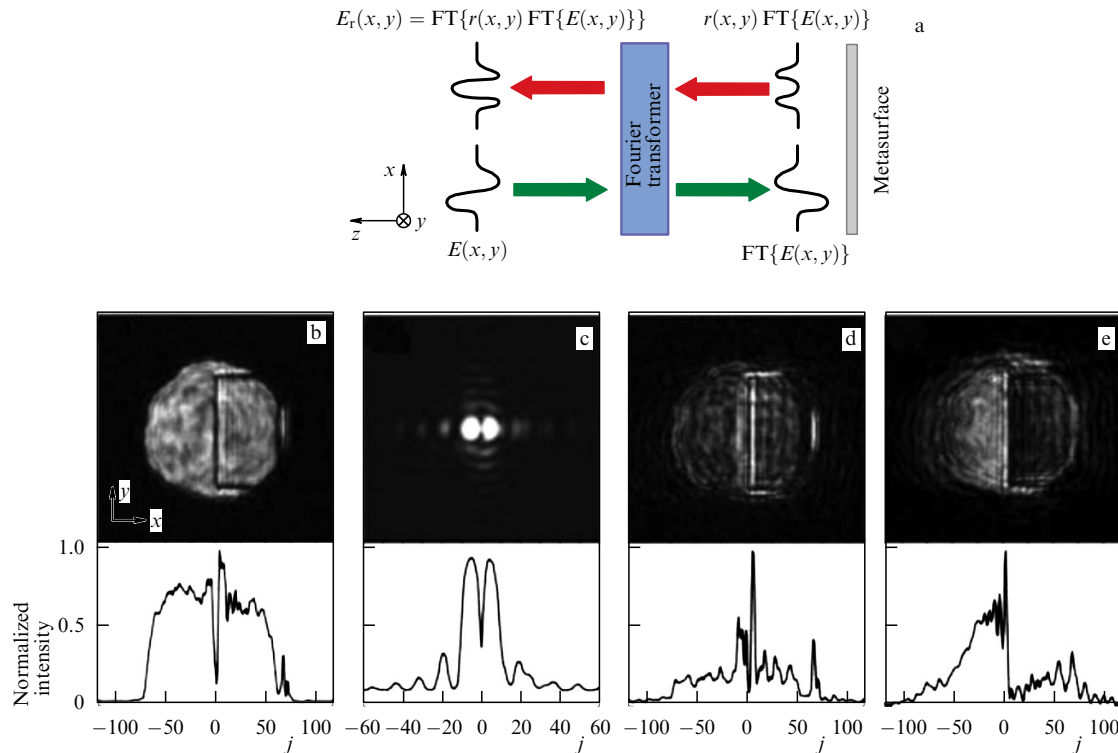
Figure 42. (Color online.) Analog computations based on using metasurfaces [40]. (a) Computation scheme. Initial function $E(x, y)$ is first fed to a Fourier transformer, then to the metasurface to be converted in compliance with function $r(x, y)$ (reflection coefficient). The resultant function undergoes Fourier transformation, too. (b) Initial function $E(x, y)$. (c) Fourier transform of the initial function. (d) Transformation corresponding to differentiation. (e) Transformation corresponding to integration. Bottom portions of figures b–e present dependences of signal intensity received by the camera on pixel number j along the x-axis at $y = 0$.

with the aid of 'plasmonic dye-based colorants' are equally possible to obtain through the application of perforated metal films [161, 162] in which nanohole diameter controls light color.

4.4.4 Calculations based on metasurfaces. The ability of metasurfaces to strictly control both light phase and amplitude in a wide range opens up opportunities for analog computations. The concept of metamaterial-based analog calculations was proposed in Ref. [163]. Reflecting metasurfaces developed in paper [47] were used for this purpose in Ref. [40]. The concept is based on the possibility of representing the dependence of the output function $W(x, y)$ on the input function $f(x, y)$ via the convolution

$$W(x, y) = \int g(x - x', y - y') f(x', y') \, \mathrm{d}x' \, \mathrm{d}y' .$$

The same law is expressed through the double Fourier transform (FT)

$$W(x, y) = \mathrm{IFT}\Big\{ G(k_x, k_y) \, \mathrm{FT}\{ f(x, y) \} \Big\}, \tag{29}$$

where inverse FT (IFT) stands for inverse Fourier transform in coordinates, and $G(k_x, k_y) = \mathrm{FT}\{g(x, y)\}$. Here, the role of the initial function is played by the distribution $E(x, y)$ of the electric field strength of electromagnetic wave in space. This radiation is fed to a lens that implements the Fourier transform $\mathrm{FT}\{E(x, y)\}$. Radiation then falls on the metasurface with a coordinate-dependent reflection coefficient $r(x, y)$ playing the role of the convolution function $G(k_x, k_y)$. The

distribution of the reflection coefficient over the metasurface depends on the operation that needs to be performed on function $f(x, y)$. Specifically, for the differentiation of $f(x, y)$ with respect to x, the reflection coefficient will be proportional to x: $r_{\mathrm{diff}}(x, y) \sim x$. For integration, it should be inversely proportional to x: $r_{\mathrm{int}}(x, y) \sim 1/x$. Radiation reflected from the metasurface is fed back to the lens, which turns the output function into $W(-x, -y)$. Negative signs before arguments are due to the fact that the lens performs a direct but not inverse Fourier transform.

Figures 42b–e illustrate the experimental distribution of those fields playing the role of functions. The initial function shown in Fig. 42b was obtained using a round hole. Then, a lens was involved to produce the Fourier transform presented in Fig. 42c. Figures 42d and 42e display images of light reflected from differentiating and integrating metasurfaces, respectively. The metasurfaces were $50 \times 50\ \mu m^2$ in size, each comprising 40,000 meta-atoms. The figures imply that the analog computation procedure under consideration is still imperfect and the functions are disturbed by noises, partly because meta-atoms scatter light near resonances and the process is highly sensitive to the accuracy of their manufacture. Reference [164] proposed a concept of analog computations on metasurfaces in the cross-polarization scheme, which is expected to enhance computation efficiency, because the reflection coefficient is controlled by nanorod rotation less sensitive to manufacturing inaccuracies.

4.4.5 Supersensitive sensors. Metasurfaces are key elements of supersensitive biosensors [165–168]. Meta-atoms of such metasurfaces are, as a rule, either metallic nanoparticles or

holes in thin films. Extremely strong fields form under resonance conditions near the meta-atoms. Therefore, resonances are very sensitive to minor changes in the refraction index of the medium where they are occurred. A change in resonance is recorded based on the analysis of the reflection spectrum.

Nonlinear properties of metasurfaces can considerably increase sensor sensitivity. The power of second-harmonic generation by means of metasurfaces is rather low. However, the width of second and third harmonic resonances is smaller than that of the fundamental harmonic. Some authors propose using nonlinear properties of metasurfaces together with the high intensity of the local field near nanoparticles and high sensitivity of higher-order harmonic generation to geometry and other nanoparticle characteristics for engineering supersensitive sensors [169–171].

Thus, Ref. [171] describes a sensor capable of determining, based on 3rd harmonic generation, changes in the refraction index of water with the resolution $\Delta n = 10^{-3}$. Figure 43 schematically illustrates finding the refraction index of a medium. Radiation falls onto the metasurface and, in the linear regime (Fig. 43a), there is a peak in the light transmission intensity spectrum. The metasurface is submerged into the liquid containing admixtures that alter its refraction index and resonance of nanoparticles. This causes peak displacement in the frequency dependence of transmission. In the linear scheme (Fig. 43a), the detector tuned to a given frequency records changes in radiation intensity. Figure 43b presents a nonlinear setup for detecting changes in the refraction index that is not substantially different from the linear one, save for the fact that the detector is tuned to the 3rd harmonic of scattered radiation. The intensity peak of the 3rd harmonic is much narrower than that of the 1st harmonic, which makes the detector more sensitive to environmental changes. Experiments in Ref. [171] demonstrated that the nonlinear detection setup is several times more sensitive than the linear one.
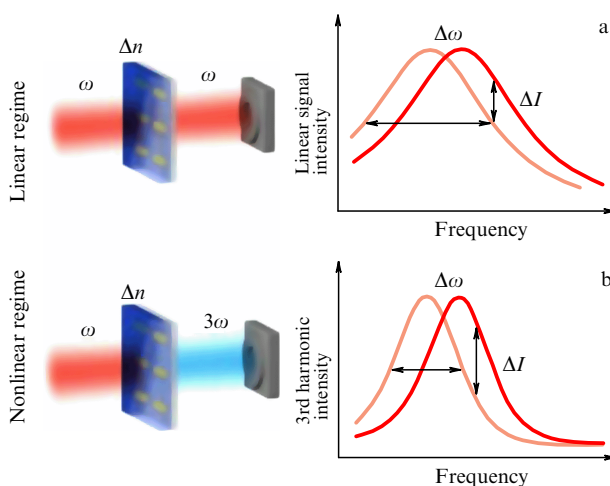

Figure 43. (Color online.) Layout of a third-harmonic sensor (taken from Ref. [171]). (a) Schematic of the sensor operating in a linear regime. (b) Schematic of the sensor operating in a nonlinear regime. Resonance peak in the dependence of transmission intensity on the 3rd harmonic radiation frequency is narrower than that for the 1st harmonic, which increases the sensitivity of the nonlinear sensor.
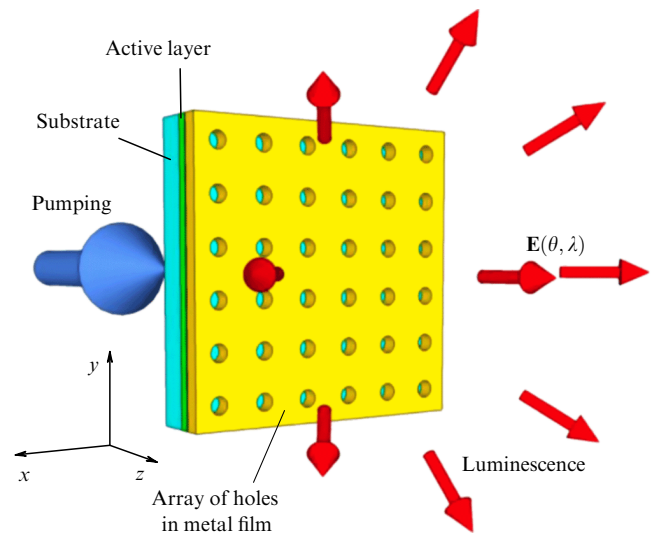

Figure 44. (Color online.) Schematic representation of a spaser utilizing metasurface as the resonator [177].

4.4.6 Miniature metasurface lasers.

Resonators are indispensable components of lasers, maintaining positive feedback and generation of selected modes. The work of resonators is based on multiple light reflection (e.g., a Fabry–Perot resonator). A standing wave or resonant mode is formed between the reflecting surfaces, if a whole number of half-waves fits into this space. Therefore, the size of a resonator cannot be smaller than the radiation half-width, which prevents unrestricted reduction of laser dimensions.

As shown in Section 2.2, metasurfaces composed of meta-atoms exhibit resonances and can serve as resonators. The meta-atoms being much smaller than the wavelength, such surfaces can be used to design miniature nanolasers. Arrays of both nanoparticles [172–175] and nanoholes in thin films [176–179] were employed as resonators in experiments. Because of plasmon resonances developing on metal nanoparticles and nanoholes, such lasers are called spasers.

Figure 44 gives a schematic representation of a spaser utilizing a metasurface as the resonator [177]. The metasurface prepared from nanoholes in a thin gold film lies 20 nm above the InGaAs active layer coating the substrate. The active layer is pumped from the side of the substrate by laser light with a shorter wavelength. Luminescence occurs on the metasurface side.

5. Methods of metasurface simulations

Metasurfaces are composite three-dimensional structures formed by meta-atoms of various sizes and shapes. Only a few problems can be solved analytically [22, 180]. In most studies, numerical simulation is used, requiring huge computational resources. To calculate an electromagnetic field, the finite element method and the finite difference method in the time domain are most commonly resorted to. Both techniques have advantages and disadvantages. Many authors [47, 68, 100, 133, 161] prefer the commercial software Comsol Multiphysics [181], whose Wave Optics module allows the application of the finite element method to solve stationary and nonstationary electrodynamic problems. As a rule, this approach is employed to simulate a unit cell or a supercell of

the metasurface. Another popular commercial package is the Finite Difference Time Domain technique (Lumerical FDTD Solutions) [182], which makes possible the implementation of the finite difference method in the time domain. This technique is also widely applied by many authors [10, 22, 77, 108, 132]. It is more common employed to model lenses and holograms that cannot be broken into periodic cells. The third commercial computer simulation technology software package (CST Studio) [183] finds ample application for modeling metasurfaces by making use of both above techniques [15, 51, 55, 136, 163]. In addition, there are less popular packages for modeling, such as FDTD Concerto used in Ref. [42] and the program MAGMAS (Model for the Analysis of General Multilayered Antenna Structures) applied in Refs [89, 90]. At present, MAGMAS is sold by Synopsys Inc. [184]. Meep, a flexible free software package [185], is of value for the application of the finite difference method in the time domain to calculate metalenses [110, 111].

Calculating metasurface far and near fields implies the availability of great computational resources. For example, a supercomputer is needed to model a lens [112] on a grid of up to 10^{10} nodes. At the same time, a combination of numerical and analytical methods permits not only considerably reducing the amount of computation but also clarifying the physics of metasurface phenomena. A highly efficient method for the purpose has been developed by the authors of Ref. [186], who proposed finding numerically only multipole moments of meta-atoms and reserve analytical calculations for far fields.

6. Conclusions

The past few years have witnessed a tremendous upgrowth in metasurface research. A high efficiency of metasurfaces has been achieved in certain sectors compared with the light control effectiveness of the first specimens in the infrared spectrum, which hardly reached 15%. At the beginning, metasurfaces were used in combination with light polarizers, and the shift of operating frequency into the visible region resulted in a drop in efficiency to 1%. Thereafter, researchers gained an ability to create metasurfaces with an efficiency higher than 50% in the visible frequency region for which polarizers are not required; simultaneously, lenses with an efficiency up to 80% were manufactured.

This article was designed to overview the most interesting and promising avenues of metasurface research, such as the development of gradient metasurfaces for beam steering by altering its phase and amplitude in the visible and near infrared regions.

Phase control permits the direction of light transmitted through a metasurface to be set in accordance with the generalized Snell's law. The first metasurfaces comprised meta-atoms capable of phase control only by means of electric resonance in the 0 to π range. The meta-atoms were metallic nanoparticles of various shapes, which made necessary the employment of additional polarizers or the placement of meta-atoms only in odd or even Fresnel zones; it resulted in a further reduction in efficiency. A combination of electric and magnetic resonances became possible due to the application of dielectric meta-atoms, which allowed controlling the light phase in full measure from 0 to 2π and increasing at once efficiency of metasurfaces to 40%. The resonances were additionally combined on reflecting metasurfaces formed by metallic particles over a metal substrate. The

efficiency of such metasurfaces reached 50%. However, metasurfaces based on resonances are known to operate in relatively narrow spectral regions, which restricts their applications. Another approach to engineering metasurfaces makes use of the Pancharatnam–Berry phase. Such metasurfaces operate in a wide spectrum but only with circularly polarized radiation. The efficiency of such devices has also been significantly improved.

Metasurfaces are used to manufacture nanolenses, the thickness of which is much smaller than the radiation wavelength. Meta-atoms of such lenses control the light phase by focusing a plane wave on a point within the bounds of the lens focal length. The efficiency of the first metalenses did not also exceed 10%. After a time, it was enhanced to 40% by using dielectric meta-atoms, and their focusing accuracy reached 95%. The efficiency of lenses based on the Pancharatnam–Berry phase was as high as 86%.

Metalenses can work in a wide spectral range, but they are not free from chromatic aberration. Because light of various wavelengths is refracted at different angles, each lens focuses it at different distances. The large number of degrees of freedom in meta-atoms makes it possible to correct aberrations. Resonant metasurfaces from composite meta-atoms can deflect light of various wavelengths at the same angle. Therefore, they can be used to design lenses without chromatic aberration.

Integral phase and amplitude control of light by each meta-atom provides a basis for engineering holographic metasurfaces. Because meta-atoms are much smaller than the wavelength, such holograms undergo no distortion associated with additional diffraction maxima and can be more efficient than ordinary holograms. However, the available technologies do not yet allow creating holographic metasurfaces of a large size, which strongly restricts the quality of the resulting images.

Metasurfaces can serve as components of various optical devices, such as polarization transformers, polarized light detectors, and polarizing filters. Also, metasurfaces can serve as colorants and therefore operate as spectral filters. Moreover, metasurfaces are suitable for analog calculations and other purposes.

This review also covers nonlinear effects in metasurfaces that enrich their properties and expand the scope of their applications. Nonlinear effects are even more sensitive to varying meta-atom geometry and properties, as well as to environmental conditions, which opens up vast prospects for a variety of applications of metasurfaces, such as designing and manufacturing biosensors, second- and third-harmonic generators, optically controlled devices, and light microscopy designed to exceed the diffraction limit. Integration of meta-atoms into active elements, e.g., quantum heterostructures, allows the nonlinear response of metasurfaces to be enhanced. Such integration makes it possible to increase the second-harmonic generation power by an order of magnitude.

Combining metasurfaces with active media containing dye molecules or semiconductor quantum wells and dots permits the creation of miniature lasers and various devices based on them.

To sum up, metasurfaces are a subject of extensive research awaiting further development. A characteristic example of explosive exploration in this field of science and technology is the appearance, during preparation of the present article, of a new important area of studies concerned

with the formation and characteristics of metasurfaces with controlled charge concentration and conductivity, which may replace semiconductor elements in the future [187].

References

1. Novoselov K S et al. *Science* **306** 666 (2004)
2. Basov D N, Fogler M M, García de Abajo F J *Science* **354** 195 (2016)
3. Low T et al. *Nature Mater.* **16** 182 (2017)
4. Dai S et al. *Nature Commun.* **6** 6963 (2015)
5. Song J C W, Rudner M S *Proc. Natl. Acad. Sci. USA* **113** 4658 (2016)
6. Kumar A et al. *Phys. Rev. B* **93** 041413(R) (2016)
7. Klimov V *Nanoplasmonics* (Singapore: Pan Stanford Publ., 2014)
8. Kildishev A V, Shalaev V M *Phys. Usp.* **54** 53 (2011); *Usp. Fiz. Nauk* **181** 59 (2011)
9. Kildishev A V, Boltasseva A, Shalaev V M *Science* **339** 1232009 (2013)
10. Yu Y F et al. *Laser Photon. Rev.* **9** 412 (2015)
11. Born M, Wolf E *Principles of Optics* (Oxford: Pergamon Press, 1964);Translated into Russian: *Osnovy Optiki* (Moscow: Nauka, 1979)
12. Feynman R P, Leighton R B, Sands M L *The Feynman Lectures on Physics* Vol. 1 (New York: Basic Books, 2010); Translated into Russian: *Feinmanovskie Lektsii po Fizike. 3. Izluchenie, Volny. Kvanty* (Moscow: URSS, 2016)
13. Aieta F et al. *Science* **347** 1342 (2015)
14. Yu N, Capasso F *Nature Mater.* **13** 139 (2014)
15. Zheng G et al. *Nature Nanotechnol.* **10** 308 (2015)
16. Soukoulis C M, Wegener M *Nature Photon.* **5** 523 (2011)
17. Padilla W J, Basov D N, Smith D R *Mater. Today* **9** (7, 8) 28 (2006)
18. Shalaev V M et al. *Opt. Lett.* **30** 3356 (2005)
19. Xiang Y J et al., in *The 23rd PIERS 2008, Progress in Electromagnetics Research Symp., Hangzhou, China, 24 – 28 March, 2008* (Cambridge, MA: The Electromagnetics Academy, 2008) p. 952
20. Lapine M, Shadrivov I V, Kivshar Yu S *Rev. Mod. Phys.* **86** 1093 (2014)
21. Boltasseva A, Atwater H A *Science* **331** 290 (2011)
22. Yu N et al. *Science* **334** 333 (2011)
23. Ni X et al. *Science* **335** 427 (2012)
24. Scopus, https://www.scopus.com/
25. Zhan A et al. *ACS Photon.* **3** 209 (2016)
26. Jahani S, Jacob Z *Nature Nanotechnol.* **11** 23 (2016)
27. Zhang L et al. *Adv. Opt. Mater.* **4** 818 (2016)
28. Genevet P, Capasso F *Rep. Prog. Phys.* **78** 024401 (2015)
29. Chen H-T, Taylor A J, Yu N *Rep. Prog. Phys.* **79** 076401 (2016)
30. Shaltout A M, Kildishev A V, Shalaev V M *J. Opt. Soc. Am. B* **33** 501 (2016)
31. Wang J, Du J *Appl. Sci.* **6** 239 (2016)
32. Glybovski S B et al. *Phys. Rep.* **634** 1 (2016)
33. Minovich A E et al. *Laser Photon. Rev.* **9** 195 (2015)
34. Veselago V G *Sov. Phys. Usp.* **10** 509 (1968); *Usp. Fiz. Nauk* **92** 517 (1967)
35. Pendry J B *Phys. Rev. Lett.* **85** 3966 (2000)
36. Klimov V V *JETP Lett.* **89** 229 (2009); *Pis'ma Zh. Eksp. Teor. Fiz.* **89** 270 (2009)
37. Kalousek R et al. *Opt. Express* **20** 17916 (2012)
38. Johnson P B, Christy R W *Phys. Rev. B* **6** 4370 (1972)
39. Yu N et al. *Nano Lett.* **12** 6328 (2012)
40. Pors A, Nielsen M G, Bozhevolnyi S I *Nano Lett.* **15** 791 (2015)
41. Farmahini-Farahani M, Mosallaei H *Opt. Lett.* **38** 462 (2013)
42. Sun S et al. *Nature Mater.* **11** 426 (2012)
43. Sun S et al. *Nano Lett.* **12** 6223 (2012)
44. Pfeiffer C, Grbic A *Phys. Rev. Lett.* **110** 197401 (2013)
45. Zenin V A et al. *Opt. Express* **22** 10341 (2014)
46. Sarychev A K, Shvets G, Shalaev V M *Phys. Rev. E* **73** 036609 (2006)
47. Pors A et al. *Sci. Rep.* **3** 2155 (2013)
48. Pors A, Bozhevolnyi S I *Opt. Mater. Express* **5** 2448 (2015)
49. Pors A, Bozhevolnyi S I *Opt. Express* **21** 27438 (2013)
50. Evlyukhin A B et al. *Phys. Rev. B* **82** 045404 (2010)
51. Decker M et al. *Adv. Opt. Mater.* **3** 813 (2015)
52. Kerker M, Wang D-S, Giles C L *J. Opt. Soc. Am.* **73** 765 (1983)
53. Luk'yanchuk B S et al. *ACS Photon.* **2** 993 (2015)
54. Alaee R et al. *Phys. Rev. B* **91** 115119 (2015)
55. Shalaev M I et al. *Nano Lett.* **15** 6261 (2015)
56. Chen X et al. *Nature Commun.* **3** 1198 (2012)
57. Huang L et al. *Nano Lett.* **12** 5750 (2012)
58. Kang M et al. *J. Opt. Soc. Am. B* **29** 572 (2012)
59. Kang M et al. *Opt. Express* **20** 15882 (2012)
60. Klyshko D N *Phys. Usp.* **36** 1005 (1993); *Usp. Fiz. Nauk* **163** (11) 1 (1993)
61. Berry M V *J. Mod. Opt.* **34** 1401 (1987)
62. Butet J, Brevet P-F, Martin O J F *ACS Nano* **9** 10545 (2015)
63. Franken P A et al. *Phys. Rev. Lett.* **7** 118 (1961)
64. Kauranen M, Zayats A V *Nature Photon.* **6** 737 (2012)
65. Bachelier G et al. *J. Opt. Soc. Am. B* **25** 955 (2008)
66. Kujala S et al. *Phys. Rev. Lett.* **98** 167403 (2007)
67. Black L-J et al. *ACS Photon.* **2** 1592 (2015)
68. Chandrasekar R et al. *Opt. Mater. Express* **5** 2682 (2015)
69. Czaplicki R et al. *Nano Lett.* **15** 530 (2015)
70. Chen P-Y et al. *ACS Photon.* **2** 1000 (2015)
71. Bachelier G et al. *Phys. Rev. B* **82** 235403 (2010)
72. Wang F X et al. *Phys. Rev. B* **80** 233402 (2009)
73. Krause D, Teplin C W, Rogers C T *J. Appl. Phys.* **96** 3626 (2004)
74. Liu S et al. *Nano Lett.* **16** 5426 (2016)
75. Celebrano M et al. *Nature Nanotechnol.* **10** 412 (2015)
76. Baker R J *CMOS: Circuit Design, Layout, and Simulation* 3rd ed. (New York: Wiley. IEEE Press, 2010)
77. Khorasaninejad M et al. *Science* **352** 1190 (2016)
78. Zhang Y et al. *Sci. Rep.* **5** 10119 (2015)
79. Li Q-T et al. *Opt. Express* **24** 16309 (2016)
80. Czaplicki R et al. *Nano Lett.* **15** 530 (2015)
81. Czaplicki R et al. *Opt. Lett.* **41** 2684 (2016)
82. Husu H et al. *Nano Lett.* **12** 673 (2012)
83. Klein M W et al. *Science* **313** 502 (2006)
84. Berthelot J et al. *Opt. Express* **20** 10498 (2012)
85. Czaplicki R et al. *Phys. Rev. Lett.* **110** 093902 (2013)
86. van Nieuwstadt J A H et al. *Phys. Rev. Lett.* **97** 146102 (2006)
87. Yang X et al. *Opt. Lett.* **41** 2938 (2016)
88. Kruk S et al. *ACS Photon.* **2** 1007 (2015)
89. Valev V K *Langmuir* **28** 15454 (2012)
90. Valev V K et al. *Adv. Mater.* **26** 4074 (2014)
91. Camacho-Morales R et al. *Nano Lett.* **16** 7191 (2016)
92. Carletti L et al. *Nanotechnology* **28** 114005 (2017)
93. Lee J et al. *Nature* **511** 65 (2014)
94. Lee J et al. *Adv. Opt. Mater.* **4** 664 (2016)
95. Wolf O et al. *Nature Commun.* **6** 7667 (2015)
96. Nookala N et al. *Optica* **3** 283 (2016)
97. Tymchenko M et al. *Phys. Rev. Lett.* **115** 207403 (2015)
98. Lee J et al. *Adv. Opt. Mater.* **2** 1057 (2014)
99. Aieta F et al. *Nano Lett.* **12** 4932 (2012)
100. Ni X et al. *Light Sci. Appl.* **2** e72 (2013)
101. Chao W et al. *Opt. Express* **17** 17669 (2009)
102. Fu Y, Zhou W, Lim L E N *J. Opt. Soc. Am. A* **25** 238 (2008)
103. Etayo D, Ederra I, Gonzalo R *J. Infrared Millim. Terahertz Waves* **35** 525 (2014)
104. Andersen G *Opt. Lett.* **30** 2976 (2005)
105. Gao H et al. *Nano Lett.* **10** 4111 (2010)
106. Shi Z et al. *Plasmonics* **5** 175 (2010)
107. Ishii S, Shalaev V M, Kildishev A V *Nano Lett.* **13** 159 (2013)
108. Almeida E, Shalem G, Prior Y *Nature Commun.* **7** 10367 (2016)
109. Arbabi A et al. *Opt. Express* **23** 33310 (2015)
110. Arbabi A et al. *Nature Commun.* **6** 7069 (2015)
111. Arbabi E et al. *Optica* **3** 628 (2016)
112. Byrnes S J et al. *Opt. Express* **24** 5110 (2016)
113. Vo S et al. *IEEE Photon. Technol. Lett.* **26** 1375 (2014)
114. Khorasaninejad M et al. *Nano Lett.* **17** 1819 (2017)

115. Wen D et al. *Adv. Opt. Mater.* **4** 321 (2016)
116. Chen X et al. *Adv. Opt. Mater.* **1** 517 (2013)
117. Lin D et al. *Science* **345** 298 (2014)
118. West P R et al. *Opt. Express* **22** 26212 (2014)
119. Tang D et al. *Laser Photon. Rev.* **9** 713 (2015)
120. Zhao Z et al. *Sci. Rep.* **5** 15781 (2015)
121. Khorasaninejad M et al. *Nano Lett.* **15** 5358 (2015)
122. Arbabi E et al. *Sci. Rep.* **6** 32803 (2016)
123. Eisenbach O et al. *Opt. Express* **23** 3928 (2015)
124. Huang L et al. *Nature Commun.* **4** 2808 (2013)
125. Zhang H, Tan Q, Jin G *Opt. Eng.* **51** 075801 (2012)
126. Wen D et al. *Nature Commun.* **6** 8241 (2015)
127. Huang Y-W et al. *Nano Lett.* **15** 3122 (2015)
128. Chen W T et al. *Nano Lett.* **14** 225 (2014)
129. Devlin R C et al. *Proc. Natl. Acad. Sci. USA* **113** 10473 (2016)
130. Huang K et al. *Laser Photon. Rev.* **10** 500 (2016)
131. Chong K E et al. *ACS Photon.* **3** 514 (2016)
132. Wang B et al. *Nano Lett.* **16** 5235 (2016)
133. Li Q-T et al. *Opt. Express* **24** 16309 (2016)
134. Zhou F et al. *Opt. Express* **21** 4348 (2013)
135. Ye W et al. *Nature Commun.* **7** 11930 (2016)
136. Wang Q et al. *Sci. Rep.* **6** 32867 (2016)
137. Ni X, Kildishev A V, Shalaev V M *Nature Commun.* **4** 2807 (2013)
138. Walther B et al. *Adv. Mater.* **24** 6300 (2012)
139. Wan W, Gao J, Yang X *ACS Nano* **10** 10671 (2016)
140. Montelongo Y et al. *Nano Lett.* **14** 294 (2014)
141. Almeida E, Bitton O, Prior Y *Nature Commun.* **7** 12533 (2016)
142. Wang L et al. *Optica* **3** 1504 (2016)
143. Pors A, Nielsen M G, Bozhevolnyi S I *Optica* **2** 716 (2015)
144. Panchenko E et al. *ACS Photon.* **3** 1833 (2016)
145. Wen D et al. *Opt. Express* **23** 10272 (2015)
146. Khorasaninejad M et al. *Nano Lett.* **16** 4595 (2016)
147. Zhao Y, Alù A *Nano Lett.* **13** 1086 (2013)
148. Ding F et al. *ACS Nano* **9** 4111 (2015)
149. Gorodetski Y, Karabchevsky A *Proc. SPIE* **9883** 98830H (2016)
150. Mo W et al. *Opt. Express* **24** 13621 (2016)
151. Wu P C et al. *Nano Lett.* **17** 445 (2017)
152. Klimov V V et al. *Opt. Express* **24** 6172 (2016)
153. Klimov V V et al. *Phys. Rev. A* **92** 063842 (2015)
154. Treshin I V et al. *Phys. Rev. A* **88** 023832 (2013)
155. Hedayati M K, Elbahai M *Plasmonics* **12** 1463 (2017)
156. Ellenbogen T, Seo K, Crozier K B *Nano Lett.* **12** 1026 (2012)
157. Kumar K et al. *Nature Nanotechnol.* **7** 557 (2012)
158. Yue W et al. *Sci. Rep.* **6** 29756 (2016)
159. Zapata-Rodríguez C J et al., in *16th Intern. Conf. on Transparent Optical Networks, ICTON, 6 – 10 July 2014* (Piscataway, NJ: IEEE, 2014)
160. Zhu X et al. *Nature Nanotechnol.* **11** 325 (2016)
161. Cheng F et al. *Sci. Rep.* **5** 11045 (2015)
162. Genet C, Ebbesen T W *Nature* **445** 39 (2007)
163. Silva A et al. *Science* **343** 160 (2014)
164. Chizari A et al. *Opt. Lett.* **41** 3451 (2016)
165. Lee K-L et al. *Sci. Rep.* **5** 8547 (2015)
166. Sreekanth K V et al. *Nature Mater.* **15** 621 (2016)
167. Bahramipanah M et al. *ACS Nano* **9** 7621 (2015)
168. Klimov V V et al. *J. Phys. D* **50** 285101 (2017)
169. Butet J, Martin O J F *Nanoscale* **6** 15262 (2014)
170. Kim E et al. *Phys. Rev. B* **78** 113102 (2008)
171. Mesch M et al. *Nano Lett.* **16** 3155 (2016)
172. Yang A et al. *Nature Commun.* **6** 6939 (2015)
173. Hakala T K et al. *Nature Commun.* **8** 13687 (2017)
174. Schokker A H, Koenderink A F *Phys. Rev. B* **90** 155452 (2014)
175. Zhou W et al. *Nature Nanotechnol.* **8** 506 (2013)
176. van Exter M P et al. *Opt. Express* **21** 27422 (2013)
177. van Beijnum F et al. *Phys. Rev. Lett.* **110** 206802 (2013)
178. Tenner V T, de Dood M J A, van Exter M P *ACS Photon.* **3** 942 (2016)
179. Meng X et al. *Laser Photon. Rev.* **8** 896 (2014)
180. Zyablovskii A A et al. *JETP* **125** 175 (2017); *Zh. Eksp. Teor. Fiz.* **152** 211 (2017)
181. COMSOL, https://www.comsol.ru/
182. Lumerical Inc., https://www.lumerical.com/
183. CST — Computer Simulation Technology, https://www.cst.com/
184. Synopsys. Optical Solutions. RSoft, https://www.synopsys.com/optical-solutions/rsoft.html
185. Oskooi A F et al. *Comput. Phys. Commun.* **181** 687 (2010)
186. Pavlov A A et al. *Quantum Electron.* **43** 496 (2013); *Kvantovaya Elektronika* **43** 496 (2013)
187. Forati E et al. *Nature Commun.* **7** 13399 (2016)